

T-4460

**In-Situ Studies of the Electrochemical Interface of
Cu/Pt (poly) Using Surface
Extended X-ray Absorption Fine Structure**

by
Li Wang

ProQuest Number: 10796581

All rights reserved

INFORMATION TO ALL USERS

The quality of this reproduction is dependent upon the quality of the copy submitted.

In the unlikely event that the author did not send a complete manuscript and there are missing pages, these will be noted. Also, if material had to be removed, a note will indicate the deletion.



ProQuest 10796581

Published by ProQuest LLC (2019). Copyright of the Dissertation is held by the Author.

All rights reserved.

This work is protected against unauthorized copying under Title 17, United States Code
Microform Edition © ProQuest LLC.

ProQuest LLC.
789 East Eisenhower Parkway
P.O. Box 1346
Ann Arbor, MI 48106 – 1346

T-4460

A thesis submitted to the Faculty and the Board of Trustees of the Colorado School of Mines in partial fulfillment of the requirements for the degree of Ph.D in Applied Physics.

Golden, Colorado

Date 6/21/94

Signed: Li Wang
Li Wang

Approved: Thomas E. Furtak
Dr. T. E. Furtak
Professor of Physics
Thesis Advisor

Golden, Colorado

Date 6/23/94

John U. Trefny
Dr. J. U. Trefny
Professor and Head
Department of Physics

ABSTRACT

In-situ surface extended x-ray absorption fine structure (SEXAFS) spectroscopy measurements were made from a copper monolayer underpotentially deposited (UPD) on a polycrystalline platinum substrate with a grazing incidence geometry using a fluorescence detection mode. The purpose of this project was to improve the experimental aspects of this technique with the aim of structural study of the electrochemical interface. The system of a single Cu atomic layer on Pt was chosen because of its perceived simplicity as a strongly bound electroadsorbate, and to provide a marker layer suitable for identification of the surface of the electrode. Signal-to-noise ratios of 4 were obtained in a single SEXAFS scan. This was accomplished through a design based upon a large surface area (47 cm²). Measurements were performed on the same layer using both s- and p-polarized x-rays. The results of multiple scans showed that, surrounding an average copper atom there are 3 oxygen neighbors at a distance of 2.06 ± 0.03 Å, 4 copper neighbors at a distance of 2.62 ± 0.03 Å, and 3 platinum neighbors at a distance of 2.65 ± 0.03 Å. This information is consistent with a model of copper in a three-fold hollow site on the platinum surface, with oxygen in a strongly bound relationship. Neighboring copper atoms are not close-packed, but lie in an open structure. These results have demonstrated how high quality *in-situ* SEXAFS can be obtained in an electrochemical environment, and have contributed to the understanding of a specific system.

TABLE OF CONTENTS

ABSTRACT		iii
LIST OF FIGURES		vii
LIST OF TABLES		ix
ACKNOWLEDGMENTS		x
Chapter 1	INTRODUCTION	2
Chapter 2	LITERATURE SURVEY	7
2.1	Review of Techniques for Electrode/Electrolyte Interfacial Study . . .	7
2.1.1	Introduction	7
2.1.2	Optical Second Harmonic Generation (SHG)	8
2.1.3	Scanning Tunneling Microscopy (STM) and Atomic Force Microscopy (AFM)	8
2.1.4	X-ray Diffraction (XRD)	9
2.1.5	X-ray Standing Wave (XSW)	9
2.1.6	Differential Reflectance Spectroscopy (DRS)	10
2.1.7	Quartz Crystal Microbalance (QCM)	10
2.1.8	Extended X-ray Absorption Fine Structure (EXAFS) Spectroscopy	11
2.1.9	Comparison of <i>In-Situ</i> Methods	12
2.2	Review of Previous UPD Studies	13
2.2.1	Electrochemical Studies	13
2.2.2	Anion Effect	15
2.2.3	STM Studies	18
2.2.4	X-ray Absorption Studies	19
2.2.5	AFM Studies	26
2.2.6	Summary	26
Chapter 3	THEORIES AND TECHNIQUES	28
3.1	Electrochemical Theories and Techniques	28
3.1.1	Underpotential Deposition(UPD)	28
3.1.2	Energy Level Diagram of UPD	33
3.1.3	Density of States of the Adatom/Foreign Metal Substrate System	35
3.2	EXAFS Techniques and Theory	37

3.2.1	Introduction	37
3.2.2	Synchrotron Radiation	38
3.2.3	Theory of EXAFS	39
3.2.4	Data Analysis	48
3.3	Experimental	57
3.3.1	Substrate Preparation	57
3.3.2	Cell Design	57
3.3.3	Solution Preparation	60
3.3.4	Experimental Setup	60
3.3.5	X-9 Beam Line	66
3.3.6	Sample Alignment	66
Chapter 4	RESULTS AND DISCUSSION	70
4.1	Electrochemical Results	70
4.1.1	Characterization of the Clean Pt Substrate	70
4.1.2	True Surface Area Determination	72
4.1.3	Cell Contamination Test	74
4.1.4	Anion Effects	74
4.1.5	Cu Adlayer Stability Characterization	76
4.2	SEXAFS results	83
4.2.1	Estimation of Water Thickness and Surface Roughness from Angle Scan	83
4.2.2	Incident Angle and Energy Dependent	83
4.2.3	Standards	85
4.2.4	High Signal to Noise Ratio	89
4.2.5	Step High Change with Changing of Water Layer Thickness	91
4.2.6	Near Edge Spectrum	91
4.2.7	Post Edge Spectrum	96
Chapter 5	SUMMARY AND CONCLUSION	105
Chapter 6	SUGGESTED WORK	108
	REFERENCES	111
Appendix A	CLEANING PROCEDURE FOR GLASS SUBSTRATES	117
Appendix B	MODELS FOR THE SOLID-ELECTROLYTE INTER- FACE(DOUBLE LAYER STRUCTURE)	118
B.1	The Parallel-Plate Condenser (Helmholtz Model)	118

B.2	The Diffuse Double Layer (Gouy-Chapman Model)	119
B.3	The Inner Layer Double Layer (Stern-Grahame Model)	120
B.4	Water Structure in the Double Layer BDM Model	121
B.5	Molecular Dynamics Simulation of Ion Adsorption	122
Appendix C	REFLECTANCE SPECTROSCOPY SET-UP	123

LIST OF FIGURES

2.1	Cyclic voltammogram of Cu adsorbed on Pt electrodes.	14
2.2	Adsorbed water, bisulfate and sulfate anions on a Pt electrode	17
2.3	Schematic diagram of Cu and O	22
2.4	Cu K edge XANES spectra	24
3.1	Underpotential shift ΔE_p as a function of the work function difference ($\Delta\phi$)	32
3.2	Schematic diagram of energy level produced from Kolb	34
3.3	Calculated electronic densities of states in states/eV	36
3.4	Schematic diagram of origin of EXAFS (Hayes and Boyce, 1982)	40
3.5	Schematic diagram of grazing incident geometry.	44
3.6	Schematic representation of angles	46
3.7	Absorption coefficient of copper foil standards	49
3.8	The EXAFS modulation $k\chi$ on the copper k-shell absorption cross section.	53
3.9	Fourier transform $k\chi$ of copper foil standard	55
3.10	Schematic diagram of the electrochemical cell	58
3.11	Schematic diagram of the electrochemical set up	61
3.12	Experimental setup of EXAFS study.	63
3.13	Efficiency of a 15-cm long gas ionization chamber as a function of energy,	64
3.14	Schematic diagram of X-9 beam line.	67
3.15	Laser alignment	69
4.1	Cyclic voltammogram of Pt electrode in 0.5 M sulfuric acid solution.	71
4.2	Cyclic voltammogram of Pt electrode in different electrolytes:	75

4.3	Normalized reflectance change $\Delta R/R$ as a function of desorbing time t	78
4.4	Voltammetry of Cu adlayer on polycrystalline Pt electrode	80
4.5	Angle dependent reflectivity	84
4.6	Near edge spectrum of the standards.	86
4.7	EXAFS function of nickel filter	88
4.8	The adsorption coefficient from a single scan	90
4.9	Step height change with the change of water layer thickness	92
4.10	The near-edge region of the fluorescence spectra in s- (solid line) and p- (dashed line) polarization	94
4.11	The SEXAFS function $k\chi(k)$ from s-polarization	97
4.12	The SEXAFS function $k\chi(k)$ from both s- and p-polarization.	98
4.13	The Fourier transform of the $k\chi(k)$ for s polarization,	99
4.14	The Fourier transform of the $k\chi(k)$ for p polarization,	100
4.15	Schematic diagram of Cu adlayer associated with O.	103
6.1	Voltammetry of Cu adlayer on polycrystalline Pt electrode in hydrochloric acid solution.	110
C.1	schematic diagram of the reflectance experimental set up.	124

LIST OF TABLES

0.1	Table of Acconyms	1
3.1	The Potential Difference Between the Bulk and Monolayer Desorption Peaks (ΔE_p)	31
3.2	Parameters from Theoretical Calculation for Standards	56
4.1	The True Surface Area of the Pt Substrate	73
4.2	Threshold Position of Standards	87
4.3	Normalized Edge Position of Cu Foil, and Cu Adlayer of Both s- and p- Polarization	95
4.4	Results from the Model of 2s + p	104

ACKNOWLEDGMENTS

I gratefully acknowledge the contributions of my thesis advisor professor Thomas E. Furtak. He is not only a good professor, but also a good friend to work with. Without his ingenious advice, endless patience, and willing help, this dissertation would still be a dream.

I wish to acknowledge the collaborators at Rensselaer Polytechnic Institute (RPI), for their invaluable participation in the EXAFS data analysis. It is impossible to finish this dissertation without their cooperation. They are professor Timothy M. Hayes, Dr. J. Pant, Dr. L. Lurio, Dr. W. Li, Dr. G. Liang, Mr. J. Zhang, Mr. K. Pansewicz, Dr. V. Iskandarian, Mr. G. Kendall, Mr. C. M. Lo, and Mr. A. Rahimi. A very special thanks to professor Hayes for his advice, guidance and encouragement. I thank Dr. J. Pant and Dr. L. Lurio for their intense work on the data analysis, and methodology.

I would like to express my special thanks to Dr. Patrick MacCarthy, Dr. D. M. Wood, Dr. M. Haun and Dr. T. R. Ohno for serving on my committee.

Thanks are also due to Mr. J. P. Kintner for his instant help in the machine shop, Dr. Abdelkader Outzourhit for the invaluable discussions, and Dr. P. Samanta and Ms. E. A. Creek for their early work in the project.

I am very grateful to the people who helped me with material characterizations, Mr. R. McGrew for copper wire characterization with SEM from the Metallurgy Department of Colorado School of Mines (CSM), Mr. H. Moutinho for the roughness measurement with AFM from National Renewable Energy Laboratory.

Special thanks also go to my husband Dahong Du in the physics department of CSM for his invaluable discussions, endless help and encouragement.

Thanks also go to my parents, my brothers, my sisters, my nephew and my son for their understanding, support and love.

Finally, I wish to thank all of the members of the Physics Department at the Colorado School of Mines.

This work was supported by the Office of Naval Research through contracts N00014-90-J-1326 and N00014-90-J-1332. The experiments were performed at the National Synchrotron Light Source on beamline X9A, built and operated by the National Biostructures Research Resource.

T-4460

To My Husband Dahong Du.

Table 0.1: Table of Acconyms

AFM	Atomic Force Microscopy
CSM	Colorado School of Mines
DRS	Differential Reflectance Spectroscopy
DLR	Double Layer Region
EXAFS	Extended X-ray Absorption Fine Structrue Spectroscopy
IRS	Infrared Reflectance Spectroscopy
NND	Nearest Neighbor Distance
NSLS	Brookhaven National Synchrotron Light Source
PTFE	Polytetrofluoroethylene
QCM	Quartz Crystal Microbalance
RPI	Rensselaer Polytechnic Institute
SEM	Scanning Electron Microscopy
SERS	Surface Enhanced Raman Spectroscopy
SHG	Second Harmonic Generation
SND	Second Neighbor Distance
SSRL	Stanford Synchrotron Radiation Laboratory
STM	Scanning Tunneling Microscopy
UPD	Underpotential Deposition
XAS	X-ray Absorption Spectroscopy
XRD	X-ray Diffraction
XSW	X-ray Standing Wave

Chapter 1

INTRODUCTION

During the past several decades, the investigation of electrode adsorbate structure, on a microscopic level, has become more reliable partly due to the development of new *in-situ* spectroscopic techniques [1] such as extended x-ray absorption fine structure spectroscopy (EXAFS), surface enhanced Raman spectroscopy (SERS), second-harmonic generation (SHG), and infrared reflectance spectroscopy (IRS). Structure information in an electrochemical environment is particularly important because many practical processes occur at metal/electrolyte interfaces. Understanding the interfacial structure is a key to understanding chemisorption, hence catalysis. Strong interaction between adatoms and substrates dramatically changes the physical and chemical properties of the adlayer. These systems are of technological, as well as scientific, interest in areas such as corrosion, generation and storage of electrical energy, electroplating, electrochemical sensors, fuel cells and miniaturization of electronic devices.

X-ray absorption spectroscopy is a powerful technique for obtaining information on the geometry of the material in the electrochemical environment. In order to increase the sensitivity of x-rays to the metal/solution interface, a 'marker' layer with a unique atomic identity needed to be established for the study. A Cu adlayer on the Pt substrate was chosen for this purpose.

Underpotential deposition (UPD) is an electrochemical process whereby several monolayers or a submonolayer of adatoms are deposited on a foreign metal substrate at potentials more positive than the reversible Nernst potential [2] (for more detailed

information see section 3.1, Eq. (3.4)). This means that the deposition of Cu on a Pt surface occurs at potentials more positive than those where Cu would deposit on bulk Cu. Underpotential deposition is a unique method to form a uniform monolayer or submonolayer under equilibrium conditions. The surface coverage of the adlayer can be controlled by changing the deposition potential and the concentration of the metal ions in the aqueous electrolyte. The mechanism of UPD is still controversial and requires an *in-situ* technique to obtain more information about the adlayer. However, the study of UPD was originally a secondary goal.

The UPD process on noble metal substrates has been studied for a long time. UPD systems are of interest because of 1) they form a class of well-defined strong adsorption problems that are useful as a prototype for strong adsorption in electrochemistry; 2) the adatom lattices form interesting two-dimensional networks that have different electronic properties than individual atoms or bulk material of the same type; 3) some (but not many) catalytic processes are known which rely on adatom monolayers of a foreign metal [3].

The development of high intensity x-ray sources through synchrotron radiation has facilitated the characterization of the structure at liquid-solid interfaces. Since x-rays interact more weakly with water than with metals, they penetrate an appreciable distance, making it possible to study the surface under water. XAS is potentially more powerful in this application than any other technique. It has the capability of revealing the structure of the substrate and the short-range structure of the electrolyte as well. Nowadays, electrochemical studies which use synchrotron radiation are commonly recognized by scientists. However, the development of these techniques is still beginning.

This project was part of a collaboration with Dr. Tim Hayes' group at Rensselaer

Polytechnic Institute (RPI). All experiments such as reflectance spectroscopy, cyclic voltammetry and the quartz crystal microbalance were done at CSM. The EXAFS measurements were done at Brookhaven National Laboratory. The EXAFS data analysis methodology, the analysis and results presented in this thesis were performed by the RPI group.

The two major objectives of this project were: 1) to further explore x-ray methods using synchrotron radiation to study the structure of the interface between a solid and a liquid; 2) to achieve a large signal to noise ratio so as to enable high precision data acquisition and analysis to reveal the local environment of atoms in a monolayer metal deposit on a foreign metallic substrate under electrochemical control. To this end, Cu was chosen in this work as the deposited metal and polycrystalline Pt was chosen as the substrates.

A large polycrystalline Pt substrate with a surface area of 47 cm^2 was used in order to increase the signal-to-noise ratio. In contrast to small single crystal substrates, the Bragg reflection from the surface of a polycrystalline substrate is averaged out. This removes potentially troublesome effects while preserving the near neighbor distance information. However, the signal to noise ratio in our experiment is much larger. The experiment exploits high intensity tunable x-rays, grazing incidence, and fluorescence detection using a custom ion chamber. The background was reduced by using a grazing incident geometry to limit the excited volume of the sample to that portion within a penetration depth of 20 \AA . Under this glancing angle condition, a surface monolayer can contribute 10 to 15% of the total signal. The fluorescence detection mode is commonly used in surface studies.

This thesis is organized as follows: In Chapter 2, a literature review of the interfacial structure for the Cu/Pt system as well as the Cu/Au system is presented.

Those have been studied by many groups using different *in-situ* methods. The results, however, are not consistent because each group has a slightly different approach. This part is followed by a brief review of *in-situ* surface techniques, emphasizing the advantages and disadvantages of each, paying particular attention to EXAFS.

In Chapter 3, a brief discussion of the techniques and theory which relate to this work is given. We used non-x-ray techniques to help understand the problem, including cyclic voltammetry, differential reflectance spectroscopy, and the quartz crystal microbalance. Cyclic voltammetry (measuring the change of the current I to calculate the total charge dQ transferred across the interface) and the quartz crystal microbalance (measuring the change of the frequency f to calculate the total mass change dm on the surface) were used together to compare the charge and mass transfer. Differential reflectance spectroscopy (which is sensitive to the valence electronic properties of the surface) was used to monitor the long-term stability of the Cu deposit. The main part of this chapter is focused on EXAFS theory and data analysis.

Results and discussion are given in Chapter 4. First, the methods used to obtain a clean Pt substrate in a sulfuric acid solution are presented. Anion effects are discussed as well. Second, results from the test of the stability of the Cu adlayer are presented. These tests were done by using both the cyclic voltammetry and the differential reflectance spectroscopy. Third, results pertaining to the oxidation state test using the quartz crystal microbalance are presented. The edge spectra of the standards and the Cu layer using both s-polarization and p-polarization are also presented in this chapter. Finally the results obtained from EXAFS post-edge spectra are discussed. The model for the local environment of the Cu adlayer on polycrystalline Pt is then presented.

The conclusion and summary of this work are given in Chapter 5. Future sug-

gested works are given in Chapter 6. The electrochemical result on Cu/Pt system in a perchloric acid solution is also presented in Chapter 6 to support an idea for further study.

Chapter 2

LITERATURE SURVEY

2.1 Review of Techniques for Electrode/Electrolyte Interfacial Study

2.1.1 Introduction

Traditionally, electrochemical techniques [2], such as cyclic voltammetry, have been used to investigate kinetic and thermodynamic properties of electrolyte-metal interfaces. The traditional electrochemical methods, however, give limited information about the microscopic structure of the metal surface at an atomic and molecular level. Recently non-electrochemical techniques, such as various spectroscopic and surface analytical techniques [3], have been used in tandem with the electrochemical methods to obtain the microscopic structure of these interfaces.

Ex-situ studies of adsorbed layers on metal substrates indicated that the metallic underlayer dominates the properties of the interface [4, 5, 6]. Unfortunately, the information obtained by *ex-situ* techniques may not be a true representation of the actual surface because the metal surface changes when the surface is transferred from solution to a vacuum system without potential control. For example, the structure of some passive films changes during transfer as hydroxyl groups decompose to oxides [7]. Moreover, any information on the solution side of the interface obtained by using *ex-situ* techniques is lost.

2.1.2 Optical Second Harmonic Generation (SHG)

Optical second harmonic generation has been used in electrochemical systems since 1967 [8]. Only recently, this nonlinear optical method has been recognized by electrochemists as being useful for probing adsorbed molecules in both a static and time-resolved mode [9]. This is because the SH signal is forbidden (the second order nonlinear susceptibility $\chi^{(2)}$ vanishes) in bulk media with a center of symmetry and is allowed only at the interface, where inversion symmetry is broken (under the electric dipole approximation). The second order nonlinear polarization is defined as

$$P^{(2\omega)} \propto \chi^{(2)} E(\omega)E(\omega), \quad (2.1)$$

where E is the electric field at the surface. For inversion symmetry, $E(\omega) = -E(\omega)$, $P^{(2\omega)} = -P^{(2\omega)}$, therefore $\chi^{(2)}$ must vanish. Furthermore, the fast time response of the SH signal allows one to investigate dynamic processes occurring over a wide range of time scales. This method has been used to study the potential dependence of several UPD systems [10, 11, 12]. However, the detail of the mechanism whereby SHG probes the electronic manifold of states that control $\chi^{(2)}$ is poorly understood.

2.1.3 Scanning Tunneling Microscopy (STM) and Atomic Force Microscopy (AFM)

In-situ scanning tunneling microscopy and atomic force microscopy are very powerful techniques for imaging the real space topographic and electronic properties of metal surfaces with up to atomic resolution ($\sim 1\text{\AA}$) [13, 14]. STM is based on a measurement of the current due to the tunneling of electrons between a sharp tip and a surface atom, while AFM exploits the atomic force between the tip and the sur-

face atom through a thin layer of water (approximately 10 Å). The tunneling current (from STM) and the atomic force (from AFM) will increase as the distance between the tip and surface atom decreases. Both *in-situ* STM and AFM were used by electrochemists in an electrochemical environment not long after the STM and the AFM became known. The real advantage of these techniques is that they allow one to directly obtain the atomic structure of a solid surface from images. However, chemical information cannot be directly measured.

2.1.4 X-ray Diffraction (XRD)

Another *in-situ* surface technique is x-ray diffraction (XRD) [15], which provides information on long-range order scale, while EXAFS gives information on local order scale. Further more, this method is far less sensitive to the atomic vibrations (the Debye-Waller factor) than is EXAFS. This method was first applied to *in-situ* studies by a group at IBM [16]. The surface sensitivity of XRD can be enhanced by using a grazing angle geometry, in which the incident beam impinges on the surface near the critical angle for total external reflection. Therefore the intensity of the electric field at or near the surface can be dramatically increased because of the limited beam penetration.

2.1.5 X-ray Standing Wave (XSW)

Most recently, an x-ray standing wave (XSW) technique has been utilized to probe the electrochemical double layer [17] and the structure of the metal-electrolyte interface [18]. The technique is based on stimulating atoms with the x-ray interference field. The interference field is generated through the diffraction from the substrate, which must be a perfect single crystal. The fluorescence photons can be detected as a

function of the shift of the wavefield. This technique has been practically used since the exploitation of synchrotron radiation.

2.1.6 Differential Reflectance Spectroscopy (DRS)

Optical properties of electrode/electrolyte systems have also been studied by differential reflectance spectroscopy [19], which measures the normalized reflectance change $\Delta R/R$ of a surface due to adsorption. The optical properties can be monitored as a function of photon energy, angle of incidence and the coverage of adatoms through this method. The main advantage of the technique is to extract information about electronic states of the adatom. Recently reflectance anisotropy on low index single crystals has been used to determine surface structure [20].

2.1.7 Quartz Crystal Microbalance (QCM)

Melroy *et al.* [21] were the first to use an *in-situ* quartz crystal microbalance method on a UPD system. The principle of the quartz crystal microbalance is based on the perturbation from a foreign mass Δm deposited on a quartz crystal substrate. If Δm is small compared to the mass of the substrate itself, the frequency response of the oscillating substrate to Δm follows a linear relation [22, 23] (for an AT-cut crystal).

$$\Delta f = -2.26(f_0^2/n)\Delta m \quad (2.2)$$

where f_0 (megahertz) is the resonant frequency of the unloaded quartz crystal, n is the order of the harmonic, and Δf (Hertz) is the shift of the resonant frequency due to the unit area mass loading Δm (micrograms per square centimeter). One can use this method to obtain the electroadsorption valency (γ).

2.1.8 Extended X-ray Absorption Fine Structure (EXAFS) Spectroscopy

X-ray photons (1 keV- 100 keV) can be used to obtain interfacial information under water. This is because x-ray propagation distances in many solutions are reasonably long and the wavelength of x-rays is comparable to interatomic distances (*e.g.* the wavelength of a common Cu K_{α} line is 1.54 Å).

Extended x-ray absorption fine structure (EXAFS) spectroscopy, which requires high intensity, tunable x-ray sources, has been used since the exploitation of synchrotron radiation [24]. In this method, the x-ray absorption cross section for an atom displays oscillations as a function of the energy above the threshold for excitation of a deeply bound core (K- or L-shell) electron. The oscillation is caused by interference between the outgoing electron wave and the back-scattered electron wave from neighboring atoms. Starting out as a laboratory curiosity, EXAFS has become a powerful analytical tool for the determination of local atomic environments (*e.g.* interatomic distances, coordination numbers, thermal and structure disorder) in *in-situ* complex systems (solid, liquids, and gases). Compared to conventional x-ray sources, synchrotron radiation has high intensities, a broad spectral range, a high degree of linear polarization, pulsed time structure and natural collimation [24]. The high intensities and broad or continuous spectral range significantly decrease the data acquisition time. This technique seems to be unique in providing environment information on the local species (chemical and bonding) at the electrode/electrolyte interface. For more information see section 3.2.

2.1.9 Comparison of *In-Situ* Methods

The advantage of using SHG is that it can monitor a variety of adsorptive and reactive processes on time scales as short as tens of femtoseconds. However, the structure information obtained through $\chi^{(2)}$ is simple, and the mechanisms of the effect are poorly understood. Information about the electronic states of the adatom can be extracted from DRS. The total charge of the adsorbate can be measured by the QCM. But the structure information obtained from SHG, DRS and QCM relates only indirectly to microscopic structural details. The surface topography of an adlayer can be precisely obtained from STM and AFM. Questions of using STM and AFM for probing the structure information are 1) adsorbed anions cannot be easily detected if it does not strongly adsorb on the substrate, so no environmental information is available; 2) the surface area which is actually probed by STM and AFM is relatively small (typically several nanometer square). Therefore the information obtained from a small area could be different than that obtained from a large area. The application of XSW in electrochemical systems is limited since it is a relatively new technique. The main advantage of using XSW is to study the potential dependent distribution of charged species within the diffuse double layer. However, this technique requires a perfect single crystal substrate and it gives only the structure information in the normal direction of the surface. EXAFS and XRD are unique tools for probing the structure and environmental information directly. EXAFS gives information on local order while XRD gives information on long-range order. The EXAFS technique also has the advantage over XRD that the analysis of the x-ray absorption near edge structure yields information about the state of oxidation of the central atom. In addition, XRD is much less sensitive to atomic vibrations than EXAFS because the x-ray scattering cross section in XRD is a function of the square of the atomic number.

Therefore, heavy elements tend to obscure the signal from the light elements.

2.2 Review of Previous UPD Studies

2.2.1 Electrochemical Studies

The phenomenon of underpotential electrodeposition of a metal onto a foreign metal substrate has been widely studied because of its importance in deposition and catalytic processes. The cyclic voltammogram study of underpotential deposition of Cu on Pt electrode (Cu/Pt) was first reported by Bowles [25]. This study showed that a monolayer was deposited onto Pt at potentials more positive than the potential for bulk Cu plating because the Pt-Cu bond is stronger than the Cu-Cu bond.

Cyclic voltammogram studies of a Cu adlayer underpotentially deposited on single crystal (100), (110), and (111) Pt surface and polycrystalline Pt were carried out by Kolb *et al.* [26, 27]. Their experiment was conducted in an electrolyte of 1N H₂SO₄ with 1 mM CuSO₄ for single crystals and 0.2 mM CuSO₄ for the polycrystalline case. Solutions were prepared with triple-distilled water and were bubbled with purified nitrogen prior to use. The desorption spectra of the Cu monolayer on Pt are shown in Fig. 2.1 with a scan rate of 10 mV/s for single crystals and 100 mV/s for polycrystalline Pt. The results showed that the desorption spectrum for polycrystalline Pt is the superposition of the desorption spectra of three low index plane substrates. The results on single crystals also revealed that a full Cu monolayer cannot form on all the crystal surfaces. Integration of the current due to the Cu layer desorption showed that a complete monolayer formed only on Pt (100) (410 $\mu\text{C}/\text{cm}^2$) and Pt (110) (310 $\mu\text{C}/\text{cm}^2$). The differences of the Cu coverage on Pt (100) and Pt (110) is due to the differences of the substrate surface atoms that are 416 $\mu\text{C}/\text{cm}^2$ for Pt (100) and 300 $\mu\text{C}/\text{cm}^2$ for Pt (110). Only two-thirds of a complete monolayer was

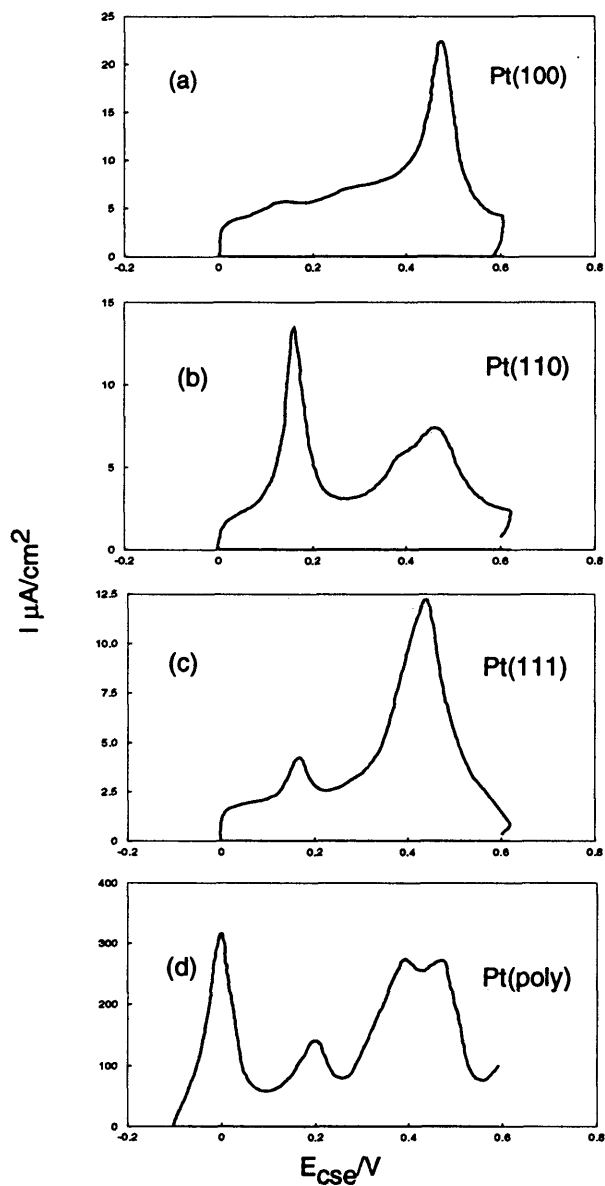


FIG. 2.1: Cyclic voltammogram of Cu adsorbed on Pt electrodes. (a), (b), (c): on Pt single crystal electrodes in 1N H_2SO_4 +1 M CuSO_4 and (d) on Pt polycrystalline in 1N H_2SO_4 + 0.2 M CuSO_4 reproduced from [26, 27].

observed on Pt (111) ($325 \mu\text{C}/\text{cm}^2$, Cu coverage corresponding to surface atoms of $480 \mu\text{C}/\text{cm}^2$). It is clear from Fig. 2.1 that the bonding energies are different for different faces. This suggests that different adlayer structures are formed on different faces. Another interesting result shown by Fig. 2.1 is that the first half monolayer is formed in a very narrow region on all the Pt substrates.

The interfacial bonding of a metal atom adsorbed on a foreign metal substrate was studied by Kramar *et al.* using XPS [28]. As mentioned before, the deposition of Cu on the Pt surface happens at potentials more positive than those where Cu would deposit on bulk Cu. This suggests that the bonding forces are different between Cu/Pt and Cu/Cu. The calculation indicates that the bonding of Cu/Pt (001) is much stronger than Cu/Cu or Pt/Pt bonding and exists only between a Cu monolayer and the first layer of Pt. The shorter Cu-Pt nearest neighbor distance (2.66 \AA) suggests that a strong attractive interaction between these atoms exists. The bonding energy depends strongly on the crystallographic orientation of the surface of the substrate. More detail will be given in section 3.1.3.

2.2.2 Anion Effect

It has been recognized for quite a time that anion adsorption can have a strong influence on the UPD behavior. The effect is found to increase in the sequence $\text{I}^- \geq \text{SCN}^- \geq \text{Br}^- \geq \text{Cl}^- \geq \text{SO}_4^{2-} \geq \text{F}^-$ [29, 30], the larger ions having a bigger effect. A similar study found that contact adsorption decreases within the sequence $\text{I}^- \geq \text{Br}^- \geq \text{Cl}^-$ [31]. The underpotential shift (ΔE_p , the potential difference between bulk metal deposition and monolayer deposition) decreases due to anion adsorption, suggesting a reduction of bond strength between the adatom and the substrate. In addition, anion adsorption results in an increase in the area under the monolayer peak

in the desorption spectrum. This is because both the metal atom adsorption and the anion desorption contribute to the current in the same direction. Therefore, a large apparent surface charge change is produced and the coverage of the Cu adlayer can not be directly obtained from a current-voltage curve alone.

Anions coadsorption with Cu on Pt (111) was studied by White *et al.* [32]. The results indicate that the coverage of Cu on Pt (111) decreases in the order $\text{Cl}^- \geq \text{Br}^- \geq \text{I}^- \geq \text{SO}_4^{2-}$. This suggests that the coadsorption of Cl^- has a much stronger influence than that of SO_4^{2-} .

The adsorption of bisulfate and sulfate anions on a Pt electrode in sulfuric acid solution was studied by Kunimatsu *et al.* [33] using IR spectroscopy. The possible configuration of water and anions adsorbed on a Pt electrode surface according to that study are shown in Fig. 2.2. In the region of hydrogen adsorption, the Pt surface is covered by adsorbed hydrogen and the water molecules are adsorbed through hydrogen bonding (Fig. 2.2a). In the region of oxygen adsorption, (Fig. 2.2b), the Pt surface is covered by oxygen and water molecules are in contact with the surface oxide through two hydrogen bonds. Some of the oxide surface is covered by sulfate ions. Therefore, the dipole moment of a water molecule is opposite in the hydrogen region to its orientation in the oxygen region. In the double layer region (no hydrogen or oxygen adsorbed), both bisulfate and sulfate anions are adsorbed on to the surface.

The adsorption of chloride (Cl^-) ions in the course of electrodeposition of Cu on a Pt electrode was also studied by Horanyi *et al.* [34] using a radiotracer method. Their results showed that the electroadsorption of Cu ions on a Pt electrode did not inhibit the specific adsorption of chloride ions. Adsorption of bisulfate (HSO_4^-) ions, from a solution of 10^{-3} M of Cu^{2+} induced by the electrodeposition of Cu on a Pt electrode, was also studied later by the same group [35]. Both experiments showed

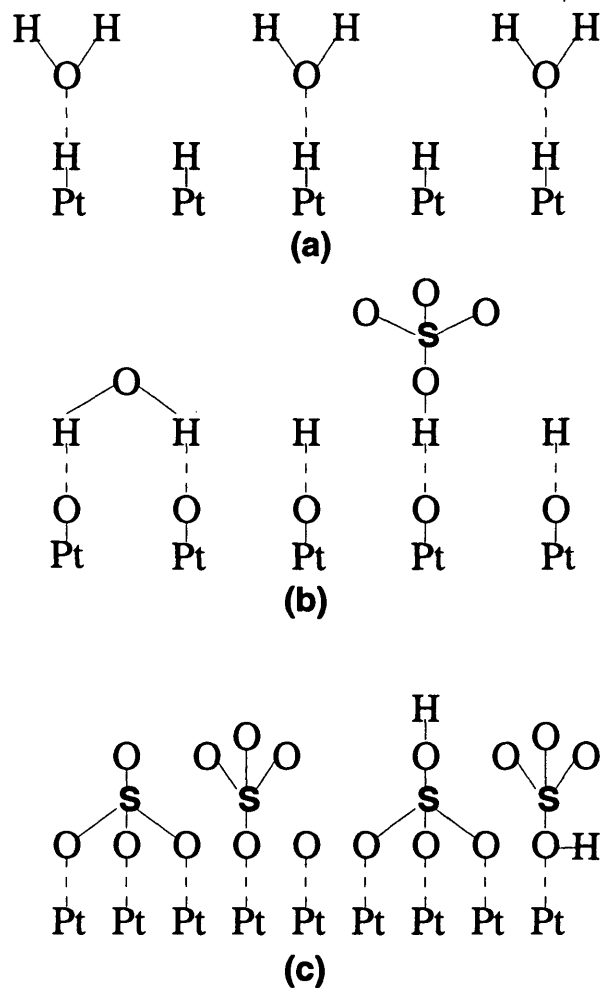


FIG. 2.2: Adsorbed water, bisulfate and sulfate anions on a Pt electrode surface in 0.5 M H_2SO_4 solution [33]: (a) adsorbed water in the hydrogen region; (b) adsorbed water and sulfate ions (SO_4^{2-}) in the oxygen region; (c) adsorbed bisulfate (HSO_4^-) and sulfate (SO_4^{2-}) ions in the double layer region.

that the underpotential deposition of Cu on a Pt electrode enhanced the adsorption of anions.

2.2.3 STM Studies

In-situ scanning tunneling microscopy of the UPD of Cu on Pt (111) was studied by Sashikata *et al.* [36]. The experiment was done in a 0.05 M H₂SO₄ + 5 mM CuSO₄ aqueous solution. The result suggested that the structure of the first Cu adlayer is ($\sqrt{3} \times \sqrt{3}$) R 30° and this open structure of the Cu adlayer is due to the coadsorption of the anions such as sulfate (SO₄²⁻) and bisulfate (HSO₄⁻) in the solution. There was a discrepancy in the total charge of UPD Cu on Pt (111) revealed by coulometric measurement and the charge which would be consistent with the STM measurement in their study. The coulometric results show a total charge of 270 μC/cm², while the STM would predict a total charge of 160 μC/cm² based on a ($\sqrt{3} \times \sqrt{3}$) R 30° structure. The results indicated that a significant charging current resulted from the desorption of SO₄²⁻ and HSO₄⁻ (non-Faradaic contribution) during the UPD process. In the non-Faradaic processes, charge does not cross the electrode/electrolyte interface, but currents can flow when the potential applied on the electrode changes. No other structure information, such as the environment of the anions, could be determined by this method.

The atomic structure of underpotentially deposited Cu on single crystal Au (100) and Au (111) was carefully studied by Magnussen *et al.* [37] using *in-situ* STM in a solution of 0.05 M H₂SO₄ and 5 mM CuSO₄. Samples were prepared by a flame annealing method with a well-ordered and atomically smooth surface. The results on clean substrates clearly showed that the presence of surface reconstruction on Au (100) was due to anion adsorption and oxidation-reduction cycles. No results were

given for Au (111), since the interaction between mobile sulfate ions and the surface is much stronger with Au (111) than Au (100) which affected the quality of the STM image. The studies of a Cu adlayer on Au (111) indicated that two different phases were observed depending on the Cu coverage. A hexagonal superstructure with a ($\sqrt{3} \times \sqrt{3}$) R 30° (honeycomb) unit cell and a densely packed hexagonal structure with a (5 x 5) unit cell correspond to Cu coverages of 0.33 monolayer and 0.64 monolayer, respectively. However, a more recent work suggested that the (5 x 5) reconstruction might be due to chloride contamination from a reference electrode [38]. Results in Ref. [37] of the Cu adlayer on Au (100) were not as well-defined as those on Au (111), but they appeared to have very similar structures. By considering the results on a full monolayer coverage from Ref. [39], Melroy *et al.* concluded that the atomic structure of Cu underpotentially deposited on Au (111) and Au (100) is strongly dependent on the Cu coverage. The increased Cu coverage resulted in more close-packed, quasihexagonal adlayer structures.

A very recent study of the UPD of Cu on Au (111) was carried out by Toshinori *et al.* [40]. The STM image exhibited only a ($\sqrt{3} \times \sqrt{3}$) R 30° structure for the first Cu UPD layer in a 0.05 M H₂SO₄ and 5 mM CuSO₄ solution. No other structure such as the (5 x 5), reported previously [37], was found in this study.

2.2.4 X-ray Absorption Studies

So far the *in-situ* EXAFS studies of underpotential deposition of Cu on a Pt have been limited. An *in-situ* EXAFS study of Cu underpotentially deposited on Pt (111) substrate pretreated with iodine was studied by White *et al.* [41]. The polarization of the incident x-ray beam was parallel to the substrate surface in their work. Cu was deposited from a dilute (0.05 mM) Cu²⁺ containing solution in 0.1 M H₂SO₄. The

EXAFS data indicated a Cu-Cu nearest neighbor distance of $2.88 \pm 0.04 \text{ \AA}$, which is affected by the surface active anions. No other information was given about the structure. However, in their experiment the sample area was very small; their data are very noisy by comparison to our data. In addition, since the Pt (111) surface was stabilized with adsorbed iodine prior to the experiment, it is unclear what relationship that work may have to our program.

In-situ XANES (X-ray Absorption Near Edge Structure) was applied to UPD Cu on carbon-supported Pt in 0.5 M H_2SO_4 [42]. It was reported that Cu only adsorbs on the Pt and not on the carbon. The XANES results indicated that the adsorbed Cu had an oxidation state close to Cu^+ with a tetrahedral coordination.

The latest study of underpotential deposition of Cu on Pt (100) by *in-situ* X-ray Absorption Spectroscopy (XAS) was carried out by Durand *et al.* in France [43]. They used fluorescence detection and grazing incidence with the plane of polarization of the incident beam parallel to the surface. The electrolytic solutions were 10^{-4} M Cu^{2+} , in 10^{-3} M HClO_4 , and in 1 M NaClO_4 . XAS results showed that the UPD of one monolayer Cu on the Pt surface splits into two adlayers. Both of them were in a $c(2 \times 2)$ surface structure with a vertical distance of 1.35 \AA . Oxygen atoms are found in both adlayers, between Cu atoms. The distance between Cu and O was 1.97 \AA which is half the distance of in-plane Cu (3.93 \AA). The nearest distance between Cu-Cu was found to be 3.09 \AA with the Cu atoms not in the same adlayer, but in two separate adlayers. The angle of the Cu-Cu nearest neighbor vectors with the surface plane is 26° degrees.

From previous studies of Cu/Pt systems, it is not hard to conclude that the structure of a Cu monolayer on Pt surface forms an open structure and the adlayer structure is dependent on the orientation of the substrate surface. XANES study

suggests that the adlayer of Cu is partially discharged (the valence electrons are less than 2). However, questions about those studies are 1) the iodine pretreated Pt surface may behave differently from the pure Pt surface; 2) the edge difference between Cu^0 and Cu^+ is only 1 eV, which makes the data analysis very difficult; 3) since EXAFS oscillations are very sensitive to the polarization of the measurement, both polarizations should be measured.

Up to now, several groups have been studying the Cu(adatoms)/Au(single crystal substrates) system using the EXAFS technique. The Cornell and IBM groups [44] used a grazing incidence geometry and fluorescence detection mode to investigate the underpotentially deposited Cu monolayer on Au (111). The sample size was 25 x 100 mm and the solution contained 1 M H_2SO_4 with 2×10^{-5} M Cu ions. The monolayer was deposited at 0.13 V with respect to a 3 M KCl Ag/AgCl electrode for 10 minutes before removing the excess electrolyte. All EXAFS measurements were done at this potential with the x-ray polarized perpendicular to the substrate surface (p-polarization). They observed strong scattering from Cu-O with a bond length of either 2.05 or 2.08 ± 0.03 Å. The first Cu-O distance is associated with the model of a single O (from water) sitting on top of the Cu atoms (see Fig. 2.3a). The second Cu-O distance is associated with the model of sulfate ions (SO_4^{-2}) on top of Cu atoms (Fig. 2.3b). This suggests that the electrolyte (or water) is not randomly adsorbed on the surface but at well-defined distances. In both cases the Cu atoms are sitting in the gold 3-fold hollow sites.

Melroy *et al.* [39] performed measurements with s-polarization with the beam polarized parallel to the substrate surface on a completely different system. The monolayer was prepared in 0.5 M sulfuric acid with 5×10^{-5} M Cu^{2+} on Au (111) at a potential of 0.13 V with respect to 3 M KCl Ag/AgCl for 10 min before deflating the

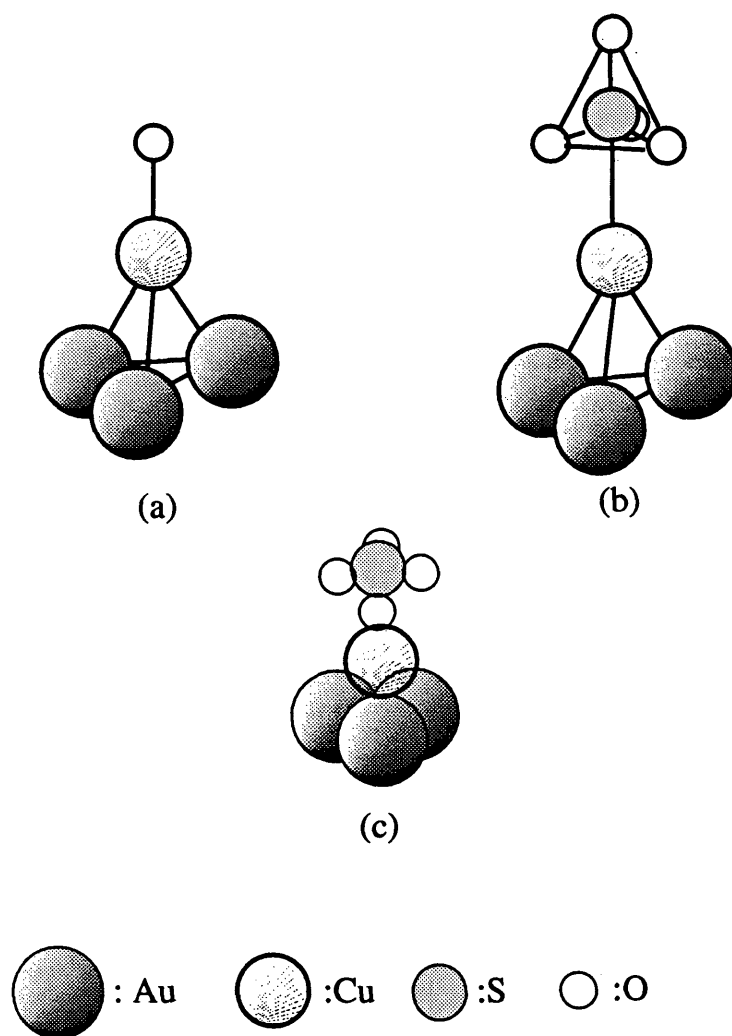


FIG. 2.3: Schematic diagram of Cu and O

(a). Schematic diagram of Cu and O (from water) on top of the gold(111) surface (p-polarization); (b). Schematic diagram of Cu and SO₄²⁻ (from the electrolyte) on top of the gold(111) surface (p-polarization); (c). Schematic diagram of Cu and SO₄²⁻ on top of the gold (111) surface (s-polarization). Figures (a) and (b) are reproduced from Blum [44], and (c) is reproduced from Melroy [39].

cell window (taking extra water out of the cell). The sample size was 1" x 3". They found that the near edge spectra are different for the oxidized Cu monolayer and the unoxidized Cu monolayer, the oxidized Cu monolayer has a higher energy edge than the unoxidized Cu monolayer. This is consistent with the larger binding energy of the core electrons for the higher oxidation state Cu^{2+} . Formation of a Cu alloy was found during their Cu deposition on gold, but it is insignificant in the EXAFS signal (only 5% of the Cu monolayer). In this geometry, strong scatterings from Cu-Cu and Cu-Au appeared. The nearest neighbor distances were $2.92 \pm 0.02 \text{ \AA}$ and $2.58 \pm 0.03 \text{ \AA}$, for Cu-Cu and Cu-Au respectively. The Cu-Cu distance is very close to the Au-Au distance in the (111) plane surface. The Cu-Au distance is consistent with their previous results and confirms that Cu atoms sit in the gold 3-fold hollow sites. No O was detected in this geometry. From this information, they concluded that the structure of the underpotentially deposited Cu on gold(111) at full monolayer coverage was as shown in Fig. 2.3c.

The Tourillon and Tadjeddine group [45] also used the grazing incident geometry and fluorescence detection mode to study a monolayer and a bilayer of Cu underpotentially deposited on a gold(100) surface. The electrolyte was 0.5M sodium sulfate (Na_2SO_4), and the Cu^{2+} ion concentration was 10^{-4} M . The pH was adjusted to 3 by adding H_2SO_4 . The monolayer was prepared at a potential of 0.1 V with respect to a saturated calomel electrode (SCE) and held at the same potential during all EXAFS measurements. The x-rays were polarized parallel to the Au surface (s-polarization). The x-ray absorption near-edge structure (XANES) (see Fig. 2.4a) showed that the Cu^{2+} edge has a higher energy than the Cu^+ edge and metallic Cu edge. The energy difference (7.5 eV) between $\text{Cu}^{2+}(3d^9)$ and $\text{Cu}^+(3d^{10})$ is due to the difference of the d-band configuration. The slight difference of edge position(1.1eV) between Cu^+ and

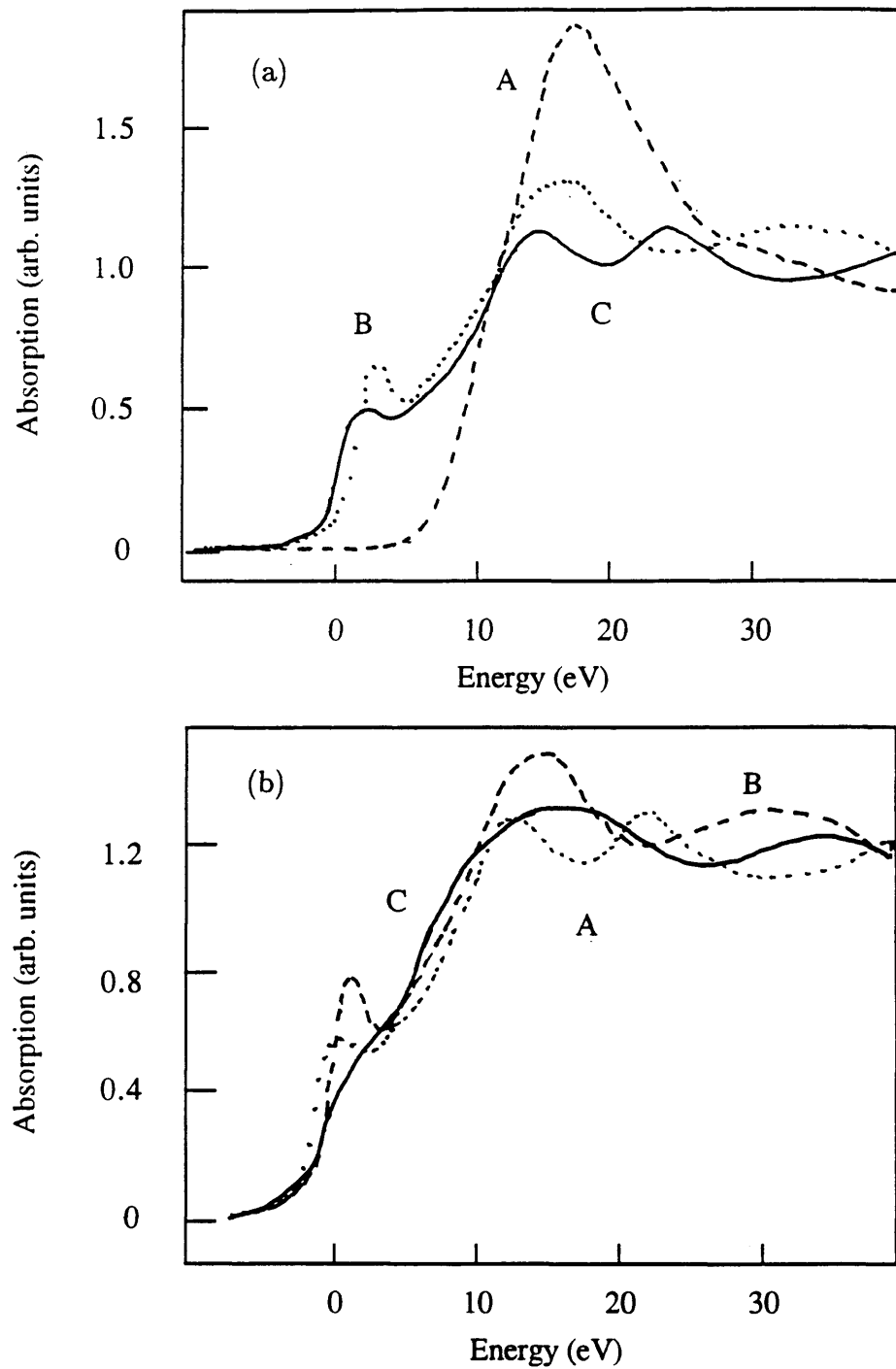


FIG. 2.4: Cu K edge XANES spectra

(a) Curve A: Cu^{++} ions in aqueous CuCl_2 solution; Curve B: Cu_2O (Cu^+) compound; Curve C: metallic Cu foil (Cu^0). (b) Curve A: metallic Cu foil (Cu^0); Curve B: Cu_2O (Cu^+) compound; Curve C: Cu monolayer on Au (100). Figures are taken from Tourillon [45].

metallic Cu^0 is due to the same d-band ($3d^{10}$) configuration. A shoulder below the edge for Cu^+ and Cu^0 is due to a dipole transition from $1s$ orbital to $3d^{10} 4p$. A strong white line in the Cu^{2+} scan is assigned to the multiple scattering paths of the photoelectron between Cu and O atoms [46]. This is a characteristic of Cu^{2+} . Fig. 2.4b shows that the energy position of the edge for a Cu monolayer is close to Cu^+ . The EXAFS results for Cu-O (1.97 Å), Cu-Cu (2.66 Å), Cu-Cu (3.72 Å) and Cu-Au (3.70 Å) measured from a monolayer of Cu on Au (100) led these authors to suggest (i) the first layer of the gold is reconstructed under the influence of the Cu monolayer and the distance of Au-Au decreases from 2.88 Å to 2.66 Å ; (ii) the Cu atoms are in 'atop' sites with an oxidation state close to Cu^+ ; (iii) the monolayer is stabilized by the influence of O atoms from water or sulfate ions. The EXAFS data for a bilayer of Cu on Au (100) shows that the main scattering is from Cu-Cu (2.59 Å and 2.90 Å). No O scattering was detected from bilayer deposition. No alloy formation was found in the underpotentially deposited Cu on gold in this case.

Underpotentially deposited submonolayers (0.3 monolayer and 0.6 monolayer) of Cu on a gold (111) substrate was also studied by Tadjeddine *et al.* [46] using *in-situ* x-ray absorption spectroscopy in a s-polarization geometry and in the fluorescence detection mode. The electrolyte used in this experiment was the same as the previous experiment [45]. They observed that Cu-O (1.95 Å) scattering appears in all cases with a 4.5 effective coordination number (N_{eff}) regardless of the Cu coverage, in contrast to IBM's result [47]. The Tadjeddine group confirmed, however, that O strongly interacts with the Cu atoms. Both experiments, discussed above, suggested that the bond lengths were dependent on the coverage, the time, and the direction of adsorption-desorption scan. The structure of the adsorbates changed from $(\sqrt{3} \times \sqrt{3})$ R 30° to a densely packed hexagonal c(5 x 5) when the deposition of the Cu adlayer

changed from 0.3 monolayer to 0.6 monolayer. As the coverage was continuously increased to one monolayer, the structure of the Cu adlayer reached the (1 x 1) epitaxial arrangement.

2.2.5 AFM Studies

The UPD of a Cu monolayer on Au (111) was also studied by Manne [48] with an Atomic Force Microscope (AFM). The electrolytes were 10^{-3} M CuSO_4 plus 0.1 M H_2SO_4 and 10^{-3} M CuSO_4 plus 0.1 M HClO_4 . Solutions were air saturated. The Au (111) was evaporated on mica with a surface area of 0.32 cm^2 . In the perchloric acid electrolyte, the images on bare Au (111) were very stable for a long time (over one hour). This suggested that perchlorate ions did not influence the bare Au (111) surface. Cu atoms formed a close-packed lattice structure with a lattice spacing of $2.90 \pm 0.2 \text{ \AA}$ in perchloric acid and $4.90 \pm 0.2 \text{ \AA}$ in sulfuric acid solution. The latter has a more open structure which may be influenced by the coadsorption of sulfate anions. Bulk Cu deposition on Au (111) formed a close-packed structure with a lattice distance of $2.60 \pm 0.2 \text{ \AA}$ for both electrolytes. Results from cyclic voltammetry showed that a Cu UPD formation in perchloric acid solution occurs at a more positive potential than in sulfuric acid solution. This suggests that the Cu-Au bond is stronger in perchlorate containing solution.

2.2.6 Summary

It is obvious to see at this point that not all of the experiments agree with each other. The EXAFS studies of Cu/Au (111) by Melroy and Cu/Au (100) by Tadjeddine, both measured s-polarization. No O was detected as a nearest neighbors from Melroy *et al.* while the Cu-O at a distance of 1.97 \AA was found by Tadjeddine.

The electrochemical environments, however, were not exactly the same for these experiments. Other differences are found between the AFM study by Manne and the EXAFS study by Melroy. Manne found a Cu-Cu distance of 4.90 Å while Melroy found a Cu-Cu distance of 2.92 Å, both in sulfuric acid.

Unfortunately, at this point, ambiguities between the different groups still exists because the experimental environments are different. We measured EXAFS from a large Pt substrate in order to obtain a high signal to noise ratio to provide a more accurate determination of the adsorption sites of Cu on a Pt surface. We also (for the first time) measured EXAFS from both s and p polarizations in order to get complete local environmental information because only those bonds whose interatomic vector has a projection that lies in the plane of polarization of the incident x-rays will contribute to the observed EXAFS (see section 3.2.2 for more information).

Chapter 3

THEORIES AND TECHNIQUES

3.1 Electrochemical Theories and Techniques

3.1.1 Underpotential Deposition(UPD)

Generally, two limiting cases are associated with electrodeposition of a metal on a foreign metal substrate [49]. One refers to systems in which the binding energy between adatoms and the substrate ($\psi_{Me'-Me}$) is relatively low compared to the binding energy of the bulk metal (ψ_{Me-Me}). The deposition occurs only in the potential region where:

$$\eta = (\mu(\theta)_{ad} - \mu_{metal}) \leq 0. \quad (3.1)$$

Here η is called the overpotential, and $\mu(\theta)_{ad}$ is the chemical potential of adatoms at coverage θ and μ_{metal} is the chemical potential of the metal substrate. Deposition in the overpotential region is always related to the bulk metal deposition. The kinetics of overpotential deposition or bulk metal deposition are controlled by condensation, nucleation and the growth processes [50].

The other limiting case, called underpotential deposition (UPD), refers to systems in which the binding energy of $\psi_{Me'-Me}$ highly exceeds the binding energy of ψ_{Me-Me} . The phenomenon of underpotential deposition was probably first found by Hevesy [19] in 1912. The UPD is the deposition of a submonolayer, monolayer or several monolayers of metal onto a foreign metal at potentials which are more positive than the potentials corresponding to the reversible Nernst potential of the bulk deposition. It was found [19] that adatoms are more strongly bound to the surface

of the foreign substrate than to the surface of its own species in the underpotential region:

$$\Delta\eta = (\mu(\theta)_{ad} - \mu_{metal}) \geq 0. \quad (3.2)$$

The UPD process presents a unique opportunity to study the coupling of a wide variety of electrochemical phenomena, including adsorption, charge transfer, surface diffusion, solution mass transport and double layer changes.

The difference between the chemical potentials shown in equation (3.2) is given by the following equation [19]:

$$\mu(\theta)_{ad} - \mu_{metal} = ne_0(E_{ad}(\theta) - E_{metal}) = Ze_0\Delta E_p \quad (3.3)$$

where e_0 is the positive electron charge, n is the number of electrons transferred in the half reaction (see Eq. (3.4)), $E_{ad}(\theta)$ is the electrode potential necessary to reach a coverage θ , E_{metal} is the Nernst potential (the potential from the Nernst equation) for the corresponding bulk metal deposition, Z is the valence number the adatoms, and ΔE_p is the potential difference between the bulk and monolayer desorption peaks which is called the underpotential shift. Consider the reduction of a species O at a cathode:



The equilibrium reversible Nernst potential E_r is then given by

$$E_r = E_0 + \frac{RT}{nF} \log \frac{a_{ox}}{a_{red}} \quad (3.5)$$

where E_0 is an electromotive series value for a specific electrode, R is the universal gas constant, and T is the ambient temperature. F is the faradaic constant, and a_{ox}

and a_{red} are activities of the oxidized and reduced species respectively. In our case the experiment is conducted at room temperature. Therefore, the Nernst equation can be expressed as:

$$E_r = E_0 + \frac{0.0592}{n} \log \frac{a_{ox}}{a_{red}} \quad (3.6)$$

Hevesy found that the equilibrium potential for a monolayer or submonolayer deposition should be modified to become:

$$E_{metal}(\theta) = E_0 + E_a + \frac{RT}{nF} \log \frac{[Ox]}{\theta} \quad (3.7)$$

where the activity of the solid phase is a function of coverage:

$$a_{red}(monolayer) = \begin{cases} \theta, & \text{for } 0 \leq \theta \leq 1 \\ 1, & \text{for } \theta \geq 1 \end{cases} \quad (3.8)$$

E_a accounts for the interaction between deposited species on the substrate surface and depends on the substrate material; $[Ox]$ is the concentration of the oxidized species. One can see clearly from Eq.(3.7) that $E_{metal}(\theta)$ is a function of the concentration of the metal ion and also depends on the metal substrate. The equilibrium deposition potential $E_{metal}(\theta)$ obtained from Eq.(3.7) is always more positive than the corresponding Nernst potential for the bulk phase.

The potential difference between bulk and monolayer desorption peaks (ΔE_p) in Eq.(3.3) has been found to be linearly related to the difference in the work function $\Delta\phi$ between the substrate and the adsorbate [19]:

$$e_0\Delta E_p = 0.5\Delta\phi. \quad (3.9)$$

Table 3.1: The Potential Difference Between the Bulk and Monolayer Desorption Peaks (ΔE_p)

<i>Metal ions/ Substrate</i>	<i>Supporting Electrolyte</i>	ΔE_p (V)	<i>Electrosorption Valence (γ)</i>
Cu ²⁺ /Pt	0.5 M H ₂ SO ₄	0.41	1.8
	0.1 M HCl	0.24	

This relation has been found to be very satisfactory for polycrystalline electrodes. Table 3.1 is reproduced from Kolb [19] and lists the underpotential shift ΔE_p of systems of Cu/Pt in different supporting electrolytes. A partial charge transfer is commonly observed in UPD. It is suggested [19] that the partial charge transfer is due to the difference of the Fermi energy of a foreign substrate and the energy of the adatoms. Therefore the electrosorption valence γ of adatoms is not always equal to the valence number of the adatoms participating in the reaction. The underpotential shift (ΔE_p) vs. work function ($\Delta\phi$) for many different systems is shown in Fig. 3.1.

It should be pointed out that adatoms are deposited onto a foreign metallic electrode due to the charge transfer from the electrode to cations from the solution. Therefore, the total charge which corresponds to the deposited (or desorbed) adatoms can be calculated from current (I) potential (E) curves known as a cyclic voltammogram. The total charge can be found from:

$$\Delta q = A^{-1} \int_{E_i}^{E_d} (I - I_d) \left(\frac{dE}{dt} \right)^{-1} dE, \quad (3.10)$$

where the initial deposition potential E_i is much higher than the ending deposition potential E_d for cation deposition, $\frac{dE}{dt}$ is the scan rate (which is usually a constant), A is the sample surface area, and I_d is the current due to the double layer effects which

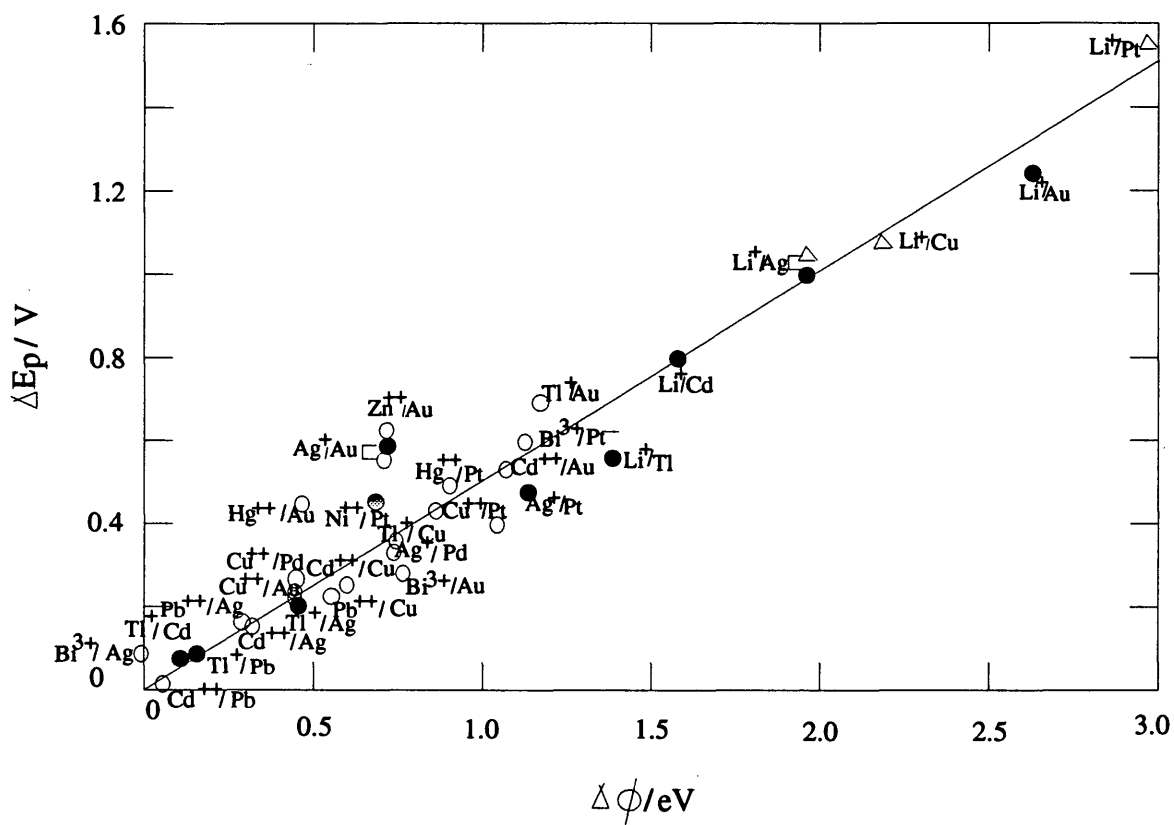


FIG. 3.1: Underpotential shift ΔE_p as a function of the work function difference ($\Delta\phi$) between the substrate and the adsorbate [19].

can be measured in cation free solution. It was found that monolayer adsorption on a polycrystalline surface finishes near a specific potential value, yielding one broad pronounced current peak in the cyclic voltammogram.

3.1.2 Energy Level Diagram of UPD

In order to understand the basic physical processes of UPD of adatoms onto a foreign metal substrate, one can assume a weak interaction between adatoms and the substrate, and use perturbation theory to find out the energy changes due to the interaction [51]. The energy level diagram of the isolated adatoms and the substrate is illustrated in Fig. 3.2a. ϕ is the work function of the metal (typically around 4 eV for transition metals) and E_f is the Fermi energy of the metal. The isolated adatom is characterized by its ionization potential V_i and its electron affinity A_i . When the adatom is brought into contact with the substrate, interaction between the adatom and substrate states result in a shift of the valence level from ϵ_{ao} to ϵ'_{ao} . The energy shift ϵ'_{ao} results from the interaction of adsorbates and substrate atoms. A study reported by Gadzuk [52] also shows that if the electron affinity of the adatom is below (or above) the Fermi energy of the substrate, a negative (or positive) ion was adsorbed (Fig. 3.2b or Fig. 3.2c). A neutral adatom is adsorbed when the electron affinity A_i lies above E_f and V_i lies below E_f . The energy states will be completely filled if a negative ion is adsorbed (Fig. 3.2b) and be completely empty if a positive ion is adsorbed (Fig. 3.2c). Of course this model is very simple and is only an approximation of what one would expect.

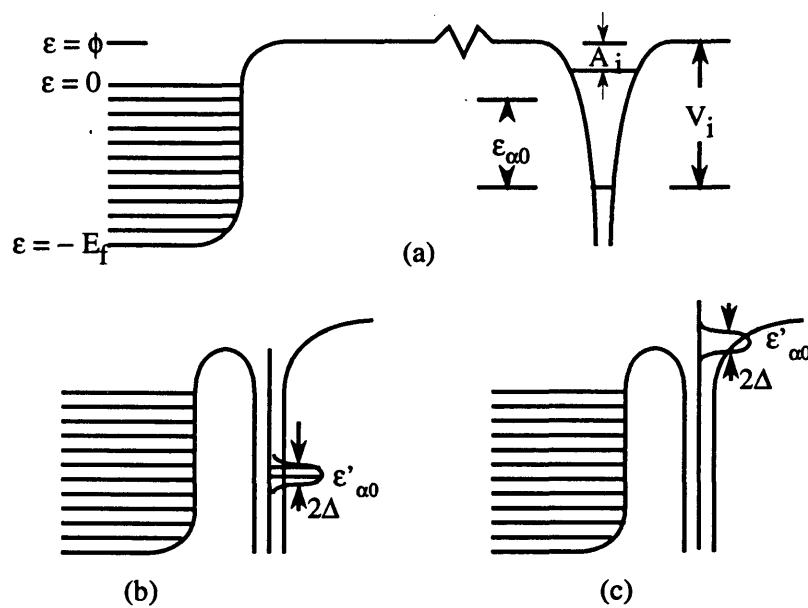


FIG. 3.2: Schematic diagram of energy level produced from Kolb
 (a). Energy level diagram of noninteracting metal adatom and foreign metal substrate; (b): Negative ion is adsorbed and the virtual state is completely filled; (c): Positive ion is adsorbed and the valence level is completely empty [52].

3.1.3 Density of States of the Adatom/Foreign Metal Substrate System

The density of states (DOS) of an interface between an adatom and a foreign metal substrate is closely related to the chemical bonding [28]. The density of states can be calculated using a self-consistent, semi-relativistic, all electron full-potential-linearized-augmented plane wave method (FLAPW) [28]. For example, an interfacial system of Cu/Pt can be treated as a 5-layer of Pt (001) slab with a copper monolayer of $c(2 \times 2)$ on top of the Pt. The model is created from the experimental results given by Kolb *et al.* [26]. The DOS of bulk Pt is shown in Fig. 3.3a. The characteristic peaks are at approximately -0.60 eV, -3.5 eV, -2.0 eV and the Fermi energy. The characteristic minimum is at approximately -5.0 eV. The surface DOS at the Fermi energy is very high (about 2 states/eV).

The DOS of a Pt surface is shown in Fig. 3.3b. The distinctive narrowing of the peak at about -5.0 eV is due to the loss of Pt-Pt nearest neighbor bonds at the Pt surface. The sharp peak at about -1.0 is increased in position compared to the DOS of the bulk Pt. The DOS of the Cu monolayer in Fig. 3.3c shows that the surface states are mainly in the energy region between -3.0 eV and -1.0 eV, which is the same region as the Pt surface states. Thus a strong interaction exists between the Pt surface and the Cu monolayer. One should notice that a distinctive minimum is found at approximately -2.0 eV for the surface of Pt (Fig. 3.3b). This peak is more pronounced and shifted toward the Fermi energy compared to the bulk Pt case (Fig. 3.3a). This is another feature to explain that the interaction between a metal adlayer and a foreign metal substrate is different from the interaction at the bulk metal surface.

The interfacial interaction between an adatom and a foreign metal substrate can

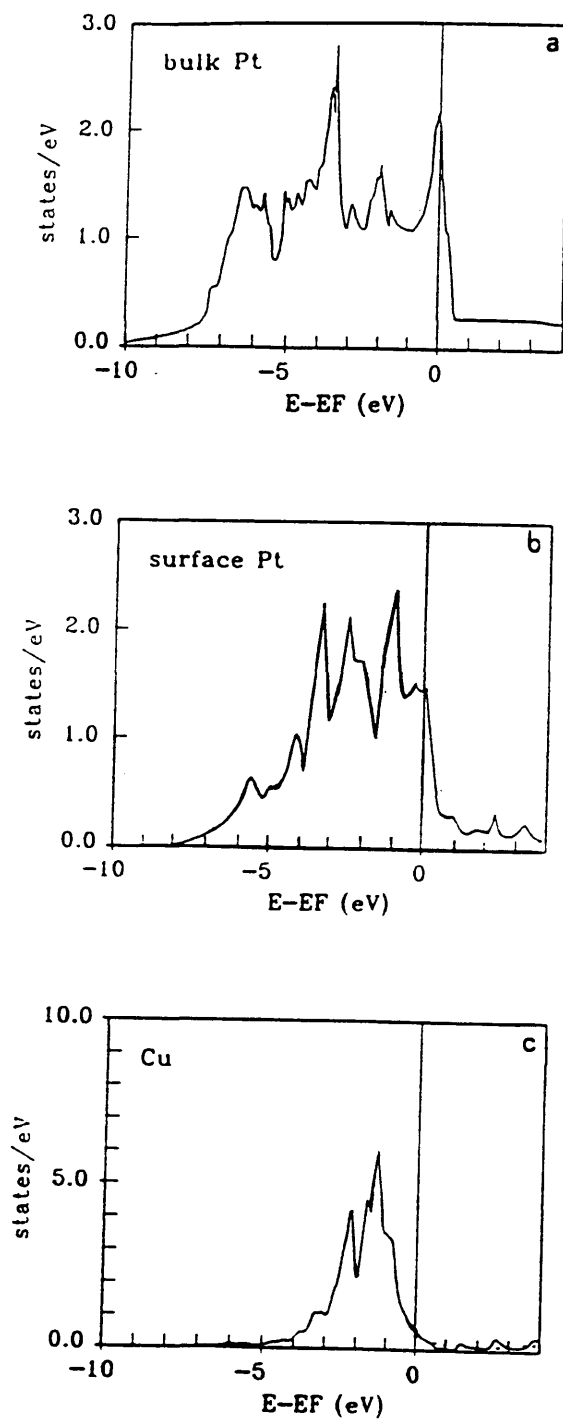


FIG. 3.3: Calculated electronic densities of states in states/eV with respect to Fermi energy [28]. (a) the DOS of bulk Pt; (b) the DOS of the Pt surface; (c) the DOS of the Cu monolayer.

also be illustrated by the electronic charge densities [28]. The valence charge density of the interface of the metal adatom/foreign metal substrate system is higher than that of the summed of the two isolated (metal adatom and foreign metal substrate) systems. Such calculations naturally include all interactions at the interface.

3.2 EXAFS Techniques and Theory

3.2.1 Introduction

Traditionally, x-rays are produced when high energy charged particles (electrons or positrons) collide with matter. The minimum wavelength (λ) in angstroms of the highest energy resulting x-rays is given by:

$$\lambda = \frac{\hbar c}{2\pi eV} = \frac{12,400}{V}(\text{\AA}). \quad (3.11)$$

Here \hbar is Plank's constant, c is the speed of light, e is the elementary charge, and V is the acceleration voltage in volts.

A broad background of x-rays (or white radiation) is produced when moving particles are slowed down or stopped by the target material and some of the energy lost is converted into electromagnetic radiation (white radiation). Because most of the electron energy is converted to heat, the white radiation has a very low intensity. In addition to the white radiation, characteristic lines are produced when the accelerating voltage increases beyond a certain critical potential (depending upon the target material). The inner shell electrons can be knocked out by the incident energetic electrons, leaving vacancies in core levels. As higher level electrons fill the core 'holes', x-ray photons are produced at characteristic energies given by the energy differences between two orbitals.

However, it is really hard to use traditionally x-rays for studying electrode/electrolyte interfacial problems. Especially, in an EXAFS experiment, we need high intensity x-rays to decrease the data acquisition time. Tunable x-rays are also needed for the EXAFS experiment because EXAFS spectra refer to the region 40-1000 eV above the absorption edge.

3.2.2 Synchrotron Radiation

Synchrotron radiation, produced by multi-GeV electron storage rings, has several advantages over the traditional method [24]: high intensity (from 10^3 to 10^6 higher than conventional x-rays), an extremely broad spectral range (from infrared to x-rays), a natural collimation, a high degree of polarization, a pulsed time structure, and a high stability.

These properties make synchrotron radiation a unique and rather extraordinary source for a wide variety of scientific and technological applications [24]. The major areas of use are: surface physics, catalytic chemistry, crystallography, amorphous materials science, trace element analysis, biochemistry, microscopy, lithography, and topography studies.

Synchrotron radiation was first observed at the General Electric 70-MeV synchrotron in 1947. The first synchrotron dedicated to the production of electromagnetic radiation was built in 1968. The 240-MeV storage ring Tantalus, associated with the University of Wisconsin. An excellent review paper about the history of synchrotron radiation has been written by Winick and Doniach [24].

3.2.3 Theory of EXAFS

The origin of EXAFS is now well understood [55]. When the x-ray photon energy is increased to a certain value ($E > E_{K\alpha}$), the deeply bound electrons (*e.g.* K-shell electrons) can be excited and cause an abrupt increase in the absorption coefficient which is proportional to the absorption cross section. The energy at the value of K_α is called the K-edge. There are basically four distinguishable regions in an absorption spectrum: pre-edge, edge, near-edge and post-edge. Extended x-ray absorption fine structure spectroscopy refers to the post-edge spectrum (oscillations in the absorption coefficient). The phenomenon of EXAFS was first explained by Kronig about a half century ago. Post-edge oscillations in the absorption coefficient are due to the modification of the final state of the photoelectron by the crystal [53], or by the atoms around the excited atom [54]. The origin of EXAFS is shown in Fig. 3.4. Fig. 3.4a shows an x-ray photon (with incident energy $\hbar\omega$) absorbed by an atom through the excitation of an electron from a core level j to an unoccupied, continuum state f . The final energy of the ejected electron ($E_f = \hbar\omega - E_j$) is greater than the Fermi energy (E_{Fermi}) of the solid. Here ω is the frequency of the incident photon. The excited electron waves (solid lines in Fig. 3.4b) propagate outward from the excited atom and a scattered wave (dashed line in Fig. 3.4c) from a neighboring atom is generated. The modulation in the absorption coefficient in the post-edge spectrum is due to the interference of the out-going electron waves with those back-scattered waves from neighboring atoms.

If one considers the scattering from more than one neighboring atom, the interpretation of the EXAFS would be very complicated. However, the multiple-atom scattering effect can be described by an effective interference path length which is the same as the sum of the scattering paths. In addition the multiple-atom scattering

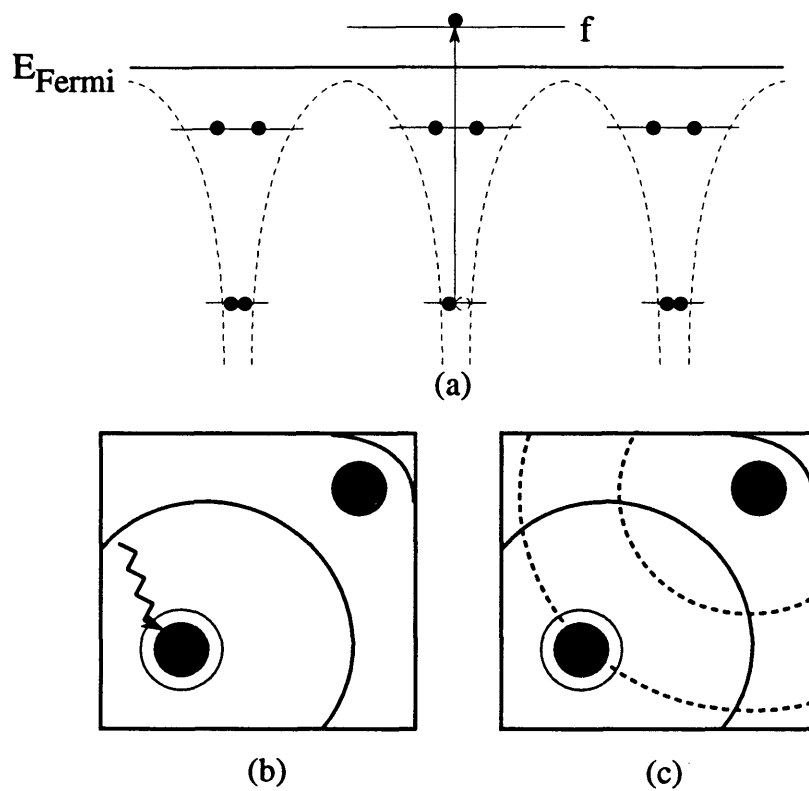


FIG. 3.4: Schematic diagram of origin of EXAFS (Hayes and Boyce, 1982)
(a). Photoionization; (b). Outgoing photoelectron wave (solid line); (c). Scattered wave (dashed line) from a neighboring atom interferes with the outgoing electron wave at the excited atom.

mainly contributes to the near-edge spectrum. Particularly, Lee and Pendry [57, 58] demonstrated that multiple-atom scattering causes a spread in phase which tends to cancel out. One way of understanding this cancellation is to note that if we have more than one neighbor, terms like $(r_i - R_j)$ will in principle be produced. Fortunately, all these terms exactly vanish, as has been shown using a Green's function technique [58]. Therefore, the problem can be simplified by considering the system as a short-range, single-electron, single-scattering system. The photoelectron emitted from the K-shell by absorbing an x-ray photon will travel as a spherical wave with a wave vector

$$k = \sqrt{\frac{2m}{\hbar^2}(E - E_0)} \quad (3.12)$$

and with a final state energy

$$E = \hbar\omega - E_{1s}. \quad (3.13)$$

Where E_0 is the final state energy corresponding to $k=0$. m is the mass of the electron and $\hbar\omega$ is the incident x-ray photon energy. The absorption cross-section of atom species α is given by Hayes and Boyce [55]:

$$\sigma_\alpha(\omega) = \sigma_\alpha^o(\omega)[1 + \chi_\alpha(\omega)], \quad (3.14)$$

and the EXAFS function is given by [55]

$$k\chi_\alpha(\omega) = \sum_\beta \int_0^\infty 2\text{Re}[e^{2ikr}\Lambda_{\alpha\beta}(k, r)]p_{\alpha\beta}(r)r^{-2}dr \quad (3.15)$$

with

$$\Lambda_{\alpha\beta}(k, r) \simeq -\left(\frac{2i\pi m}{\hbar^2}\right)t_\beta(-\mathbf{k}, \mathbf{k})e^{(-\frac{2r}{\lambda(k)} + 2i\eta_\alpha(k))}. \quad (3.16)$$

σ_α^o is similar to the absorption cross section of free atoms, which contributes a broad

background to σ_α . χ_α , the EXAFS function, has two parts: the energy dependent term $\Lambda_{\alpha\beta}(k, r)$ and the pair correlation functions $p_{\alpha\beta}$. $\Lambda_{\alpha\beta}(k, r)$ is the term accounting for the interaction between the final-state electron and the excited atom and the backscattering atoms. $p_{\alpha\beta}$ accounts for the radial distribution of the atomic species β about the central species α . $\int_0^\infty p_{\alpha\beta} r^{-2} dr$ is the total number of scatterers (β atoms) in the sample. The direct structural information is contained in the pair distribution function. t_β is the t-matrix of the scattering atom, $\eta_\alpha(k)$ is the phase shift due to the potential of the excited atom α in $l = 1$, λ is the mean free path of the electron and the damping term $e^{-\frac{2r}{\lambda(k)}}$ is the effect due to inelastic losses in the scattering process.

If there is more than one adsorbate, the contribution to the effective coordination number (N_j^*) of atoms around the central atom to the EXAFS is given by:

$$k\chi_j(k) = \frac{2N_j^*}{r_j^2} |\Lambda(k, r_j)| e^{-2k^2(\sigma_j)^2} \cos(2kr_j + \phi_j(k)). \quad (3.17)$$

Here σ_j is the Debye-Waller factor, which accounts for the thermal harmonic vibration and also static disorder [55]. The energy dependent phase shift includes: 1) the phase difference between outgoing and backscattered waves, simply equal to k times $2r_j$, with r_j the nearest distance from the neighbor; 2) the phase difference $\phi_j(k)$ between the excited atom and the backscattering atom, equal to the scattering of the electronic cloud of the excited atom; the backscattering of the nearest neighbor atom and the backscattering of the electronic cloud of the excited atom. The scattering of the electronic cloud of the excited atom is being considered twice here. The amplitude of the backscattering wave is dependent on the kind of neighbors and how far they are from the adsorbed atom. The sinusoidal EXAFS modulation is due to the interference of $\cos(2kr_j)$ with a frequency $2r_j$ in k -space. Such modulation can usually extend over 1000 eV beyond the edge. The EXAFS amplitude decreases as $1/r^2$.

EXAFS is fundamentally a bulk technique. In order to make it surface sensitive, one can employ a grazing incident geometry in the experiment to limit the penetration of x-rays into the sample by total external reflection [56]. Fig. 3.5 shows the grazing incidence geometry used in our experiment. If x-rays are incident at an angle α from air through water (neglect the absorption by water) onto a uniform dielectric (Pt substrate) with an index of refraction

$$n = 1 - \delta - i\beta, \quad (3.18)$$

with

$$\delta = \frac{N_0 e^2}{2\pi m c^2} \frac{Z + f'}{A} \rho \lambda^2, \quad (3.19)$$

and

$$\beta = \frac{\mu}{4\pi} \lambda. \quad (3.20)$$

Here N_0 is Avogadro's number, Z is the average atomic number, f' is the average of the real part of the scattering factor, A is the average atomic mass, ρ is the mass density, λ is the x-ray wavelength, μ is the linear absorption coefficient and the rest of the parameters have their common meanings. The angles of incidence and reflection are α , and the refracted angle is α' . Snell's law is

$$\cos \alpha = n \cos \alpha'. \quad (3.21)$$

In a small angle approximation,

$$\alpha'^2 = (\alpha^2 - \alpha_c^2) - 2i\beta, \quad (3.22)$$

where $\alpha_c = \sqrt{2\delta}$ (several tenths of a degree) is the critical angle for total external

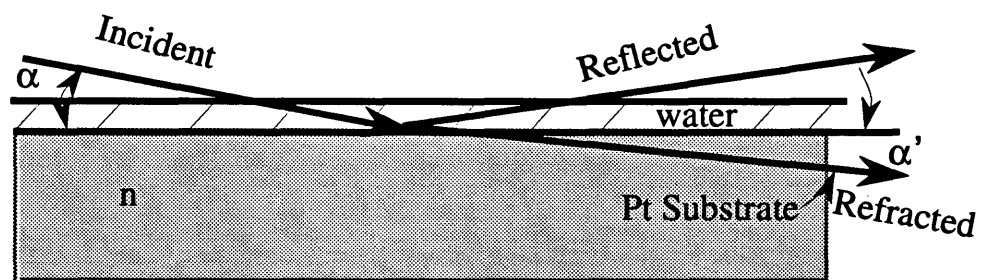


FIG. 3.5: Schematic diagram of grazing incident geometry. The angles of incidence and reflection are α , and the refracted angle is α' .

reflection. When α is very small, α' is very small too. Therefore x-rays travel almost parallel to the substrate surface.

In the EXAFS experiment, only those bonds whose interatomic vector has a projection that lies in the plane of polarization of the beam will contribute to the observed EXAFS. Thus polarization dependent studies can provide a wealth of additional structure and environmental information. If θ_j is the angle between the polarization vector of the electric field and the vector r_{ij} from the central atom to the i^{th} atom of the j^{th} shell. (see Fig. 3.6a), the effective coordination number can be written as [57, 58]

$$N_j^* = 3 \sum_i^{N_i} \cos^2 \theta_j, \quad (3.23)$$

where the summation is over atoms in the j^{th} shell. The factor of 3 arises from the fact that the integral of $\langle \vec{\epsilon} \cdot \vec{k} \rangle$ gives rise to 1/3 which is in the denominator of $\chi(k)$ [58]. For a polycrystalline or amorphous sample, the sum is over all angles, and

$$N_j^* = N_j, \quad (3.24)$$

the actual coordination number. The backscattering amplitude can thus be expressed as

$$A_i = N_i \cos^2 \theta_j. \quad (3.25)$$

In a surface experiment things are different [59]. If the angle between the interatomic vector and the surface normal vector (see Fig. 3.6b) is ϕ , then the amplitude of the backscattering of s polarization is

$$A_s = N_i \frac{\sin^2 \phi}{2} \quad (3.26)$$

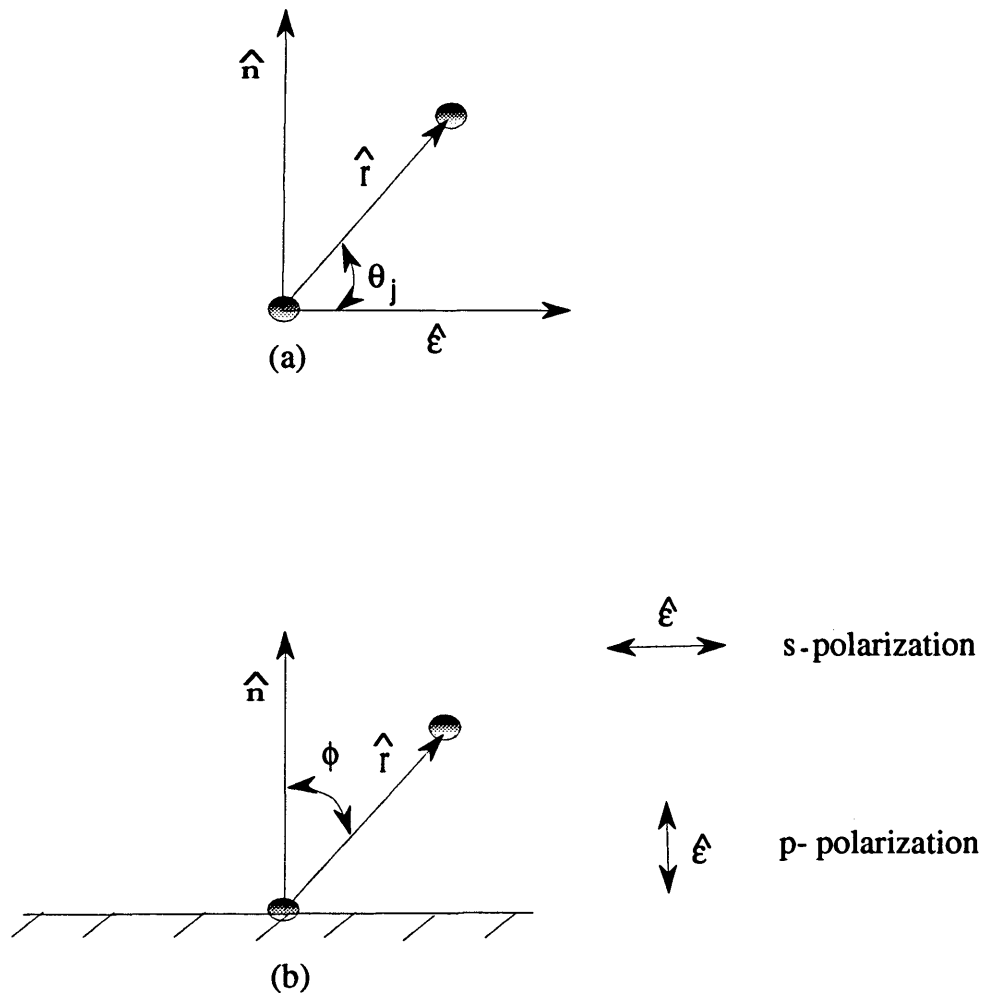


FIG. 3.6: Schematic representation of angles between (a) an interatomic vector and the plane of polarization and (b) the interatomic vector and the surface normal vector.

with the averaging through the plane of polarization and the amplitude of the backscattering of p polarization is

$$A_p = N_i \cos^2 \phi. \quad (3.27)$$

One can see from Eqs. (3.26) and (3.27), the total number of neighbors (N_i) of a given type therefore is independent of the polarization angle.

The purpose of EXAFS experimental studies is to obtain $p_{\alpha\beta}$ and extract the structure information from $k\chi_j(k)$. This can be usually done by Fourier transformation of $k\chi_j(k)$. The structural information contained in the EXAFS signal is the distance from the adsorbing atom to the j^{th} shell and the number of atoms in that shell. Theoretically, this information is available for all shells surrounding the central atom. In practice, due to σ_j^2 , $\lambda_j(k)$, and the limited data range, usually only the first few shells are recognizable. The Fourier transform of $k\chi_j(k)$ is

$$\phi_\alpha(r) = \sum_\beta \int_0^\infty p_{\alpha\beta}(r') r'^{-2} \xi_{\alpha\beta}(r - r') dr'. \quad (3.28)$$

and $\xi_{\alpha\beta}$ is in the form of

$$\xi_{\alpha\beta}(r - r') = FT[W(k)\Lambda_{\alpha\beta}(k, r)], \quad (3.29)$$

where $\phi_\alpha(r)$ is a sum of ξ peaks located at r , which is determined by the peaks in $p_{\alpha\beta}$, $\xi_{\alpha\beta}$ is the Fourier transform of the product of $W(k)$ and $\Lambda_{\alpha\beta}$, $W(k)$ is a window function introduced to minimize the loss of structure resolution. The exact form of the window function will be discussed in the next section. The r' in ξ , which arises from the mean free path factor in Λ , has been suppressed in Eq. (3.16).

The data analysis of K-shell EXAFS is based upon Eqs. (3.12 to 3.17) and Eqs. (3.23 to 3.29). It is also possible to measure EXAFS in the absorption coefficient for

the photoexcitation of less tightly bound electrons (*e.g.* from L- or M-shells). Unlike electrons from the K-shell, these electrons are characterized by a mixture of final state angular momenta. This makes the interpretation of experiment more complicated. However, many of the principles in the preceding treatment can be applied to the other shells as well.

By analyzing the data, one can obtain information about the nearest neighbor distance, the number of near neighbors and the type of neighbors.

3.2.4 Data Analysis

The data analysis procedures have been developed by the XAS group at RPI, under the direction of Prof. T. M. Hayes. Most of the data were analyzed by Dr. J. Pant and Dr. L. Lurio at RPI.

Data Averaging We usually accumulated 15 to 20 good scans, approximately 30 minutes each, to obtain better signal to noise resolution. A problem often complicating the data addition is that the energy calibration in the x-ray monochromator is not the same from scan to scan. Because of the mechanical linkage problem of monochromator, the near threshold varies with the incident beam [58]. In this work, we calculated E_j^o (the threshold energy for copper foil) from the transmitted spectrum of copper foil which was measured at the same time for each fluorescence spectrum. The calculation was as follows (see Fig. 3.7): the pre-edge and post-edge were fitted as a first order Chebyshev polynomial with a step in between. The fitting curve should bisect the post-edge oscillations. The distance between two fitting curves is determined as the edge height. The edge was fitted as a straight line which intersects the pre-edge fitting curve and post-edge fitting curve. Take the half length of the edge fitting curve between the intersection of pre-edge fitting curve and the post-edge

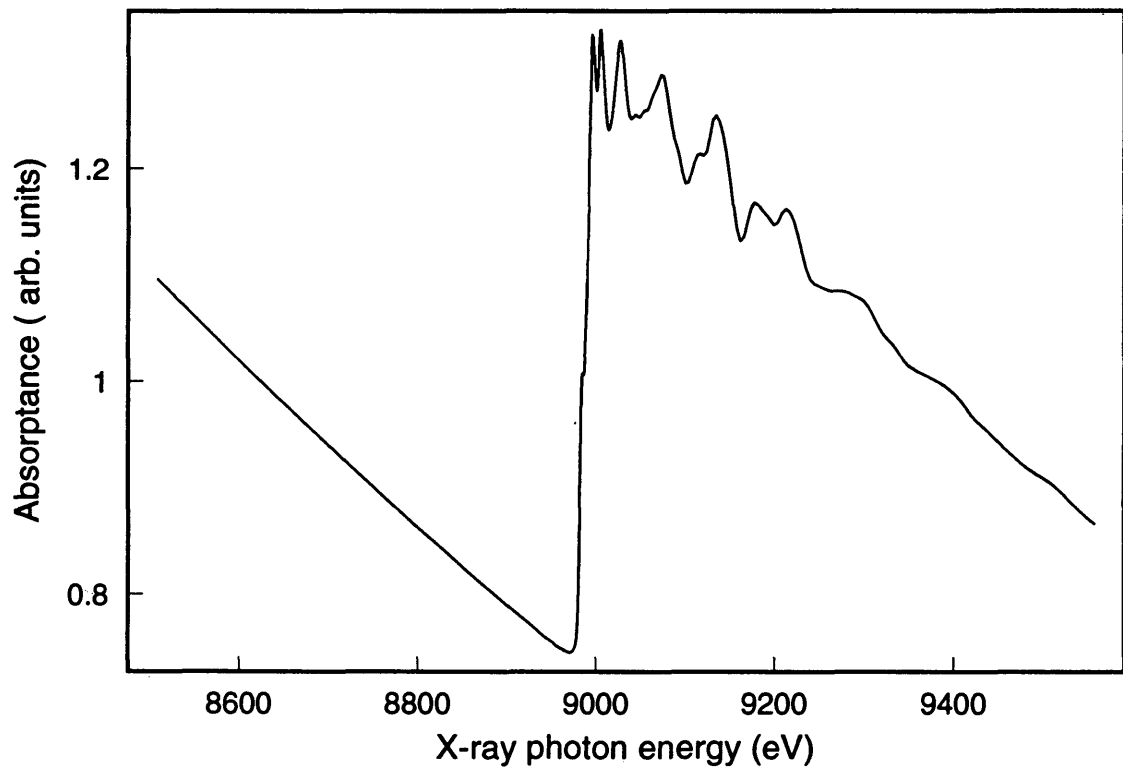


FIG. 3.7: Absorption coefficient of copper foil standards

fitting curve and drop the point to the energy axis. The corresponding energy then is called E_j^o . Therefore, the energy shift for each data set with respect to the theoretical value can be calculated from

$$\Delta(E)_j = E_{theory}^o - E_j^o, \quad (3.30)$$

where E_{theory}^o is the edge energy found from any x-ray reference book (*e.g.* 8979 eV for a Cu-1s). The absorption coefficient for summed data is

$$\mu(E) = \sum_{j=1}^{j=N_s} \mu_j(E + \Delta(E)_j). \quad (3.31)$$

N_s is the number of the data sets.

Another problem in accumulating data files is anomalously deviant points in the data set. The data file was discarded if it look really noisy. Otherwise these deviations can be replaced by parabolic interpolation from neighboring points.

Background Removal In this work, we have used EXAFS spectroscopy in the fluorescence detection mode. The x-ray absorption coefficient $\mu(E)$ for the fluorescence detection mode is defined as:

$$\mu(E) \sim \ln \frac{I_f}{I_0}. \quad (3.32)$$

Here I_0 and I_f are the incident and fluorescence x-ray intensities, respectively. And $\mu(E)$ can also be found as:

$$\mu(E) = \mu_0(E)(\chi(E) + 1) + \mu_{bg}(E). \quad (3.33)$$

Here $\chi(E)$ is the EXAFS function discussed previously, $\mu_0(E)$ is the absorption coefficient of an isolated atom, and $\mu_{bg}(E)$ is a slowly varying background. The background absorption $\mu_{bg}(E)$ is due to the photoexcitation of electrons that are less tightly bound than K-shell electrons. $\mu_{bg}(E)$ is approximated as a polynomial of the form: $A + B(\hbar\omega)^C$. For a given A, B and C (integer), $\mu_{bg}(E)$ can be determined by a least squares fit to the absorption coefficient in the region of 800 eV to 200 eV below the K-edge. Fig. 3.7 shows the absorption coefficient of copper foil standard as a function of x-ray photon energy. $\mu_{bg}(E)$ decrease with increasing the incident energy for transmission detection mode.

For the fluorescence detection mode, $\mu_{bg}(E)$ increases slowly with increasing incident energy. This is because the fluorescence efficiency increases with the increasing incident energy. For our experiment, the background is not trivial and there are many effects [59]: 1) The energy efficiency of the detectors and their absorption cross sections. For the I_0 detector, N_2 gas was used to absorb the incident x-ray for the purpose of detecting the intensity of the incident flux. N_2 (gas) absorbs less efficiently as the incident energy increases and the absorption intensity (I_0) increases as the incident energy increases, 2) The Compton scattering from the water. The Compton scattering from the water increases as the photon energy increases, 3) Compton and elastic scattering from the platinum substrate. This unmodified scattering also increases with increasing photon energy, 4) The fluorescence from our nickel filter which decreased with increasing photon energy. This fluorescence partially compensates of the background that was produced from 2) and 3), 5) The fluorescence from the K_α process remains approximately constant as the photon energy is increased. Hence, $\mu(E) \sim \ln \frac{I}{I_0}$ will increase as the incident energy increases. However, this background is always related to other effects, such as: beam harmonics (photons with frequencies

of 2ω , 3ω *et al.*). In our experiment, beam harmonics were partly removed by a Ni mirror in the beam line and by using a Si (111) crystal in the monochromator.

The procedure for finding $\mu_{bg}(E)$ (which is usually unknown) for our experiment is to fit the pre-edge absorption curve. As mentioned previously the pre-edge and the post-edge absorption curves in this work are fitted with the first order Chebyshev polynomial with a step in between. Chebyshev polynomials were used because they are orthogonal to each other making the least squares equations easy to compute. If the pre-edge curve and the post-edge curve are fitted properly, and the edge height is close enough, the post-edge fitting curve $\mu'(E)$ should go through the middle of the oscillating part throughout the whole post-edge region. Then $\mu'(E)$ can be considered as $\mu_{bg}(E)$. The next step in data analysis is to obtain $\mu_0(E)$. $\mu_0(E)$ is approximated as a polynomial of 4th or 6th order in $\sqrt{(E - E_0)}$. The parameters were chosen by a least squares fit to the K-shell EXAFS. The fitting region is from the 'white line' to the upper limit of the data range.

Extraction of EXAFS Function χ The EXAFS function χ can be extracted through Eq. (3.33) by dividing by $\mu_0(E)$. It can also normalize the EXAFS properly to the number of copper atoms. $\chi(E)$ can be converted to $\chi(k)$ via Eq. (3.12). As we know, the signal to noise ratio of the absorption coefficient decreases gradually when the photon energy increases. So, the EXAFS function $\chi(k)$ is multiplied by k in all of our work in order to help to bring out the amplitude higher in the high energy region. $k\chi(k)$ has been shown to be independent of the order of the Chebyshev polynomial for low orders. However, other people use $k^n\chi(k)$ with different n (but usually less than 10). Since n in $k^n\chi(k)$ effects the peak position and peak heights a great deal, therefore it is important to keep n the same in all the data analysis.

The $k\chi(k)$ for a copper foil standard is shown in Fig. 3.8. The broad peak

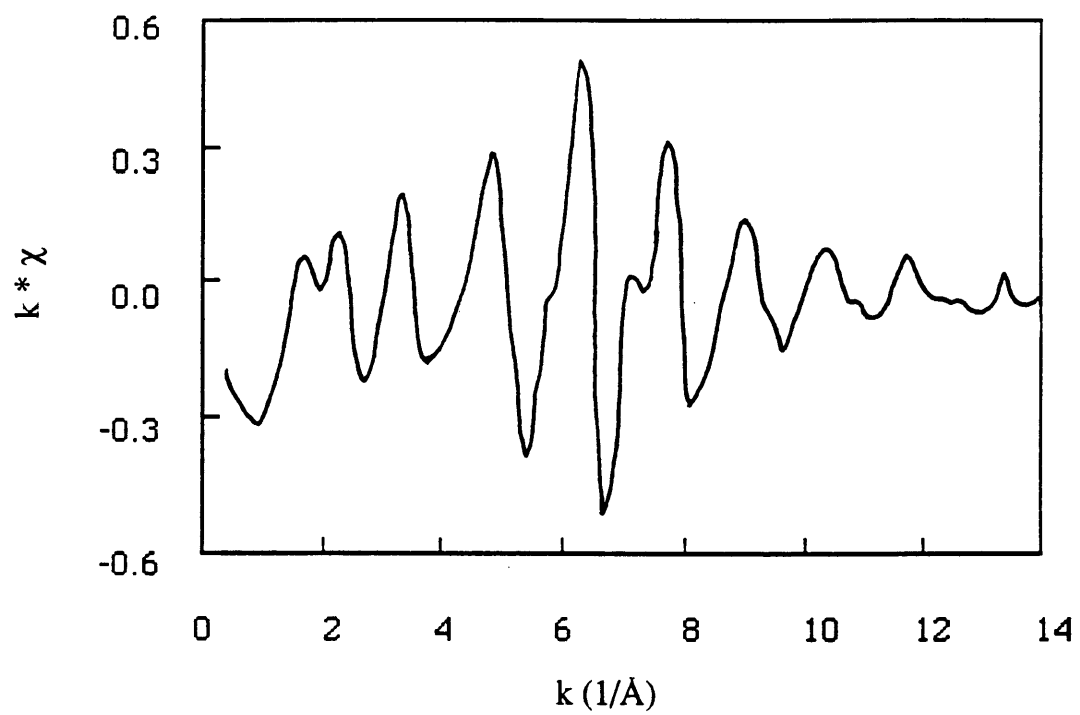


FIG. 3.8: The EXAFS modulation $k\chi$ on the copper k-shell absorption cross section.

at about $\Delta k \simeq 1\text{\AA}^{-1}$ is the threshold peak in Fig. 3.7. The EXAFS starts above that peak and extends beyond the upper limit (about 1000 eV above the edge). The structural information from $k\chi(k)$ can be analyzed in k-space or in r-space (r-space structure extraction will be discussed in next section). The methods developed by Hayes and Boyce exploit an r-space fit. The many near-neighbor positions create many spatial frequencies which are difficult to separate from one another except for simple situations (no overlap of near-neighbor positions). It is common to Fourier transform $k\chi(k)$ into r-space. Ideally, near-neighbor distances can be separated in r-space. A window function $W(k)$ is used to eliminate the undesired effect from the low frequency region (white line). Fig. 3.9 shows the FT of $k\chi(k)$ of the copper foil sample using a square window with Gaussian broadening of half width of 0.5\AA^{-1} . The solid line (dashed line) is the real part (magnitude) of $\phi(r)$. The signals from the first three shells are shown in the figure. Note that peaks are shifted to the left because of the k dependence of the phase shift and the phase of t_β in the expression for Λ (see Eq. (3.16)).

Extraction of Structure Information in r Space All our structure information are extracted from the Fourier transform of $k\chi(k)$ based on Eq. (3.15). Standards, Cu_2O , CuO , copper foil, CuS and a Cu/Pt alloy with 1% of copper, are used in this experiment to help determine the atom-dependent phase shift for the backscattered waves. These data form the basis for interpretation of the Cu adlayer results. The pair function $p_{\alpha\beta}(r)$ in Eq. (3.15) can be represented as a linear combination of shifted and broadened peaks from standards. This can be done through the following procedure: First, signatures are theoretically calculated. The signatures are calibrated by reference to the standards and then fit to the data. Since the neighbor distances are known in this case, the phase shift can be determined. For a given

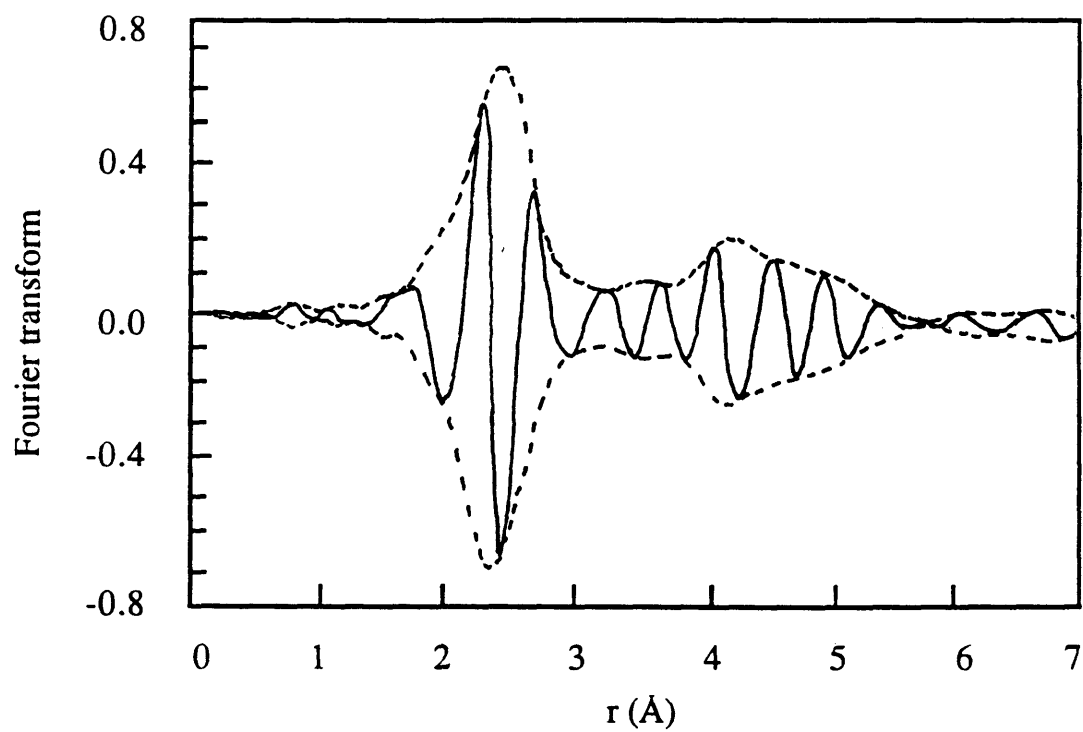


FIG. 3.9: Fourier transform $k\chi$ of copper foil standard

Table 3.2: Parameters from Theoretical Calculation for Standards

<i>Signature</i>	<i>NND(Å)</i>	<i>Number of NN</i>	<i>SND(Å)</i>	<i>Number of SN</i>
Cu-Cu	2.55	12	3.61	6
Pt-Pt	2.77	12	3.92	6
Cu-O	1.84	2	2.56	2
Cu-S	2.19	3	2.33	4

absorber/scatterer combination, the phase shifts can be transferred to any compound with the same absorber/scatterer combination without any problem. This is called phase transferability and is commonly used in EXAFS data analysis [58]. The shape of the peaks in the model $p_{\alpha\beta}$ need not be constrained during the data fitting and parameters (amplitude, phase shift and the Debye Waller factor) in $p_{\alpha\beta}$ can be varied until the ‘best’ fit is reached which corresponds to a minimum residual error R (from Hayes and Boyce):

$$R^2 = \frac{1}{2N} \sum_i^N \left[\frac{[\Re(\phi - \phi_m)]^2}{(\Re\phi)^2 + (\Re(d\phi/dr))^2} + \frac{[\Im(\phi - \phi_m)]^2}{(\Im\phi)^2 + (\Im(d\phi/dr))^2} \right] \quad (3.34)$$

here N is the number of points in the range of fitting. Thus, the number of near-neighbors, the near-neighbor distances and the widths of the peaks are obtained by comparing the experimental peaks to the signatures (*e.g.* r_{Cu-Cu} for copper foil standard) from standards. The parameters from the theoretical calculation are listed in Table 3.2. In Table 3.2, nearest neighbor distance (NND), second neighbor distance (SND) and the number of the neighbors with respect to the near-neighbors are listed. The results are calculated from the known structure. For standards Cu-O, NND and number of NN are calculated from Cu_2O and SND and number of SN are calculated from CuO. The parameters for Cu-S are calculated from CuS.

3.3 Experimental

3.3.1 Substrate Preparation

Float glass substrates (10" long by 1" wide by 3/8" thick) were purchased from a local glass company (Glass Specialists) and were cleaned according to the method in Appendix A. The flatness of the glass bars was within 50 nm based on interferometry measurements. All Pt substrates were prepared at the Stanford Synchrotron Radiation Laboratory (SSRL). The coating procedure for our Pt substrates is the same as is used for synchrotron radiation mirror coating. A 1000 Å Pt film was deposited using electron beam (e-gun) evaporation at a rate of 5 Å/s. In order to increase the adhesion between the Pt and the glass, 200 Å of Cr was deposited prior to the Pt evaporation at a rate of 1 Å/s. The chamber pressure was 10^{-9} and 10^{-8} torr for Cr and Pt evaporations respectively.

3.3.2 Cell Design

The design of the electrochemical cell is very important in this experiment. Several factors should be considered: the scale, the electrode geometry, the chemical reactivity of the system, the working temperature, and the fluid control in the system [2]. One also needs to consider contamination of the cell from the experimental atmosphere. Our special sample cell was made from Teflon polytetrafluoroethylene (PTFE) polymer, which is the most chemically resistant plastic. It is inert to most chemicals, even at elevated temperatures, except fused alkali metals, chlorine trifluoride, and fluorine at elevated temperatures and pressures [2].

A schematic diagram of the cell is shown in Fig. 3.10. The dimensions of the rectangular Teflon sample chamber (Fig. 3.10b) are 32.5 cm in length by 8.5 cm in width by 2.0 cm in height. There are 24, 1/4" diameter, tapped holes from top

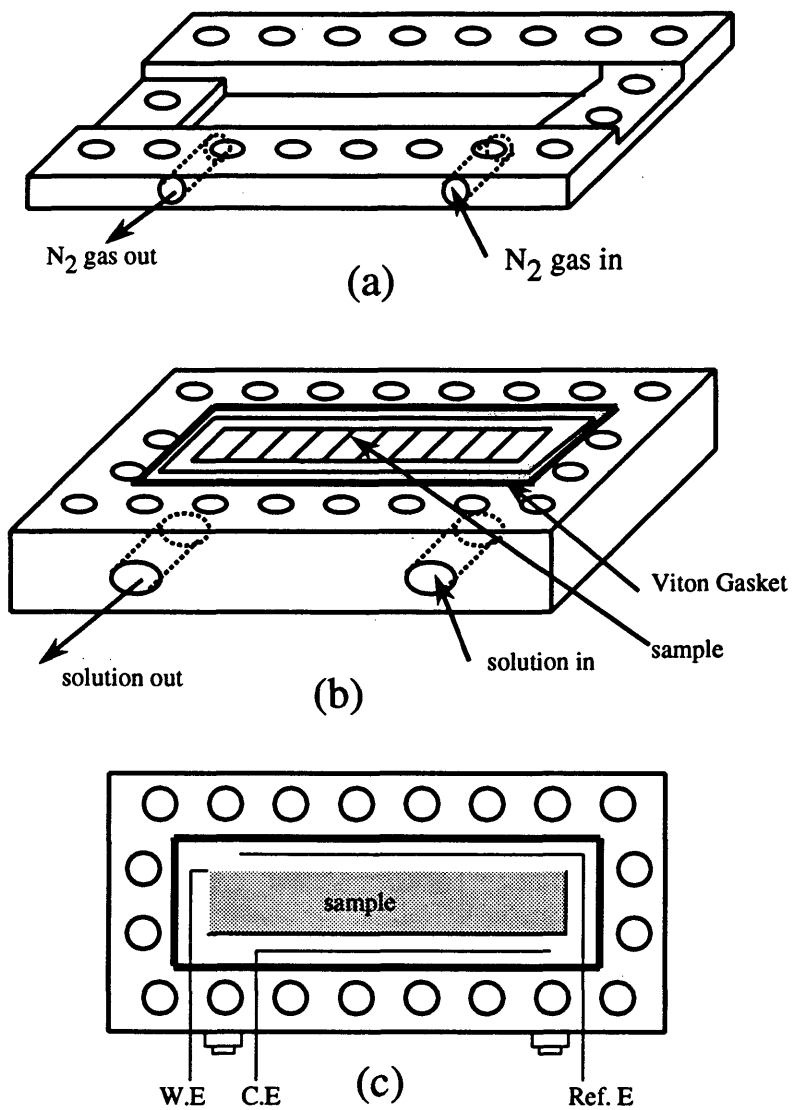


FIG. 3.10: Schematic diagram of the electrochemical cell
(a): Cell flange; (b): Electrochemical cell; (c): Top view of the electrochemical cell.

to bottom around the cell which are used to hold a flange (Fig. 3.10a) made from stainless steel. Between the flange and the Teflon chamber, a Kapton film (0.5 mil thick) was used as a window to close the cell. This thin Kapton film is inert to the experimental environment and is transparent to light and x-rays. A Viton gasket, 20.5 cm in diameter, was placed between the Kapton window and the Teflon chamber to provide a water-tight seal. The glass bar sample was placed in the middle of the cell. The top of the glass bar is slightly higher than the flange. In this configuration, the flange does not obstruct the x-rays from reaching the sample through the Kapton window, in the grazing incidence geometry. A varnished Cu wire was used to contact the substrate surface and was brought out of the cell through a force fitting hole on the side of the Teflon chamber. The contact between the Pt film and the Cu wire was furnished through a soldered connection with several layers of 'Wet and Wild' nail polish coating. A quick-set epoxy was used between the silver paint and the nail polish to prevent the nail polish from dissolving the silver paint and to provide greater mechanical strength to the contact. Pt and Cu wires were used as counter and reference electrodes, respectively. The purity of the copper wire was measured by EDX in the SEM in the Metallurgy department at CSM. The result showed that no other impurities could be detected by the system. The counter and the reference electrodes were placed on the opposite side of the substrate and parallel to the substrate surface (Fig. 3.10c) to minimize non-uniformities. The reference electrode is placed parallel and close to the working electrode to minimize the error in potential associated with the ohmic drop (iR) between the reference and the working electrode in the solution. Both the counter and the reference electrodes were brought out of the cell through tight fitting holes which were on the same side of the output hole of the working electrode. Three electrodes were doubly sealed with quick-set epoxy outside of the

cell around the force fitting holes. Solutions were easily pumped through the Teflon fittings with an external solution system. The cell was easy to clean by flushing with distilled water.

In order to prevent O_2 from penetrating the Kapton window into the solution, a double-Kapton window is used to allow N_2 to flow through the gap between the two Kapton windows in a configuration with the second Kapton window on top of the flange.

The three-electrode system allows us to measure the current passing through the working and counter electrodes. The potential of the working electrode was measured with respect to the reference electrode. Compared to a two electrode system, the three electrode system is used to avoid current being drawn across the reference electrode [2].

3.3.3 Solution Preparation

The solution was prepared from water filtered by a Millipore water purification system with a conductivity of less than 1.8×10^{-7} [ohms/cm] $^{-1}$. The solution was purged with zero grade N_2 for more than 4 hours prior to the use. Reagent-grade 0.5 M H_2SO_4 and 2×10^{-4} M $CuSO_4$ were used in the experiment.

3.3.4 Experimental Setup

Electrochemical Instrumentation Fig. 3.11 is a schematic diagram of our electrochemical setup for the Cu layer preparation. A RDE4 potentiostat from Pine Instruments was used to control the interfacial potential between the working electrode and the reference electrode. A triangular sweep generator in the RDE4 Potentiostat supplied the scanned interfacial potential to the working electrode. A X-Y

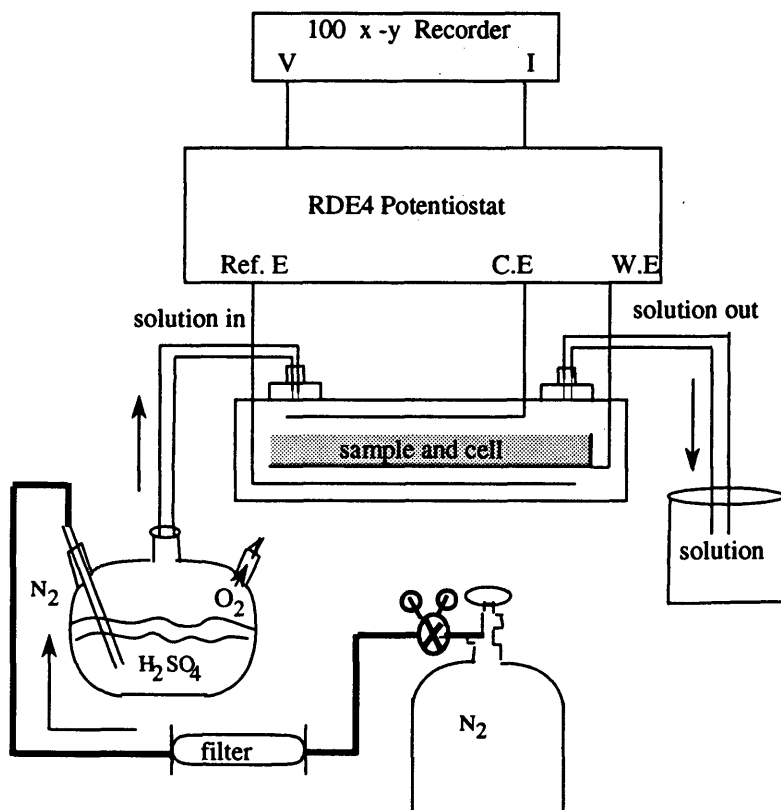


FIG. 3.11: Schematic diagram of the electrochemical set up

recorder from Houston Instruments (Model 100) was used to record cyclic voltammetry.

The EXAFS Setup A schematic diagram of our experiment for the EXAFS study is shown in Fig. 3.12. We have used five detectors in the experiment. I_0 , I_1 and I_2 are ion chambers provided by the Biostructures Primary Research Team, which operates beam line X9 at the National Synchrotron Light Source. An ionization chamber detector is the simplest x-ray detector. It was a low-noise current detector to measure x-ray flux rather than counting individual photons. An ionization detector usually contains a chamber filled with a gas and two parallel electrodes. When an x-ray enters the chamber, it will photoelectrically be absorbed by gas atoms or molecules to produce either Auger electrons or fluorescence photons. The energetic electrons will produce additional electron-ion pairs by inelastic collision. The efficiency of producing an electron-ion pair is dependent on the type of the filling gas (see Fig. 3.13), the geometry of the chamber, and the voltage applied across the two electrodes. The fluorescence photons will either escape or be photoelectrically absorbed. The voltage which is applied to the parallel electrodes produces an electric field of about 100 V/cm and separates the electrons and ions. When these electrons and ions are collected at the electrodes a current can be generated. This current is proportional to the product of the number of photons absorbed by the gas.

The intensity of the incident x-ray beam and reflected signal are measured by I_0 , and I_1 respectively, with a chamber size 27.0 cm in length by 15.0 cm in width by 7.0 cm in height filled with nitrogen. Nitrogen gas is used in those detectors because it absorbs very little beam. I_2 was used as a reference detector to measure the copper foil transmitted spectrum.

Another detector we used is a high-purity Ge crystal detector. We used this

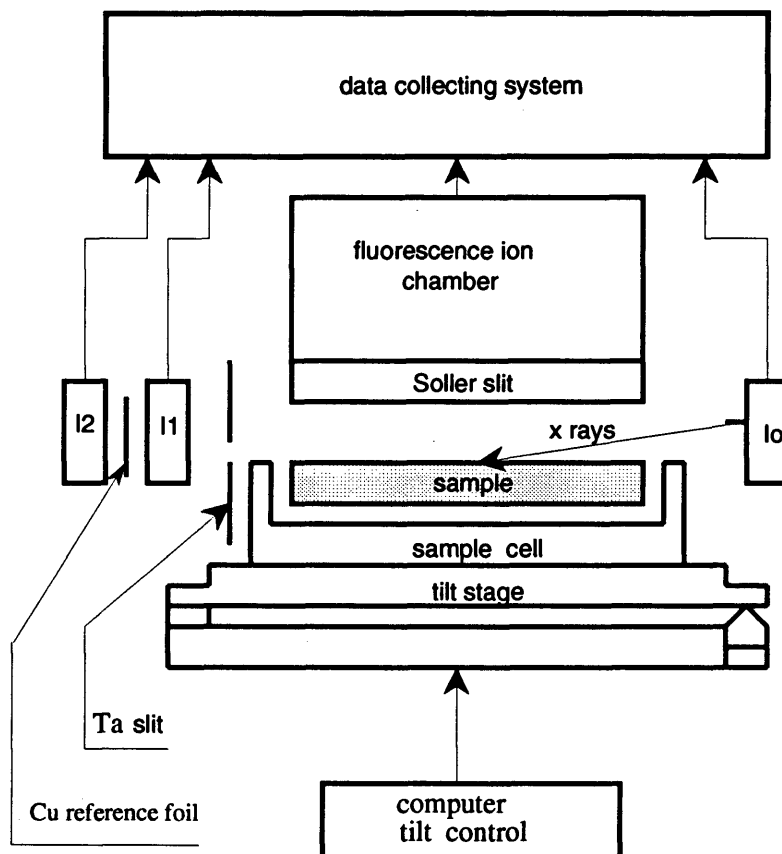


FIG. 3.12: Experimental setup of EXAFS study.

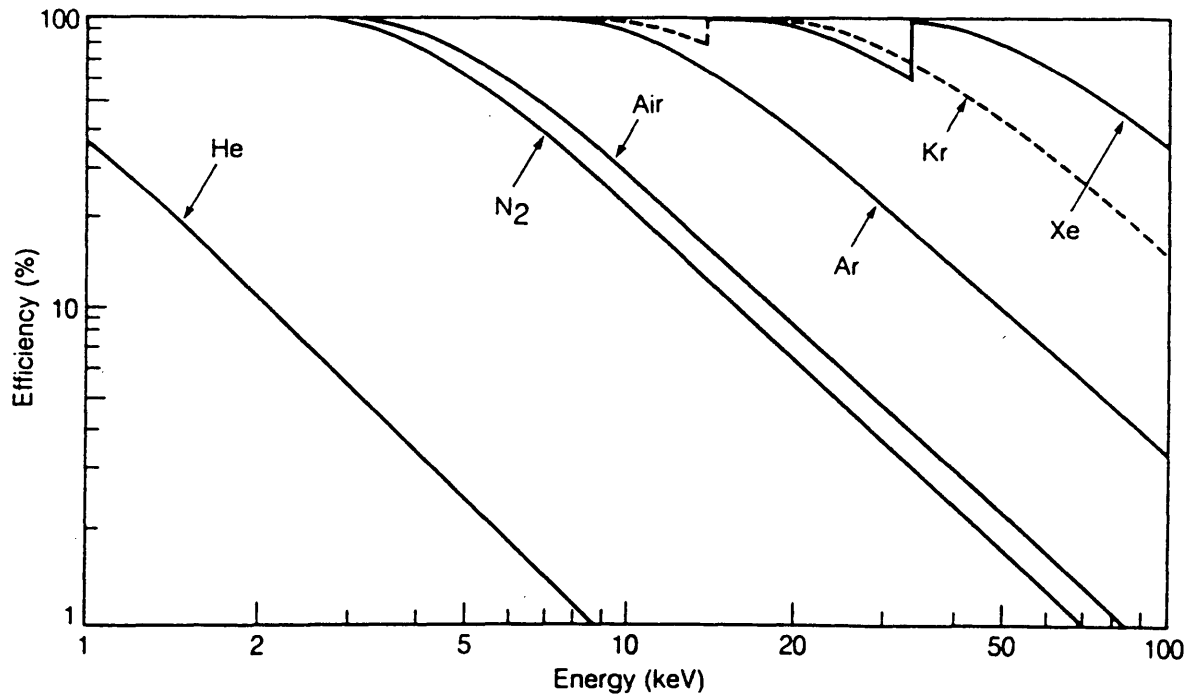


FIG. 3.13: Efficiency of a 15-cm long gas ionization chamber as a function of energy, for different gases at normal pressure [60].

detector to study the harmonic components of the incident x-rays and set the angle on the filter mirror to reduce third-order energies (where second order contributions are forbidden by using Si (111) crystals in this experiment). The higher-order radiation can be eliminated by grazing reflection from a Ni mirror (which will be discussed in section 3.3.5). The total energy load of the Ge crystal limits the dynamic range to less than 10^4 counts per second. In the special design of our experiment, we obtained a much larger signal than the limit of the detector from the sample, therefore the Ge detector could not be used in the actual EXAFS data acquisition.

In the present work, we used a special detector for acquiring the EXAFS signal. The detector contained a homemade ion chamber filled with argon. Argon was used to absorb all the fluorescence as much as possible. This ion chamber has five-electrodes with a rectangular window whose size is 32.0 cm in length by 8.0 cm in width by 15.0 cm in height which matches the size and shape of our sample. This detector is placed at 90° to the beam right above the sample in order to minimize the Compton scattering from water. An ultra-low noise pre-amplifier [61] and high voltage (45 volts) batteries were used. A Ni ($Z=28$) foil filter was placed in front of the detector to preferentially adsorb the x-rays that were scattered from the sample. The filter attenuated the background while only slightly attenuating the desired signal at the Cu ($Z=29$) fluorescence energy. A Söller slit was placed between the Ni foil filter and the ion chamber to permit the fluorescence signal photons to travel from the sample to the detector but block most of the filter refluorescence. Copper foil was placed between the I_1 and the I_2 detectors for the reference spectrum.

3.3.5 X-9 Beam Line

The experiment was conducted at the X-9 beam line at the Brookhaven National Synchrotron Light Source (NSLS). All this instrumentation is provided by the National Biostructures Primary Research Team as part of the General User Program at NSLS. Fig. 3.14 is a schematic diagram of the X-9 beam line. The beam from the synchrotron is highly polarized. X-ray beams can be blocked from the electron orbit to the beam line through the beam safety shutter. The beryllium window can separate the vacuum from the electron orbit and the beam line. The primary aperture reduces stray scattered x-rays and prevents the beam from striking the mirror. In order to select a narrow energy range, two Si (111) crystals are chosen for our experiment. The crystals are set to parallel using an automatic piezoelectric system. The first (primary) crystal is cooled with water to prevent thermal distortion. The output beam from the second crystal is parallel to the incident beam. The second crystal is on a trolley to keep the beam position in the experiment fixed in space. A focusing mirror performs two functions in the beam line. One is to focus the beam when it is bent slightly. The other one is to reject higher order harmonics through the energy dependence of the total reflection critical angle. At the end of the beam line, a walk-in hutch allows one to set up experimental instruments. The slit size of the hutch aperture, in front of the I_0 detector, is 1.9 mm and 3.5 mm in height for s-polarization and p-polarization respectively. For more information, refer to reference [24].

3.3.6 Sample Alignment

The alignment in this experiment is not trivial because we used a big substrate. The size of the incident photon beam can be adjusted by slits controlled by the

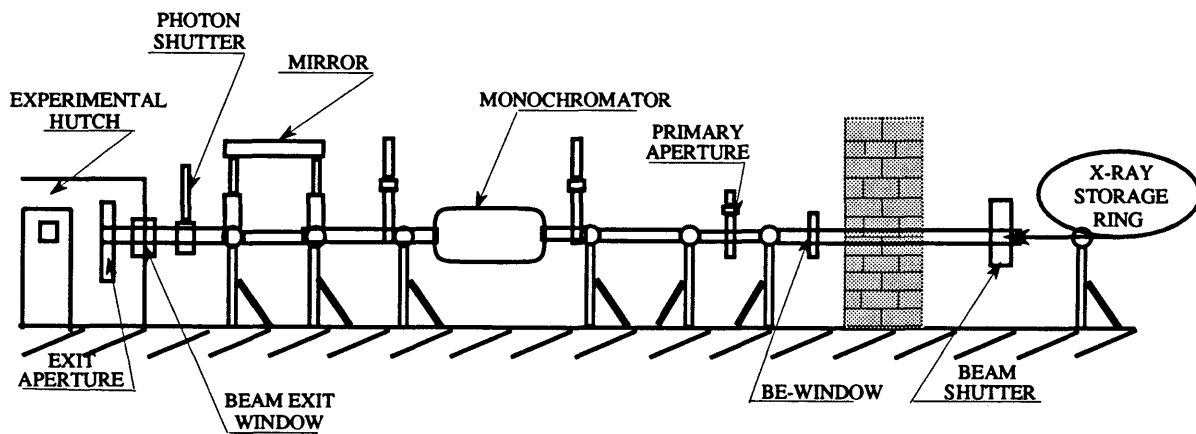


FIG. 3.14: Schematic diagram of X-9 beam line.

computer according to the measurement geometry (s- or p-polarization) we are using. The first important step for the experiment alignment is to find the 'hottest' spot of the beam and set this 'hottest' spot in the middle of the slits. A laser alignment system presented in Fig. 3.15 was used in this experiment to pre-align the substrate. There are two points in the beam line which were pre-determined from x-ray exposure of photographic paper. One is just in front of the I_0 ion chamber. The other one is on the hutch wall (the focusing wall) which is 5 or 6 feet away from the sample. We focus the x-ray beam at some distance from the sample on the focusing wall in order to get a correctly sized beam on the sample. The alignment can be done by setting the laser beam to intersect the x-ray beam pass points (one is in front of the I_0 and the other one is on the focusing wall) using an adjustable mirror. The mirror is adjusted to align the laser beam to the focus point on the wall. After this is done, instruments and the sample (see Fig. 3.12) were placed into the beam path so that the laser beam passes through each. The laser beam should just slightly touch the sample surface. After this pre-alignment was done, the x-ray beam can be opened up. The sample then was moved out completely from the beam (maximum reading from I_1 ion chamber). A Ta slit was moved up and down to find the place that allowed the whole beam to pass through. This prevented the reflected beam from reaching the detector. Using the computer tilt control system, the sample can be moved up and down and tilted back and forth to define a flat position of the sample. The sample stage was then raised up till it obscured half of the beam through the I_1 detector. The sample then is tilted to 8 mrad from the critical angle for the total external reflection. The Ta slit, I_1 and I_2 was raised in order to allow the reflected beam from the substrate to pass through them after the sample was tilted.

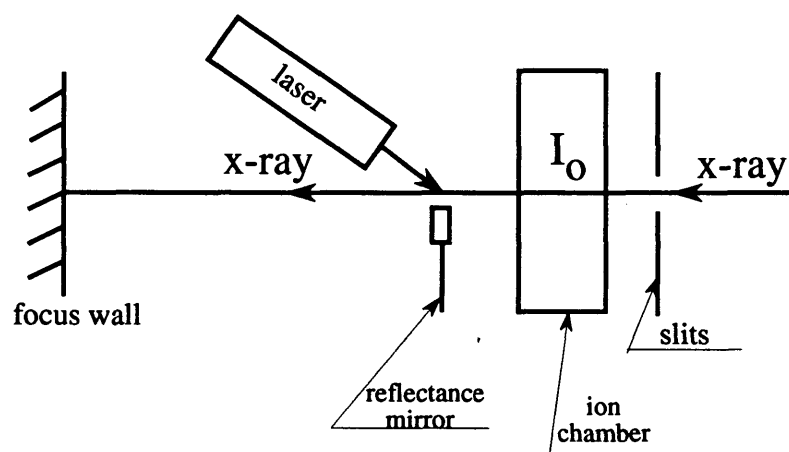


FIG. 3.15: Laser alignment

Chapter 4

RESULTS AND DISCUSSION

4.1 Electrochemical Results

4.1.1 Characterization of the Clean Pt Substrate

A standard method for electrochemically cleaning a polycrystalline Pt electrode surface involves cycling into the oxide formation and reduction potential region. A cyclic voltammogram for our polycrystalline Pt electrode in a sulfuric acid solution is shown in Fig. 4.1. The region from -0.20 V to 0.1 V with respect to a copper wire reference electrode where hydrogen atoms are adsorbed at the Pt electrode is called the hydrogen region. The adsorption of hydrogen on a platinum electrode has been investigated extensively since the early 1960's [62]. Fig. 4.1 shows that there are three current peaks in both the anodic and the cathodic directions at positions of about -0.1 V, -0.03 V, and 0.04 V. Peaks 1, 2 and 3 in the desorption region represent the three crystal faces (110), (111), and (100) respectively. However, peak 2 is not usually seen during the cathodic scan. It is weak but resolvable in our experiment. The positions of the hydrogen adsorption peaks are almost exactly the same as for the hydrogen desorption peaks. This indicates that the reaction of hydrogen atoms with a Pt surface is reversible. The distribution of peaks is strongly influenced [63] by the surface crystallographic orientation, the solution composition, the concentration of the solution, and the rate of scanning. Hydrogen chemisorption on platinum single crystals in 0.5 M sulfuric acid solution was studied by Ross *et al.* [64]. The studies found that the H-Pt bond energy is very sensitive to the crystallographic orientation

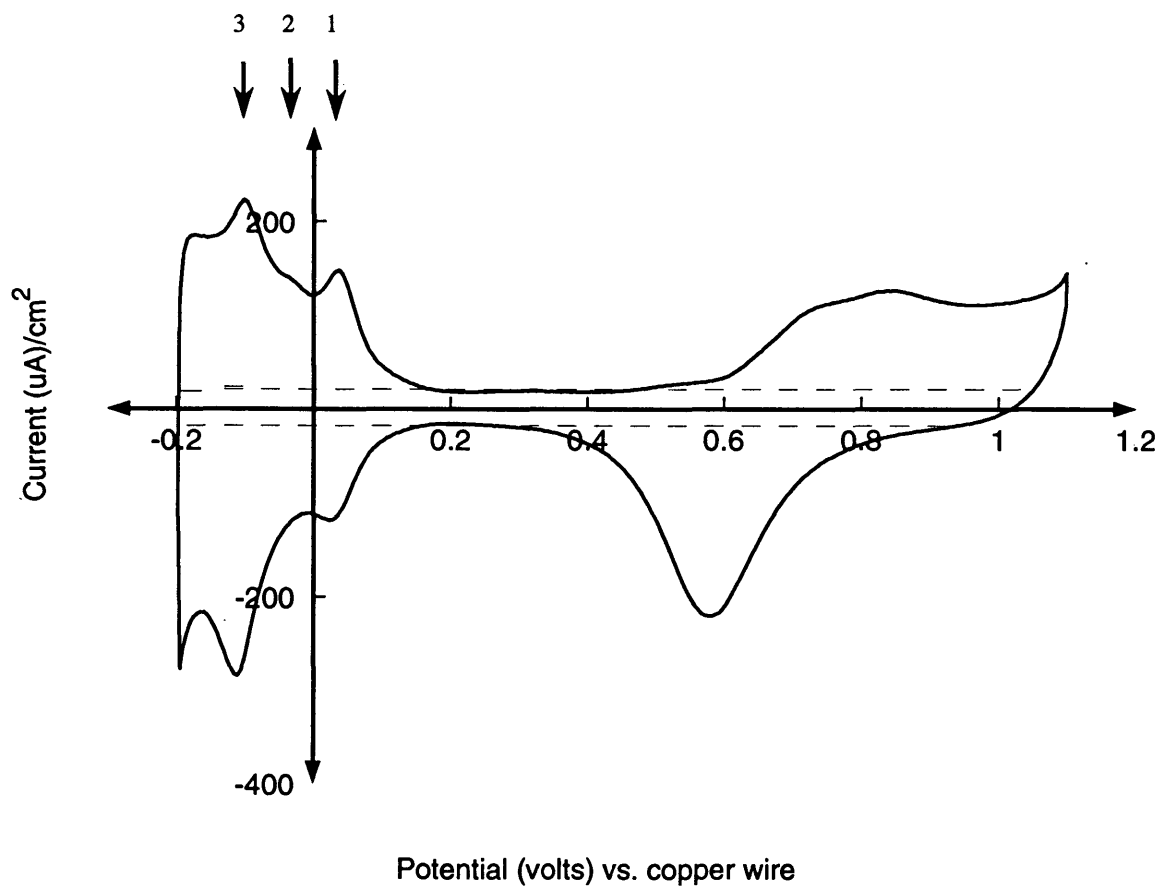


FIG. 4.1: Cyclic voltammogram of Pt electrode in 0.5 M sulfuric acid solution. Scan rate: 20 mV/s.

and the bond strength is increased, in the order of $(100) \geq (110) \geq (111)$.

The region between 0.1 V and 0.6 V is called the double layer region (DLR). In the DLR, the Pt surface is free of adsorbed oxygen and hydrogen. A symmetric curve about the zero current value in the DLR suggests that the solution is almost free of O₂. This is because the solution was purged by zero-grade N₂ for more than four hours prior to being used. More detailed information about the structure of the double layer can be found in Appendix B.

The region above 0.6 V, where oxygen is adsorbed on the Pt surface, is called the oxide region. The interpretation of phenomena observed in this region is still not satisfactory even though many studies have been performed. Oxygen adsorption on a Pt surface is a very complicated process. This is because oxygen atoms and other oxidation products are co-adsorbed on the Pt surface. Their adsorption-desorption potential are mixed together. In this region, the adsorption-desorption process is irreversible. The Pt surface can be reconstructed by this irreversible oxygen adsorption-desorption process at high coverage [65]. In our work, the clean cycling on the Pt surface was continued throughout the full region (from -0.2 V to 1.0 V) until the shape of the I-V curve stabilized. The stability of the I-V curve indicates that the surface roughness is limited.

4.1.2 True Surface Area Determination

One of the problems with the solid electrode is associated with the determination the true surface area which might be different from the apparent surface area (or the geometric area). Unless the surface is atomically smooth, its true surface area usually differs substantially from its geometric area [66].

Table 4.1: The True Surface Area of the Pt Substrate

Substrate	Apparent surface area	True surface area	R
Pt	47 cm ²	57 cm ²	1.21

The ratio of true to geometric area is called the roughness factor, R :

$$R = \frac{\text{true surface area}}{\text{apparent surface area}} \quad (4.1)$$

Polycrystalline Pt electrode surface roughness was studied by *in-situ* STM in sulfuric acid solution [67]. The study found that the roughness of the electrode surface may be caused by the migration of the Pt atoms during the cleaning cycles between the potential region of -0.25V and 1.25V vs. SCE. The same effects were found on low-index single crystal platinum surfaces [68, 69, 70, 71]. Of course, even a freshly evaporated Pt surface will be rough on the atomic scale. We estimate the true surface area of the Pt electrode by integrating the total area under the desorption curve (I-V curve) in the hydrogen region, assuming one hydrogen atom per Pt atom. Table 4.1 lists the true surface area for our Pt sample, which was corrected for the double layer contribution by subtracting the area under the curve in the double layer region (dotted lines in Fig. 4.1). This is a very common way to estimate the true surface area of Pt since no bulk hydrogen absorption occurs in this system.

4.1.3 Cell Contamination Test

It is very hard to work with a such big substrate (apparent surface area of 47 cm²). The first problem we encountered was how to bring the connection from the sample electrode out. Soldering a wire to the sample is not very hard, but we needed something to cover the soldering. Otherwise a constant current will be drawn through the connection with resulting contamination of the surface and/or solution. Quick-set epoxy was used initially, however it did not work for an extended experiment, since epoxy will be desolved by sulfuric acid solution and contaminate the Pt surface. Later we used several layers of nail polish on top the soldering and it solved the problem especially "Wild and Wet" brand nail polish. This is the same material used by those performing *in-situ* STM studies to isolate the sides of their tip.

4.1.4 Anion Effects

The cyclic voltammetry curves of a Pt electrode in different electrolytes are shown in Fig. 4.2. All solutions were purged with zero grade nitrogen and the cycling was continued in each case until a stabilized curve was obtained. The cycling region was changed according to the oxidation-reduction feature. Several results can be immediately extracted from the figure: 1) The double layer contributions are almost independent of the nature of the anions in the electrolytes examined here. The extent of the double layer region (X_{α}), however is strongly influenced by the anions in the supporting electrolyte within the sequence of:



One of the interesting things which can be seen here is that a very small double layer region was observed in the HClO₄ solution; 2) The oxygen formation and reduction

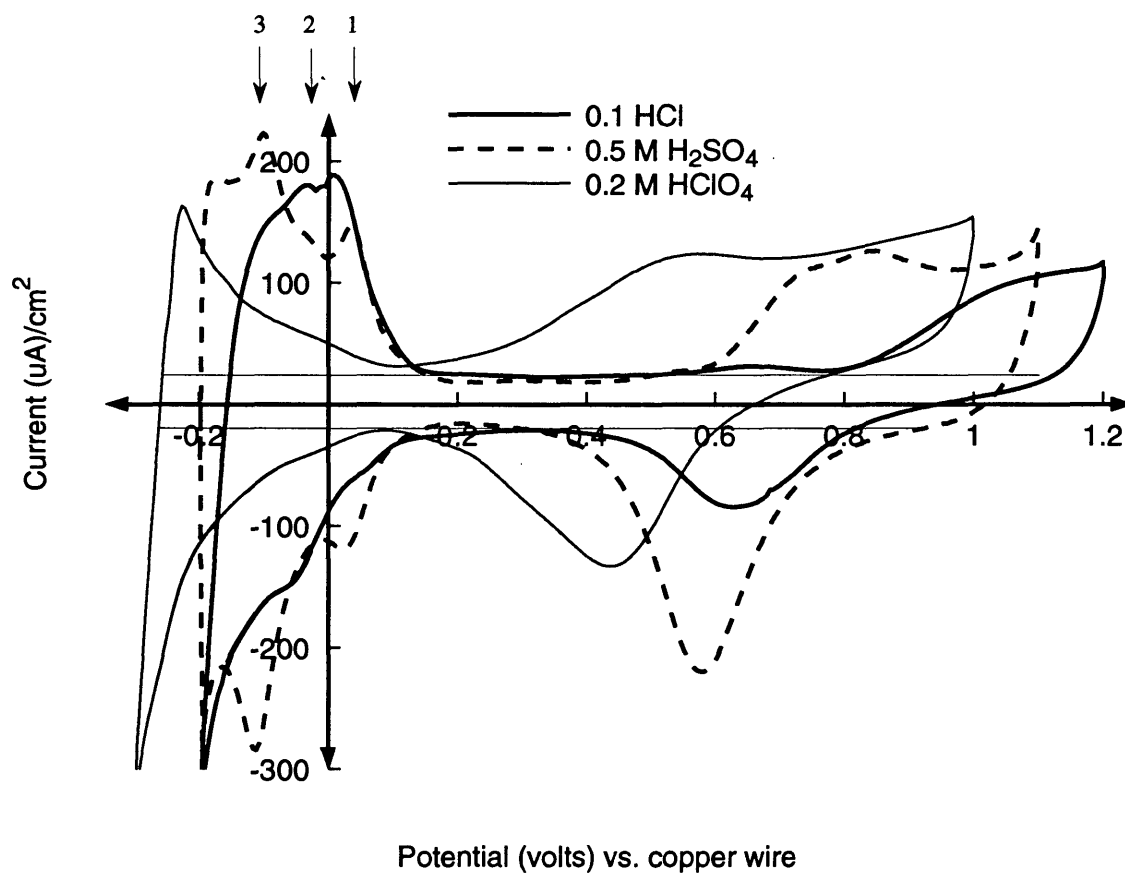


FIG. 4.2: Cyclic voltammogram of Pt electrode in different electrolytes: 0.1 M hydrochloric acid (thick solid line), 0.5 M sulfuric acid (dashed lines) and 0.2 M perchloric acid (thin solid line). Scan rate: 20 mV/s.

peaks are different in different electrolytes; 3) Multiple peaks (1, 2, and 3) of hydrogen evolution are strongly affected by the anions in the electrolyte. The three peaks 1, 2, and 3 are well defined in the sulfuric acid, while these peaks could not be resolved in the perchloric acid solution. These hydrogen desorption peaks are close but resolvable in the hydrochloric acid solution. This is because of the strong specific adsorption of Cl^- ($> \text{HSO}_4^- > \text{ClO}_4^-$) which strongly inhibits the oxidation-reduction process on the Pt surface. The change of the multiple peaks could partly be due to the surface reconstruction of the substrate.

4.1.5 Cu Adlayer Stability Characterization

Reflectance Results The next important step in the experiment was to establish a well defined, and controlled surface. It was important to determine whether or not the surface changed with time. The stability of a copper adlayer on a polycrystalline platinum electrode was studied first by differential optical reflectance spectroscopy which measures the relative reflectance change ($\Delta R/R$) as a function of time. Copper atoms were underpotentially deposited onto a Pt (poly) electrode from dilute Cu ions in solution in the underpotential region to obtain a very thin Cu adlayer (monolayer or submonolayer). Usually, the deposition potential was kept at a particular value (0.05 V vs. copper wire reference electrode) for at least 10 min, then most of the solution was pumped out (deflating the cell window). This leaves a thin layer of electrolyte which is used to control the potential at the working electrode. The x rays can penetrate through this thin layer of electrolyte. Both the EXAFS and $\Delta R/R$ were measured under these conditions. The optical wavelength of the source used in differential optical reflectance measurement ranged from 4800 Å to 8200 Å . The details of the experiment can be found in Appendix C.

Fig. 4.3 shows the relative reflectance change due to the Cu desorption with respect to desorption time (or potential). Optical reflectivity is sensitive to the electromagnetic boundary conditions. These are modified by the presence of the Cu. If the electronic character and/or the coverage of the Cu monolayer changed as a function of time, we would detect the drift in the value of $\Delta R/R$. The $\Delta R/R$ is not very sensitive to Cu^{2+} in the solution because the concentration is very low. Fig. 4.3a shows $\Delta R/R$ due to the Cu desorption with respect to desorption time (or potential) after deposition at potential of 0.0 V for 15 minutes. Here a relatively thick layer of solution was maintained above the sample. One can see that the Cu layer was stripped immediately when the stripping potential was applied. This identifies the magnitude of $\Delta R/R$ associated with a monolayer. The noise is due to the thick water layer between the substrate surface and the Kapton window.

Also, Fig. 4.3b (where the deposition potential was held at 0.0 V for 15 minutes before desorbing the Cu layer) and 4.3c (where the deposition potential was held at 0.0 V for 2 hours before desorbing the Cu layer) are quite similar. In these experiments, extra solution was sucked out using an active syringe system and only a very thin layer of water (13 μm , see section 4.2.1) left in the cell. This result reveals that the Cu adlayer did not change for a long period of time at the applied potential, under the thin layer water conditions that apply to the EXAFS experiment. The noise is much lower than the experiment shown in Fig. 4.3a.

Another feature can be seen in Fig. 4.3b and c is that the desorption of the Cu layer takes a longer time with the Kapton cell window against the substrate. This phenomenon may be due to the compressed thin electrolyte layer and its electrical characteristics.

The CuPt alloy is not seen in the reflectance experiment. This is because the

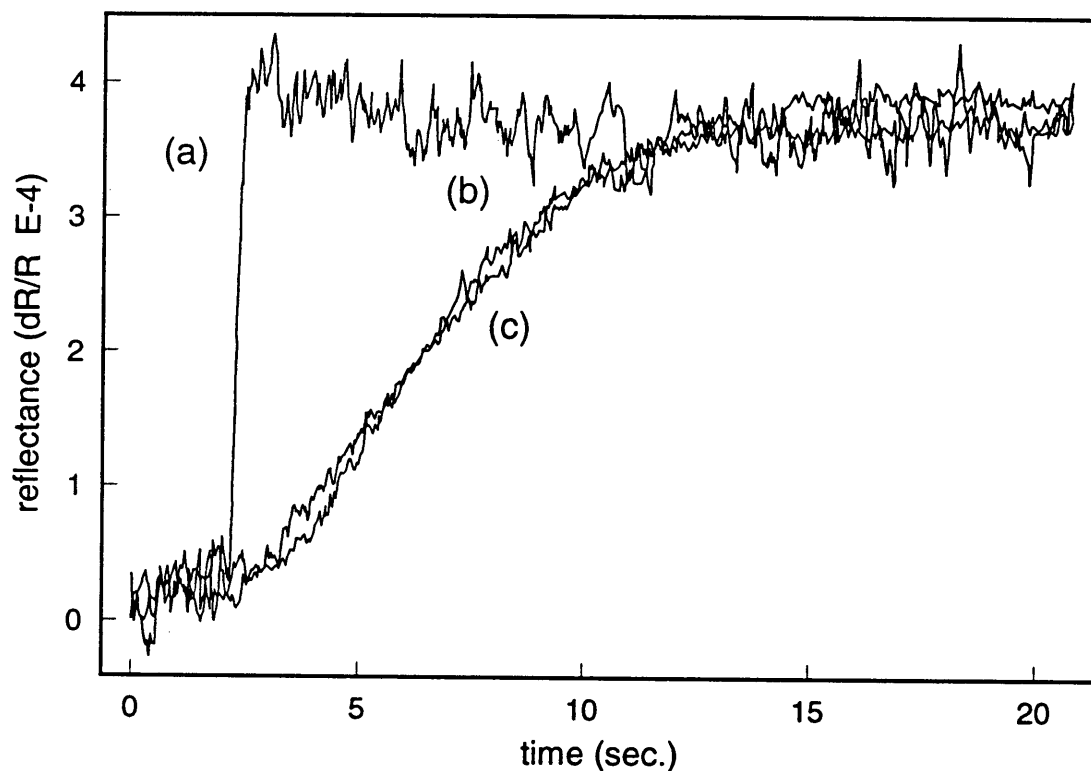


FIG. 4.3: Normalized reflectance change $\Delta R/R$ as a function of desorbing time t (seconds). scan rate: 20 mV/s. (a): Prior to stripping of the Cu monolayer, the potential was held at 0.0 V for 15 minutes with excess solution in the cell; (b): Prior to stripping of the Cu monolayer, the potential was held at 0.0 V for 15 minutes with the Kapton window deflated; (c): Prior to stripping of the Cu monolayer, the potential was held at 0.0 V for 2 hours with Kapton window deflated.

relative changes of the reflectance are the same for three different desorption cases. If Cu Pt alloy is formed during the deposition (longer wait at deposition potential), $\Delta R/R$ would be different because of the electronic character of the alloy.

Voltammetry Results The anion effect of the oxidation-reduction cycling was discussed in section 4.1.4. Since the double layer region is very narrow in perchloric acid solution, the copper adlayer could interact with oxygen atom strongly in the deposition region. Therefore, we did not measure the EXAFS of the copper adlayer in perchloric acid solution.

The electrochemical test of the Cu layer deposition is shown in Fig. 4.4 in a solution of 0.5 M H_2SO_4 containing 2×10^{-4} M Cu^{2+} ions. The full line curve shows the Cu adlayer on a polycrystalline Pt electrode due to UPD without waiting at 0.0 V with respect to the Cu wire. There are basically three peaks (not well defined but resolvable) in the deposition step at positions of about 0.38, 0.24 and 0.10 V with respect to a copper wire reference electrode. A big valley at about 0.05 V significantly suggests that the Cu monolayer finishes at that potential. In our experiment, we used this potential to obtain the full Cu monolayer. If the deposition potential is less than 0.05 V in our case, bulk copper may be deposited on the Pt surface. One can see that the three desorption peaks are shifted from their respective values on the adsorption branch with the peak separation of about 60 mV. This indicates that the Cu UPD process on Pt surface is nearly reversible [2]. The distribution of the desorption peaks is dependent on the stripping rate.

Dashed lines shown in Fig. 4.4 are the stripping curves obtained under the following conditions with the deposition potential of 0.05 V. 1) the stripping curve is obtained after the copper layer was deposited at 0.05 V for 15 minutes; 2) the stripping curve obtained after the copper layer was deposited at 0.05 V for 1 hour;

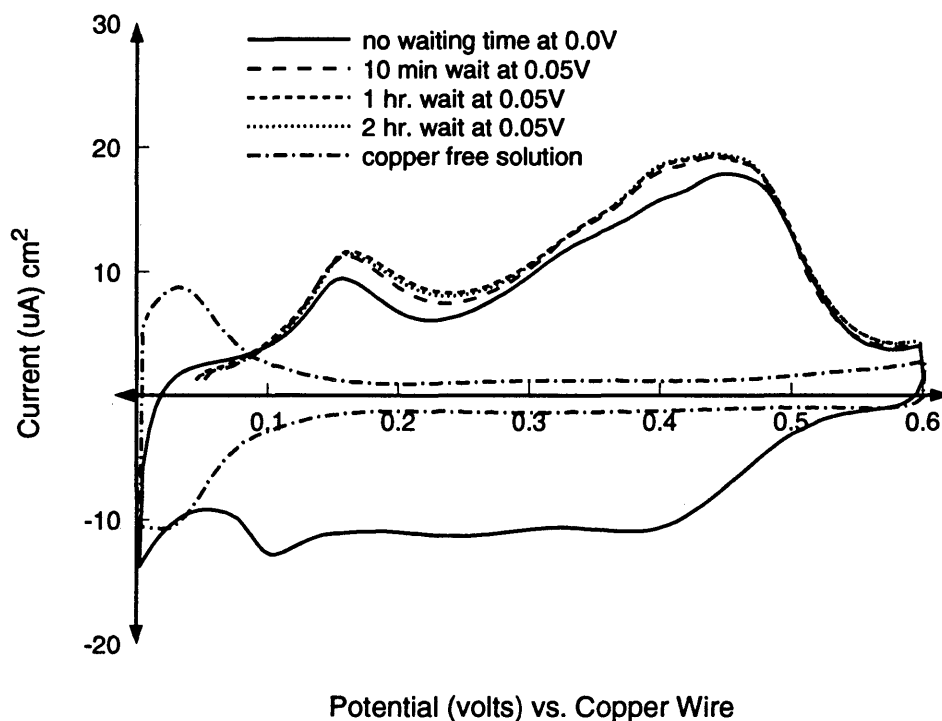


FIG. 4.4: Voltammetry of Cu adlayer on polycrystalline Pt electrode in sulfuric acid solution. Solid curve is the continuous cycling of copper deposition-desorption; Dashed lines are stripping curves of copper monolayer deposition with different waiting time at potential of 0.05 V vs. copper wire reference electrode; Semi-dashed line is the voltammetry of the double layer in Cu^{2+} free solution. Scan rate: 20 mV/s.

3) the stripping curve obtained after the copper layer was deposited at 0.05 V for 2 hours. The cell window was deflated 15 minutes later after initial Cu deposition. The solution was again pumped in while the copper monolayer was stripped off. We can see immediately that the copper coverage was almost the same for the three waiting times while the cell window was deflated. This suggests that the Cu monolayer layer was stabilized for a long period time, confirming the $\Delta R/R$ study. The copper coverage was determined from the electrochemical stripping measurement. The actual Cu coverage of about $505 \mu\text{coul}/\text{cm}^2$ is slightly larger than the coverage expected for a close-packed monolayer ($480 \mu\text{coul}/\text{cm}^2$) of polycrystalline Pt surface. This makes the UPD Cu coverage 1.05 monolayer. This result is similar to what Kolb *et al.* obtained in their study [19].

The semi-dashed line in Fig 4.4 shows the voltammetry of the double layer without Cu^{2+} ions in solution. It is easy to see hydrogen evolution beginning at about 0.1 V with respect to the copper wire reference electrode. This is inhibited when Cu^{2+} ions are present in the solution. This is the result used to determine the double layer reorganization charge flow as a background in the copper desorption experiments.

QCM Results Our recent quartz crystal microbalance (QCM) experiment suggests [72] one monolayer of Cu on Pt is obtained from the QCM mass measurement which is in a great agreement with our cyclic voltammetry experiment. Recent coupled UHV-electrochemical experiments have suggested that the Cu is found in a state of partial discharge when the copper layer is less than one monolayer, induced by coadsorbed anions [73]. Evidence for the partially charged form of Cu adlayer also studied by McBreen *et al.* from the x-ray absorption near edge structure spectroscopy [42]. This would lead to incorrect coverage estimates based upon charge measurement alone. It also implies that anions, mostly bisulfate ions HSO_4^- in our

case, must be strongly coadsorbed with the Cu. This is consistent with the evidence that metal monolayers are influenced by strongly coadsorbed anions [34, 35]. The coadsorption causes a shift, toward more negative potential, of the metal stripping peak in the I-V voltammogram.

The results from reflectance spectroscopy, the cyclic voltammetry and the QCM indicate that 1) a good clean Pt substrate is obtained; 2) the Cu adlayer is one monolayer and the monolayer is stable for at least several hours; 3) no non-Faradaic contribution is obtained from our experiments and the results are different from the *in-situ* STM study by Sashikata *et al.* [36]. The difference may be due to the different copper coverage in our and their experiment. In their study, the copper coverage is less than one monolayer. Their result is in agreement with the study by Goodman *et al.* [73].

4.2 SEXAFS results

4.2.1 Estimation of Water Thickness and Surface Roughness from Angle Scan

As mentioned in the experimental section, the EXAFS data were taken while the sample was under the electrochemical control. A thin layer of water between the sample surface and the Kapton cell window is necessary for electrochemical control. However, the thickness of this thin layer of water will affect (1) the background level by changing the magnitude of Compton scattering and also (2) the signal magnitude by increasing the attenuation of the x-rays. The surface roughness is the factor that will affect the x-ray incident angle. Therefore we need to obtain both the thickness (δ) of the thin water layer and the roughness (γ) in order to correct the background and set up the x-ray incident angle. δ and γ can be estimated by non-linear least squares fit to the angle dependent reflectivity (see Fig. 4.5) [74]. The number is found to be about 13 μm and 14.8 \AA for the water thickness and the surface roughness respectively.

4.2.2 Incident Angle and Energy Dependent

It is important to keep the x-ray incident angle constant during this experiment. This is because a change of the incident angle changes the x-rays' penetration depth and the x-ray intensity at the surface. The change might be confused with a change of the real experimental results. In this experiment, we kept the incident angle at 8 mrad which is smaller than the critical angle (9.43 mrad calculated from $\alpha_c = \sqrt{2\delta}$ and Eq. (3.19)) for the total external reflection of the system (see section 3.2.3).

In this experiment, the incident angle was controlled by a computer through two motors that allowed the sample to move up and down and to tilt. Detailed information can be found in section 3.3.6. Fig. 4.5 presents the angle dependence

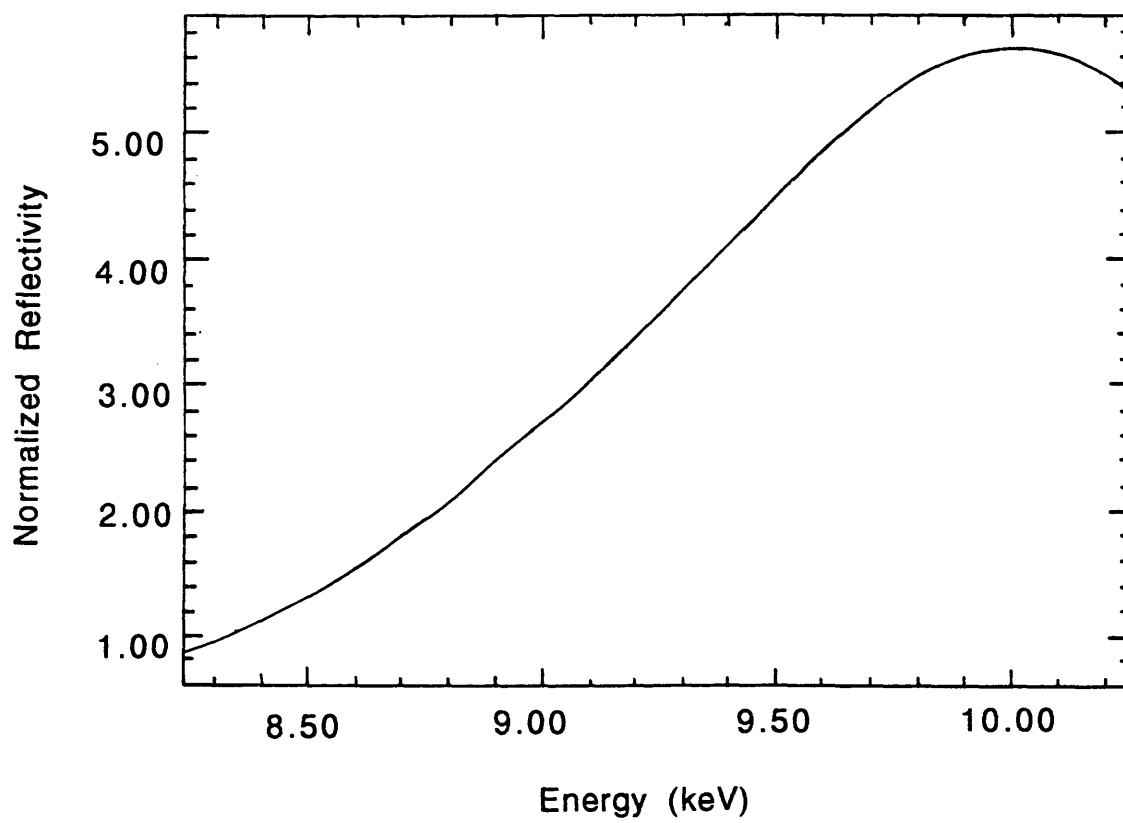


FIG. 4.5: Angle dependent reflectivity

reflectivity. The peak of the reflectivity should occur at approximately 10 keV if the incident angle is 8 mrad [74]. The relationship of the incident angle and the x-ray reflectivity to the incident energy was calculated by Dr. L. Lurio at RPI.

4.2.3 Standards

Near Edge Spectra of Standards The near edge spectra of Cu^{2+} , Cu_2O , CuO , CuS and Cu foil are shown in Fig. 4.6. All the edge spectra were recorded with higher resolution than the pre-edge and post-edge spectra from -50 to 50 eV around the Cu-K edge (8979 eV) with a step size of 1 eV. Each scan lasted approximately 5 minutes. The reason for taking Cu^{2+} ions EXAFS is that a 10" long pure Cu wire was used as a reference electrode in the early part of this project. Cu wire was continuously dissolved into solution and therefore the Cu^{2+} ions concentration changes with time. We are aware that the change of the step height of the absorption edge is associated with the change of the Cu ions concentration in the thin solution layer. The characteristic of Cu^{2+} ions EXAFS is the big peak superimposed on the white line which is shown in Fig. 4.6.

Threshold or edge (the abrupt increase in absorption coefficient) positions for standards are listed in Table 4.2. It is easy to see that the threshold position of Cu^{2+} ions is higher than that of the Cu metal edge. They are about 7.5 eV apart. The edge position of Cu_2O is close to the edge position of Cu metal. Both Cu metal and Cu_2O have shoulder edge shapes.

The edge position of CuO is close to the threshold position of Cu^{2+} ion in solution. The shoulder of the edge of the CuO is slightly higher than the Cu_2O . The shape at the edge in CuS is different than the others. A strong white line in the Cu^{2+} ion scan is caused by the multiple photoelectron scatterings between Cu and O atoms. The

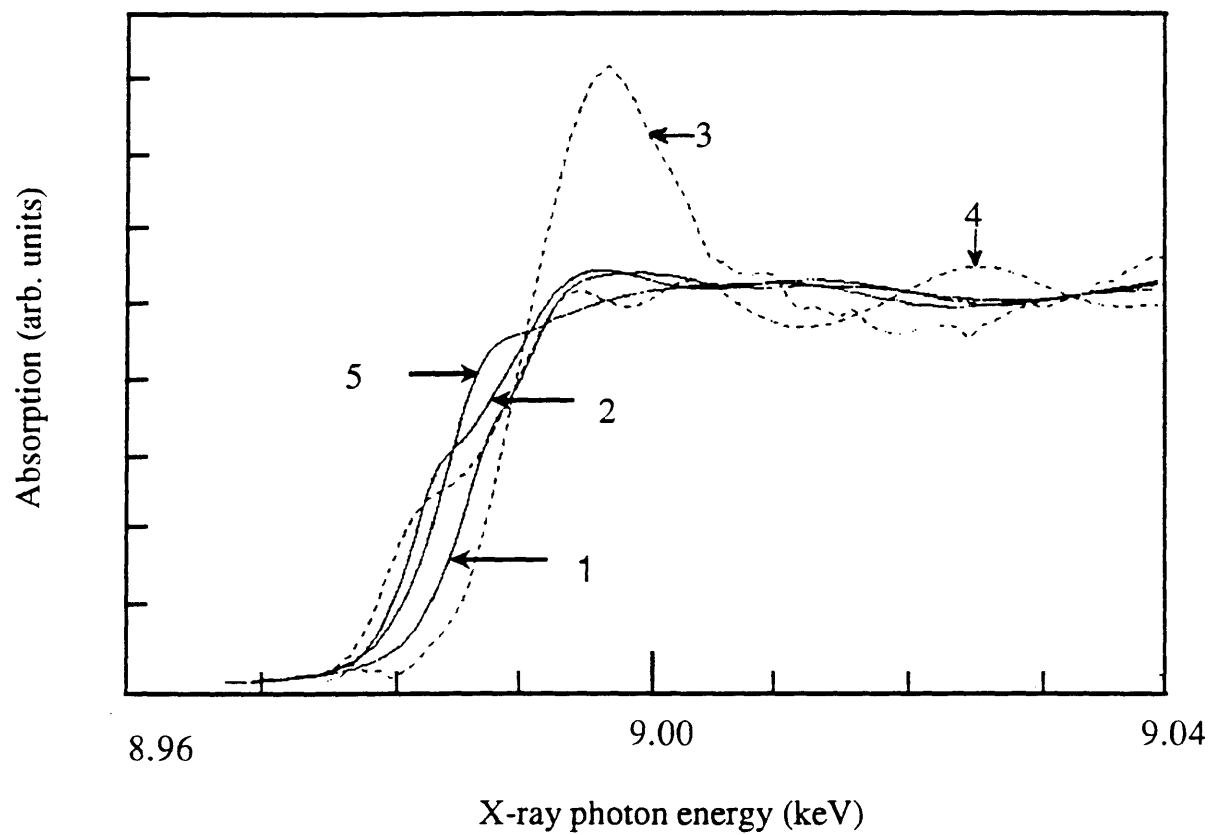


FIG. 4.6: Near edge spectrum of the standards.
1) is from CuO; 2) is from Cu₂O; 3) is from Cu²⁺ ions in solution; 4) is from Cu metal and 5) is from CuS.

Table 4.2: Threshold Position of Standards

Type	Threshold Position (eV)
Cu ²⁺	7.5
Cu foil	0
CuO	6
Cu ₂ O	2
CuS	1.5

edge height is an indication of the amount of Cu. Based on these observations, the near-edge spectrum could tell us the chemical state of the Cu and the amount of the Cu.

The edge spectra and edge positions of standards are similar to a report from McBreen [42]. The results showed that the edge position of Cu⁺ with a pre-peak is located at about 1 eV higher than that of Cu⁰.

Nickel Filter EXAFS We used a nickel filter placed in front of the Söller slit to preferentially adsorb the x-rays that were scattered from the sample as opposed to the lower energy $K\alpha$ x-rays. However, this also leads to a superimposed nickel EXAFS on top of the Cu monolayer EXAFS. The nickel EXAFS contamination can be reduced by using a double-layer nickel filter with total thickness of 25 μm . Of course, doubling the nickel filter will reduce the Cu EXAFS signal as well. But it only slightly attenuates the copper EXAFS signal. Further reduction can be done by subtracting a nickel foil EXAFS from the copper EXAFS during the data analysis. The nickel EXAFS measurement was done using a transmission detection mode. The $k\chi$ function of the nickel EXAFS is presented in Fig. 4.7. The Ni EXAFS is recorded

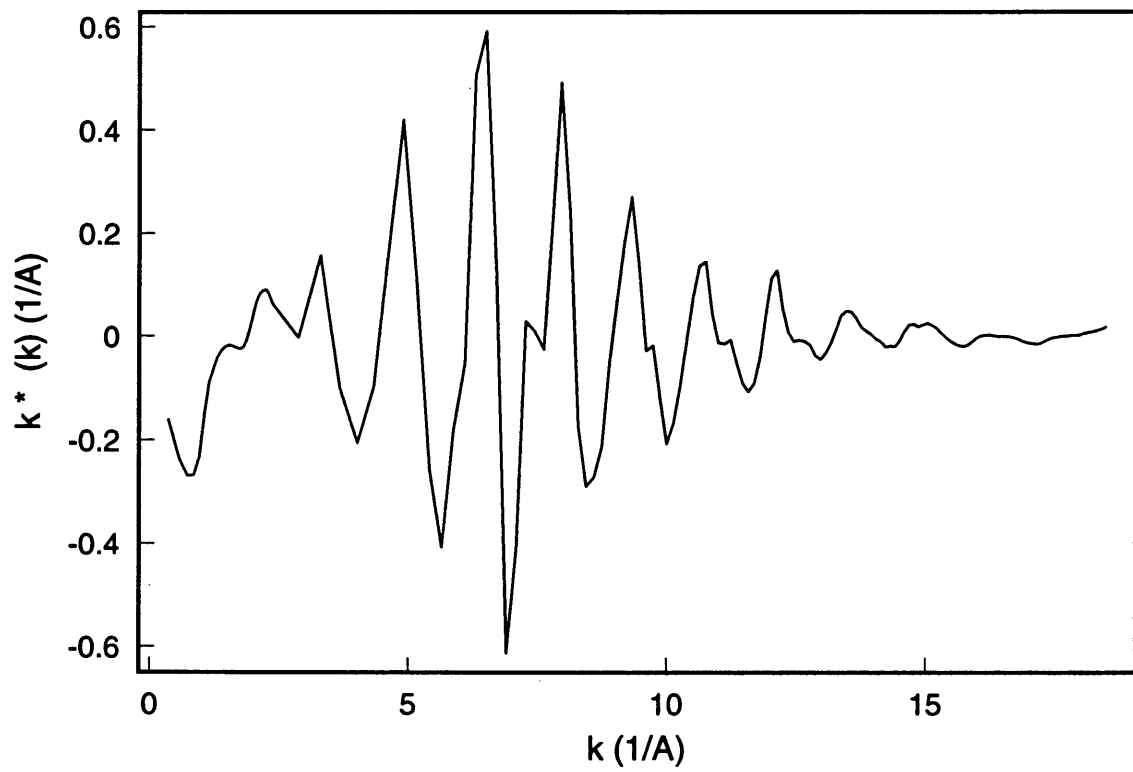


FIG. 4.7: EXAFS function of nickel filter

through the copper EXAFS region, using the k -scan setup of copper. The $k\chi$ function shows a broad peak at low k values and four peaks at high k values between 5 to 10. This is the characteristic of the nickel foil.

The double-layer nickel filter is only used in the s-polarization geometry. This is because small size of x-ray beam was used in p-polarization and less Compton scattering was produced in this geometry and less Ni fluorescence was produced in this geometry as well. Therefore one layer of nickel ($12.5 \mu\text{m}$) was used in the p-polarization.

4.2.4 High Signal to Noise Ratio

One of the problems of a surface EXAFS experiment is the low ratio of the signal to noise. With the advantage of our large sample substrate, however, the signal-to-noise ratio was four from a single scan. This is very high compared to other surface EXAFS experiments. The data in Fig. 4.8 was produced with only one scan with the polarization of the incident x-ray beam perpendicular to the normal of the Pt surface (s-pol.). Despite the good signal to noise ratio, about 10 to 20 good scans were averaged to get better resolution in this work.

The better signal to noise ratio was accomplished with some compromises. Our big sample substrate is polycrystalline, rather than single crystal, Pt. It is true that the substrate orientation may have an effect on the metal adlayer. However the near neighbor spacing should still be equivalent. An advantage of the polycrystalline substrate is that Bragg diffraction resonances are entirely averaged out. If this exists in the SEXAFS raw data then the analysis would be much more difficult.

In our early experiments, we had difficulties in controlling the leaking of the cell and thus the water thickness over a long time scale. Therefore, we had variations

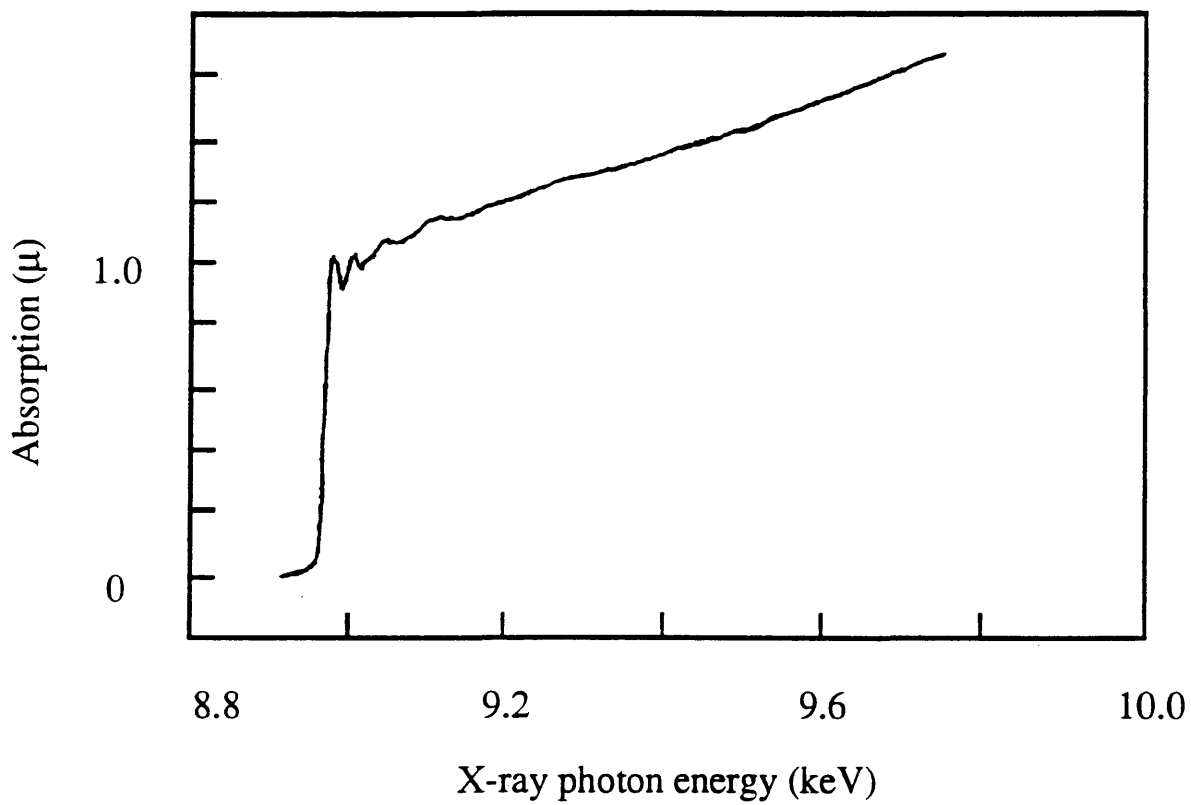


FIG. 4.8: The adsorption coefficient from a single scan due to a Cu adlayer on Pt for s polarization as a function of the incident x-ray energy.

in the height, shape and energy position of the edge. The height of the edge is proportional to the amount of Cu while the shape and position are related to the chemical state of the Cu as is the case in the comparison between Cu^0 and Cu^+ . These features also display some dependence on the angle of incidence. With our improved sample control, these variations with time have been significantly reduced, particularly in the data measured in November 1992 and 1993.

4.2.5 Step High Change with Changing of Water Layer Thickness

The step height increased with increasing in the concentration of the Cu^{2+} ions. However, the step high decreased with thicker water layer thickness (because x-rays are attenuated by the water). Both problems affect the data analysis significantly. We only observed the step height increase in our early experiments because of the Cu^{2+} ions. In our early experiments, we also had difficulty controlling the Cu^{2+} ion concentration due to continuous dissolution of the copper reference electrode. The change of the step height is more sensitive to the Cu^{2+} ions change than to the water thickness change. In our recent experiments, we coated most of the reference electrode with nail polish. As a result, the change of Cu^{2+} ions in solution was kept constant for a long period time. The step height decreased during successive scans. Fig. 4.9 shows the step height change with (Fig. 4.9a) and without (Fig. 4.9b) the water layer correction. The water layer correction is made simply from the water adsorption of x-ray beam [74].

4.2.6 Near Edge Spectrum

Cu adlayer We are the first group to acquire SEXAFS data from two polarizations (s and p) on a single electrochemically controlled layer, where s-polarization

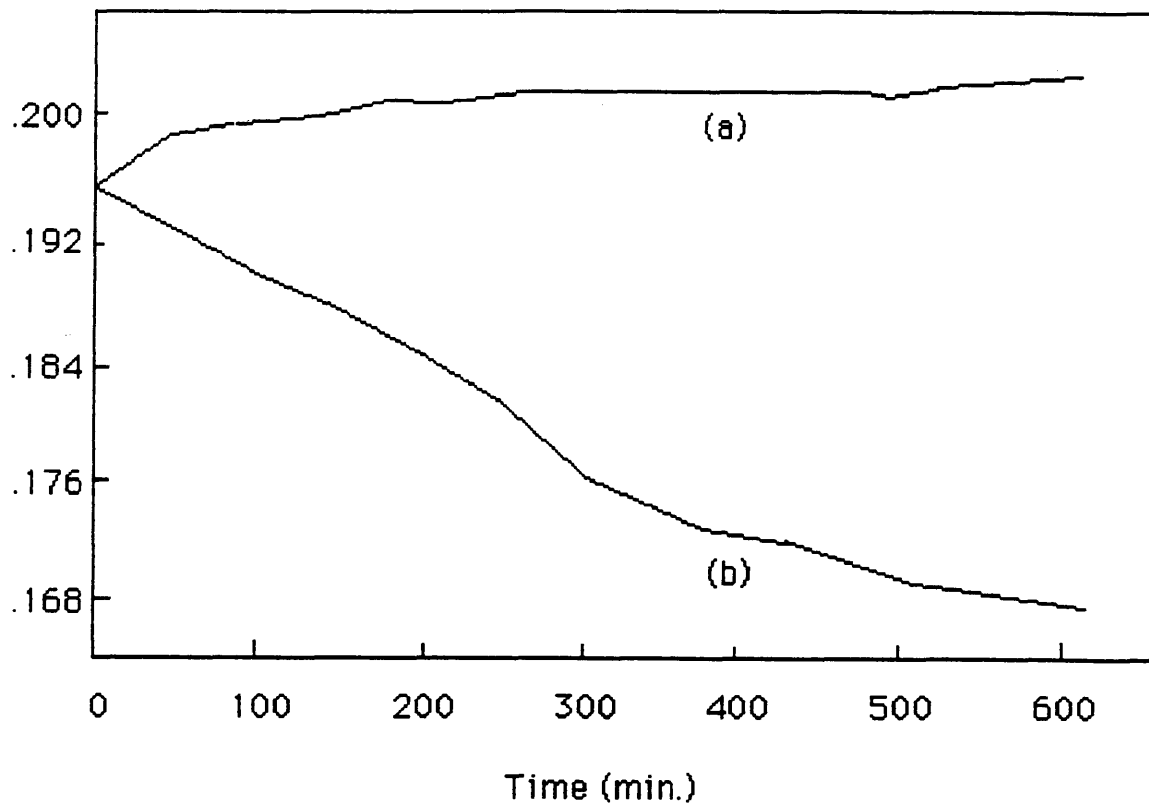


FIG. 4.9: Step height change with the change of water layer thickness
a) Step high change vs. the acquisition time for s-polarization data after the water layer correction. b) Step height change vs. the acquisition time for s-polarization data before the water layer correction.

(the electric field of the x-rays is parallel to the interface observed, see Fig. 3.6a) primarily gives information about the adsorbed monolayer in the plane of the surface and p-polarization (the electric field of the x-rays is perpendicular to the interface observed, see Fig. 3.6b) primarily gives information preferentially about the substrate and the electrolyte in the region of the interface. Therefore, using Eqs (3.26) and (3.27), a unique number of neighbors of each type can be determined. In this work, the SEXAFS data were recorded from -700 eV to 800 eV around the Cu-K edge. Each scan lasted about 30 minutes and we acquired about 20 good scans for each configuration.

The near-edge region of summed spectra corresponding to the two different polarizations are presented in Fig. 4.10. The solid line (20 summed scans), and dashed line (14 summed scans) represent s- and p-polarization, respectively. As depicted by the figure, the two polarizations show different edge shapes and positions. In s-polarization, the edge appears at approximately the same energy as the edge in metallic Cu. In p-polarization, the edge is shifted by approximately 1 eV toward higher energy. A very small, but resolvable, shoulder is present in the s-polarization case, which is also a characteristic of the metallic Cu K-edge. The absence of a shoulder in p-polarization is mainly due to lower resolution. In this project, the slit size of hutch aperture is 1.9 mm and 3.5 mm in height for s-polarization and p-polarization respectively. The 'white line' at the edge for p-polarization is larger than in the edge for s-polarization and the first oscillation is evidently smaller for p-polarization. This demonstrates that we have a well-defined surface plane. If an appreciable amount of the Pt or the Cu existed in three dimensional clusters, then we would not see any significant difference between the two orientations. The fact that the s- and p-polarizations are significantly different in the near edge region gives us additional

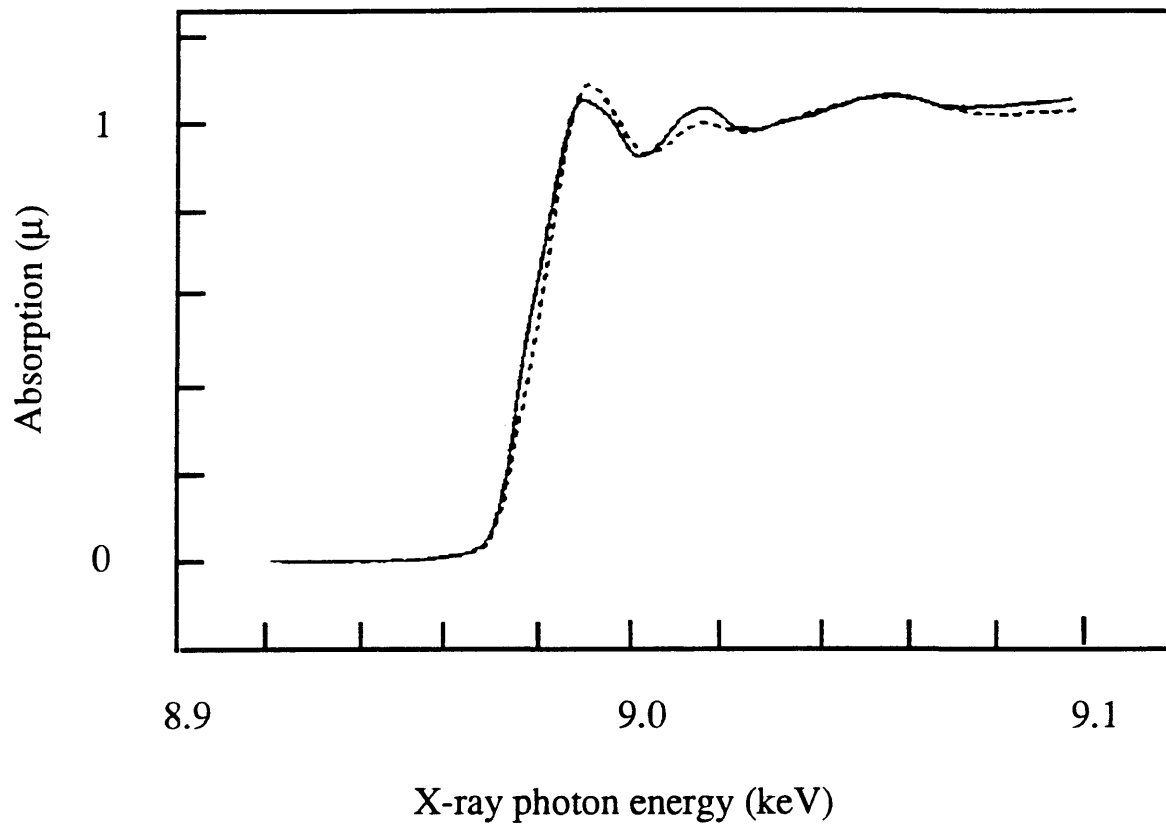


FIG. 4.10: The near-edge region of the fluorescence spectra in s- (solid line) and p- (dashed line) polarization

Table 4.3: Normalized Edge Position of Cu Foil, and Cu Adlayer of Both s- and p-Polarization

Type	Cu foil	Cu adlayer(s-)	Cu adlayer(p-)
Edge Position	4.16 eV	-1 eV	-1.4 eV

evidence that we have a reasonably flat sample. The edge positions of Cu metal, and the Cu layer from two different polarizations are listed in Table 4.3. The edge energies are measured with respect to 8979 eV. All values are ± 0.5 eV.

By comparing the edge positions of the Cu adlayer and the Cu metal, it is clear that the adsorbed layer is different from Cu metal. This is certainly expected because of the strong underpotential adsorption bond. The Fermi energy of the Cu will align with that of the Pt. The high electron density which provides static screening for the Pt surface will be intimately connected with the Cu adlayer. It is not clear at this time whether or not the Cu adlayer is partially charged from our near edge data. This is because the white line is superimposed on the near edge spectra and changes the position and the shape of the edge. So far, no good theory can separate the effects of the white line and the near edge feature. Therefore it is very hard to get information only from the edge spectra. The edge position of the Cu adlayer, in our case, is close to that of neutral Cu. This would be consistent with an XPS study of electrochemically deposited Cu on Pt [75]. The XPS studies showed that the structure of the Cu monolayer is metallic except the binding energy was found about 1 eV below the metallic Cu. However, it is inconsistent with the recent XANES study by McBreen [42] in which Cu was found to have an edge position similar to that of Cu^+ . Therefore they concluded that the monolayer Cu has an oxidation state of 1. The discrepancy of the results from two groups are probably due to the pretreatment

of the Pt substrate.

4.2.7 Post Edge Spectrum

In order to check the Cu monolayer stability, we first measured EXAFS in s-polarization (S1) geometry. After taking about 13 good scans in the S1 geometry, the sample was rotated to p-polarization (p) geometry without changing the electrochemical control. We rotated the sample back to s-polarization (S2, 10 more scans) after about 29 good scans were taken from p geometry. Fig. 4.11 shows the $k\chi(k)$ function from S1(a) and S2(b). They look nearly identical, even though they are about 2 days apart. This is another evidence that there was no evolution of the monolayer.

The SEXAFS function $k\chi(k)$ obtained for the Cu adlayer is shown in Fig. 4.12a and 4.12b for s-polarization and p-polarization, respectively. The big spike in both polarizations at approximately $1.7 \text{ (\AA}^{-1})$ is the contribution from multiple-electron scattering [55]. This region was ignored during the data analysis by using a window function consisting of a unit amplitude step between $3.625 \text{ (\AA}^{-1})$ and $12.955 \text{ (\AA}^{-1})$. However, long range oscillations exist in the FT of this function, which will interfere with the real structure. Therefore, the window function was broadened with a Gaussian of half-width $0.5 \text{ (\AA}^{-1})$ to suppress this oscillation. This window function accounts for the finite extent of the data in k space.

Other evidence of the differences in amplitude and frequency between s and p polarization can also be seen from the $k\chi(k)$ function. We did not concentrate on the $k\chi(k)$ function during the data analysis, because there is a large overlap of the influence of the neighbors in our case.

The Fourier transform $\phi(r)$ of the SEXAFS function $k\chi(k)$, the fit of the spectrum and the residual between the fit and the experimental data are presented in Fig.

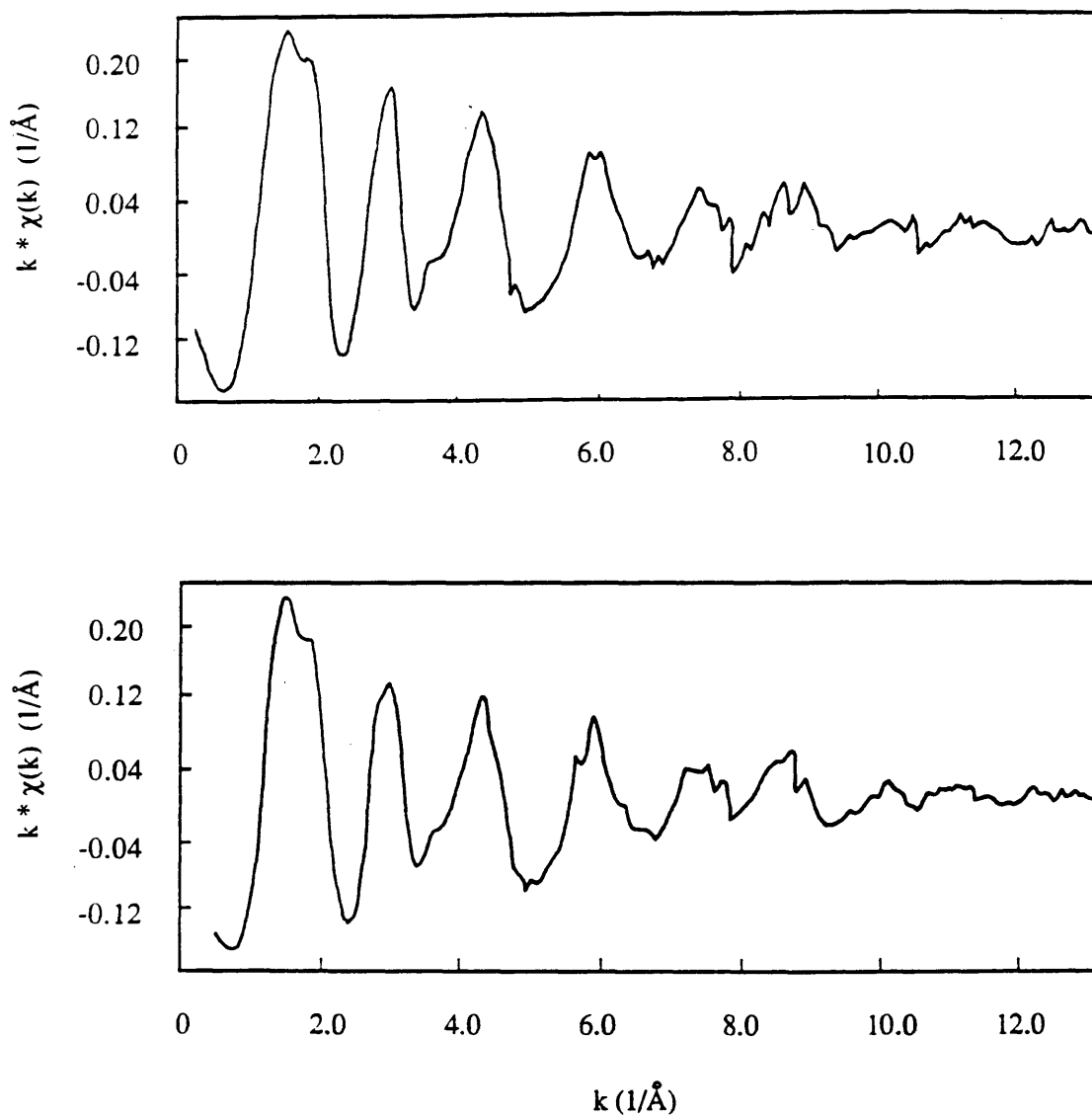


FIG. 4.11: The SEXAFS function $k\chi(k)$ from s-polarization as a function of the photoelectron wave number k . (a) S1 and (b) S2 are 2 days apart.

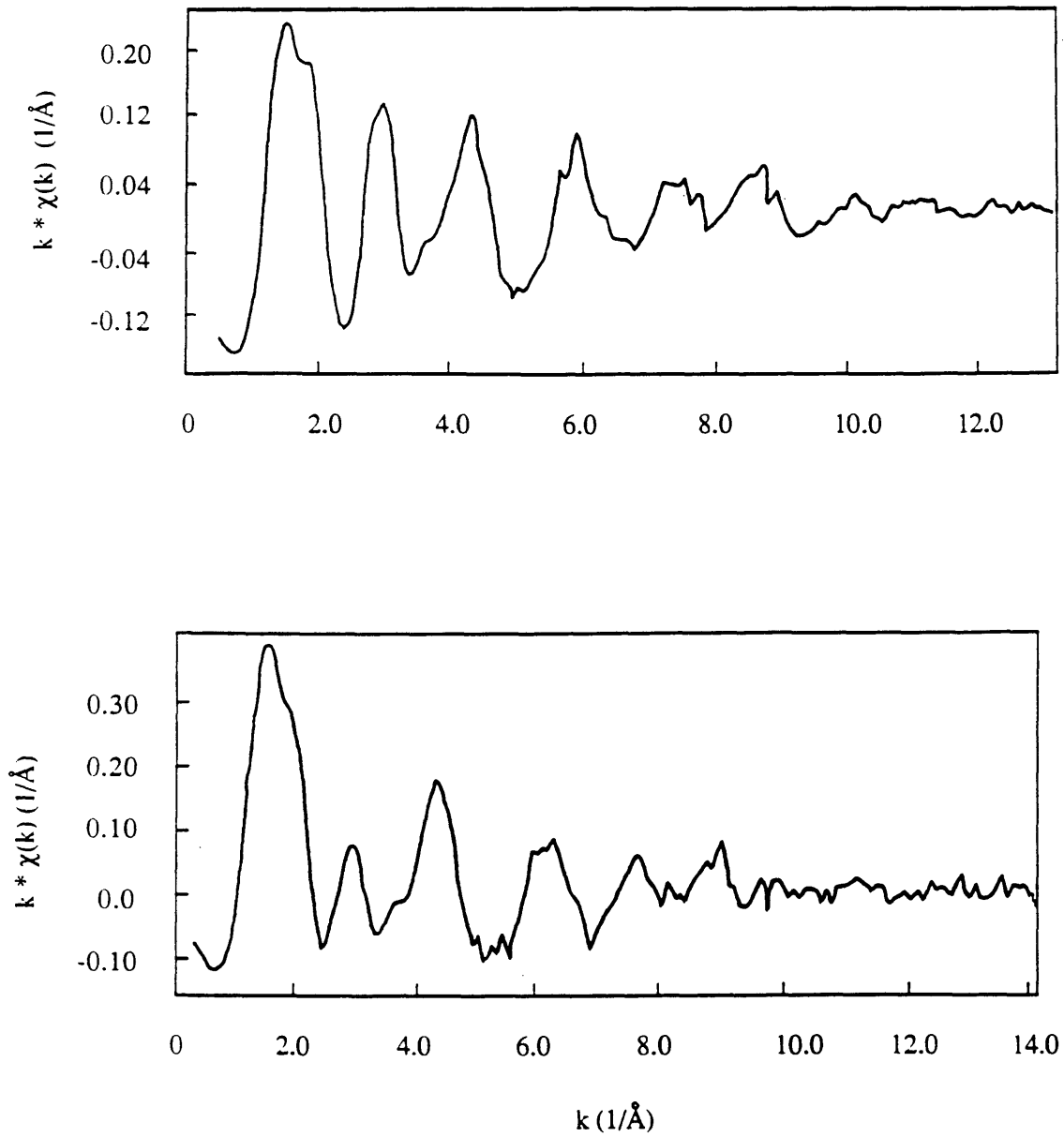


FIG. 4.12: The SEXAFS function $k\chi(k)$ from both s- and p-polarization. (a) s- and (b) p- polarization as a function of the photoelectron wave number k .

4.13 and Fig. 4.14 for s-polarization and p-polarization, respectively. The top part of the figure is the experimental data and the middle part of the figure is the fitted data with signatures used for this fitting. The bottom part of the figure is the residual of the experimental data and signatures. The envelope in the figure corresponds to the amplitude value of $\phi(r)$, which includes both real and imaginary parts of $\phi(r)$. The oscillations inside of the envelope are the real part of the $\phi(r)$. Ideally, the peaks in $p_{\alpha\beta}(r)$ should be separated after the Fourier transform of the $k\chi(k)$ function. However, in our case, each 'feature' in the real part of the unknown spectrum includes contributions from several neighbors at different distances. Also, each kind of atom has more than one substantial peak. We must include all overlapping contributions in order to arrive at a meaningful fit to any portion of $\phi(r)$.

Because the backscattering phase shift contains some k dependence, the 'features' in $\phi(r)$ appear at values of r which are not the same as the associated interatomic distance. This can be calibrated, however, by measurements on standard compounds.

In our earlier data analysis, the peak in $\phi(r)$ at about 1 Å which is so prominent in the s-polarization spectra was often thought to be low frequency noise or a real neighbor. Recently, we found that this 'feature' is due to the Ni EXAFS from the Ni filter placed in front of the fluorescence detector. The broadening due to the width of the Compton scattering peak reduces the Ni EXAFS nearly to zero below the Cu K-edge, which misled us into believing that it would not affect the data significantly. We also found out that the Ni signature extends significantly into the region we have been fitting with other (O, Cu) peaks. After subtracting the Ni EXAFS from our data, we can bring both s and p data into greater agreement. Such as the distance of Cu-Pt from both s- and p-polarization are the same.

As mentioned previously, each peak in $\phi(r)$ may contain contributions from sev-

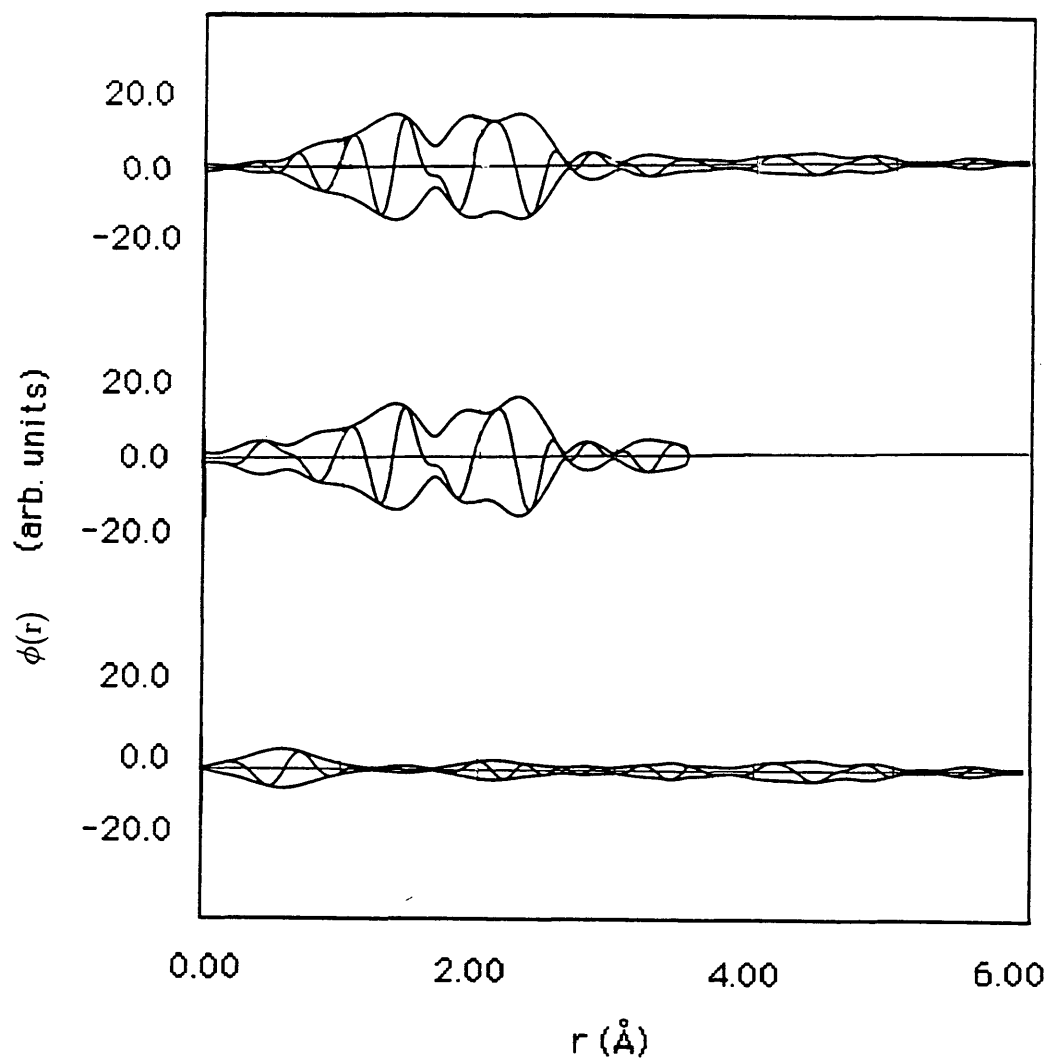


FIG. 4.13: The Fourier transform of the $k\chi(k)$ for s polarization, the fitted data and the difference between the data and the fit.

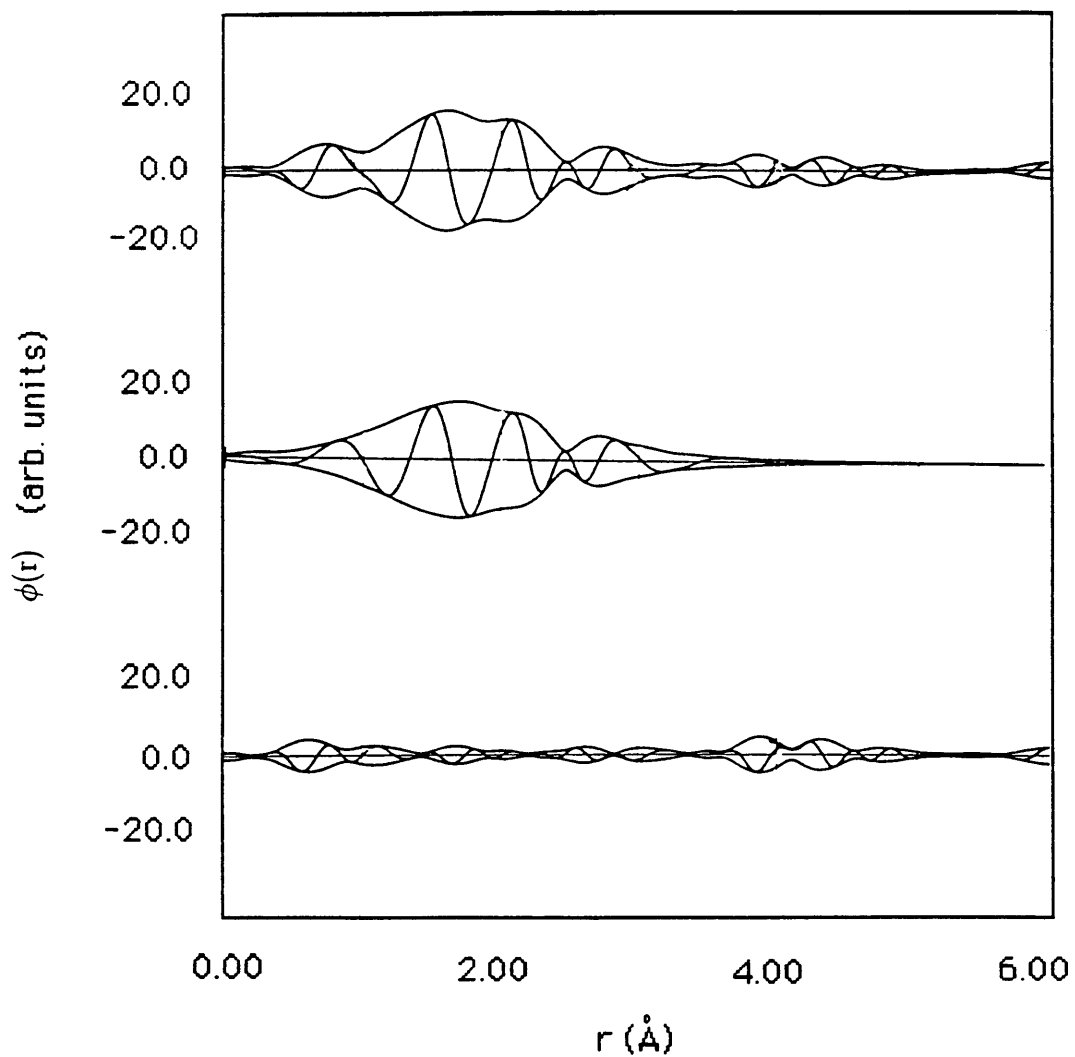


FIG. 4.14: The Fourier transform of the $k\chi(k)$ for p polarization, the fitted data and the difference between the data and the fit.

eral neighbors at different distances. Therefore, we used several signatures together to fit our data. The spectrum from the Cu monolayer was fitted as a linear superposition of ϕ_{Cu-x} where x is Cu, O, Pt. The number and positions of the neighbors in the superposition were treated as variables in the fitting process constrained only by physical common sense. The corresponding fitting curves are the middle portions in Fig. 4.13 (s-pol.) and 4.14 (p-pol.). We achieved a better fit for the p polarization data because of the smaller noise due to Compton scattering from the surface and the water into the detector. The residual of the fitting curves for both s- and p-polarization are similar.

Table 4.4 shows the results of the Cu/Pt system from the model of $2s+p$. As I mentioned in section 3.2.2, this model [59] gives us the total number of neighbors that is independent of the polarization. The results showed that O, Cu, and Pt neighbors are all at reasonable distances comparing to the standards. The schematic diagram of Cu adlayer associated with O is predicted in Fig. 4.15. The Cu-O distance at about $2.06 \pm 0.03 \text{ \AA}$ is probably associated with the model of a single O (from water) sitting on top of the Cu atom (see Fig. 4.15a). The result is consistent with the study of Cu/Au system by the Cornell and IBM groups [44]. Water molecules are not randomly absorbed on the surface, but at a well-defined distances. The oxygen scattering found in our experiment may be also associated with copper oxide film (see Fig. 4.15b). The three nearest Pt neighbors of the Cu atom are at a distance of $2.65 \pm 0.03 \text{ \AA}$ which suggests the Cu sits in a three-fold hollow site of Pt substrate and this short distance results in a strong bonding between the copper adlayer and the Pt substrate. The result is in agreement with XPS study by Kramer *et al.* [28]. Four Cu nearest neighbors are at a distance of $2.62 \pm 0.03 \text{ \AA}$ (great than 2.55 \AA for Cu-Cu standard) which suggests that the Cu layer is in an open structure. The open

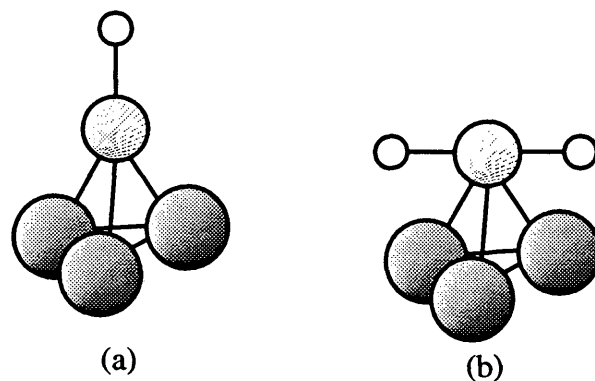


FIG. 4.15: Schematic diagram of Cu adlayer associated with O.
(a): Schematic diagram of Cu and O (from water) on top of Pt surface. (b): Schematic diagram of Cu and O (from oxidize) on top of Pt surface.

Table 4.4: Results from the Model of 2s + p

Type	Number \pm 50 %	Distance \pm 0.03 Å	Angle \pm 10 deg.
O	2.6	2.06	47°
Cu	4.1	2.62	55°
Pt	2.8	2.65	52°

structure may be influenced by the coabsorption of water molecules. Up to now, we have not been able to identify any sulfate ion scattering. If the oxygen we found from our experiment is due to the sulfate ions (SO_4^{2-}) or bisulfate ions (SO_4^-) as has been [44] proposed, we should be able to see the sulfate scattering. Therefore, the oxygen found in the study is either from a water or from a copper oxide-like structure.

More detailed analyses and the final model is still being considered. That work is continuing at RPI and will be published separately as part of the CSM-RPI collaboration.

Chapter 5

SUMMARY AND CONCLUSION

We have used surface extended x-ray absorption fine structure (SEXAFS) spectroscopy to investigate the atomic structure of an adlayer on a dissimilar metal electrode *in-situ*. Although the principle of SEXAFS has been known for quite some time, only recently it has been applied to electrochemical systems. This is because of the availability of synchrotron radiation, which provides high intensity x-rays. X-rays do not interact as strongly with matter as do electrons or ions, therefore it is possible to design an experiment to study a metal buried under a thin layer of water, in an electrochemical environment. Therefore x-rays are unique tools to study electrochemical interfacial structure *in-situ*.

The surface sensitivity of SEXAFS can be improved by using a glancing angle incident geometry (where the incident angle is below the critical angle). If the incident beam is less than the total external reflection angle (5° to several mrad depending on the substrate material), the x-ray only penetrates 20 Å or so into the surface. Electrochemical deposition of Cu on a Pt surface was chosen for several reasons. One is that the deposition of Cu on a Pt surface occurs in a potential range more positive than the reversible Nernst potential for bulk Cu deposition. This phenomenon is termed underpotential deposition (UPD). In many cases the adlayer is a single monolayer [27]. The other reason is that it is relatively easy to prepare a large uniform Pt film (with surface area of 47 cm²) on a UPD by evaporation hence improving the SEXAFS signal to noise ratio. A single scan shows that the signal to noise ratio is 4 considerably better than has been achieved in the past. However, we still accumulated 10 to

20 good scans to further improve the signal to noise ratio. With good quality data, we can determine the phase shift, the scattering amplitude (and hence the coordination number), the nearest neighbor distance and the kind of neighbors.

The big Pt substrate uniquely allowed us to perform the measurement on both s- and p-polarization. This is because in p-polarization geometry that the surface area reduced to 2 mm x 10" which is 13 times smaller than that in s-polarization geometry. However, we still obtained good SEXAFS signal to noise quality with p-polarization. It is important to measure the SEXAFS from both polarizations for the surface SEXAFS study. This is because only those bonds whose interatomic vector has a projection on the plane of polarization of the x-rays will contribute to the SEXAFS. Using both polarizations we can determine the total neighbor number. Cyclic voltammetry of UPD Cu on Pt showed that the total charge on Pt is 505 $\mu\text{coul}/\text{cm}^2$ when the deposition potential is held at 0.05 V vs. copper wire reference electrode. The total charge corresponds to 1.05 monolayer (with respect to a total charge of 480 $\mu\text{coul}/\text{cm}^2$ of Cu on Pt (111) surface). Our QCM mass measurement of the same system showed that only a monolayer of Cu was deposited on the Pt surface. Both measurements showed that Cu adlayer was stable for a long period of time. Our identical S1 and S2 (defined in the section of 4.27) data also give us a strong indication of the Cu adlayer stability.

Near edge spectra of a Cu monolayer on Pt showed that the edge position is about 1 eV below the edge position of metallic copper. The edge position of Cu^+ is 1 eV above the edge position of metallic copper. Therefore, the monolayer of Cu on Pt is more likely neutral than partially discharged.

Our SEXAFS data showed that the oxygen is the nearest neighbor with a distance of $2.06 \pm 0.03 \text{ \AA}$. It is reasonable to see that the monolayer of Cu bonds to oxygen

is either from water or from a copper oxygen complex. This is because anions are coadsorbed with Cu adlayer in the underpotential region. No sulfate scattering was found in our study. Therefore, oxygen found as a nearest neighbor is not from sulfate anions which is contradicted to other *in-situ* EXAFS studies.

The results showed that O, Cu, and Pt neighbors are all at reasonable distances (compare tables 4.4 and 3.2) and the total number of the nearest neighbors of Cu atoms is four. Four Cu nearest neighbors are at a distance of $2.62 \pm 0.03 \text{ \AA}$ which suggests that the Cu layer is in an open structure. The three nearest Pt neighbors of the Cu atom are at a distance of $2.65 \pm 0.03 \text{ \AA}$, which suggests the Cu sits in a three-fold hollow site. The more detailed results and the final model is still under the consideration by our collaborators at PRI.

Chapter 6

SUGGESTED WORK

Traditionally, electrochemists use the measurement and/or control of potential, current, and charge as functions of time to determine the kinetic and thermodynamic parameters of interfacial electrochemical processes. Very little effort, however, has been directed at finding the atomic and molecular specificity and structure at the same time. Due to the development of synchrotron sources that provide high intensity tunable x-rays, SEXAFS has now been applied to *in-situ* electrochemical systems. SEXAFS is a unique tool for probing the interfacial structure at an atomic level.

The Cu monolayer deposition on a Pt substrate in hydrochloric acid solution was also studied here and the voltammogram is presented in Fig. 6.1. The solid curve is the voltammetry of the double layer in Cu^{2+} ion free solution. Dashed lines are stripping curves of Cu monolayer deposition with different waiting time at a potential of 0.1 V vs. copper wire reference electrode. One of those dashed lines (smallest dashed line) is the voltammetry of copper desorption after the deposition potential was held at 0.1 V for 15 minutes. Then the copper layer was stripped after the cell was flushed with copper ion free solution. One can see that there is no big difference between the two voltammogram recorded 15 minutes apart. This suggests that the monolayer of copper is saturated in a very short time and is not continuous growing with time.

The reason for studying the same system with a different electrolyte is that one still does not quite understand where O come stripping curves with different waiting times at 0.1 V indicate that the Cu monolayer is stable. The SEXAFS could be

conducted at this condition. Comparing to Fig. 4.4, the Cu monolayer deposition potential is shifted to the more positive potential, which suggested that the UPD shift is greater in hydrochloric acid solution. This is consistent with recent evidence that the coadsorption of anions causes the potential for the UPD to shift toward more negative values.

It would be very interesting to study the Cu/Pt system with different copper coverage. Our QCM study showed that more charge is transferred when the copper coverage is less than 0.5 monolayer and less charge was transferred when the copper coverage is greater than 0.5 monolayer. This result is consistent with Goodman's [73] study and indicates that co-adsorbed ions play a role in the structure of the interface.

Other system such Cu/Au could be studied as well.

It is necessary to use polycrystalline substrate in order to get a high signal to noise ratio. However, a well defined surface can only be provided by a single crystal. Thus, more information can be obtained by using a single crystal substrate in *in-situ* SEXAFS.

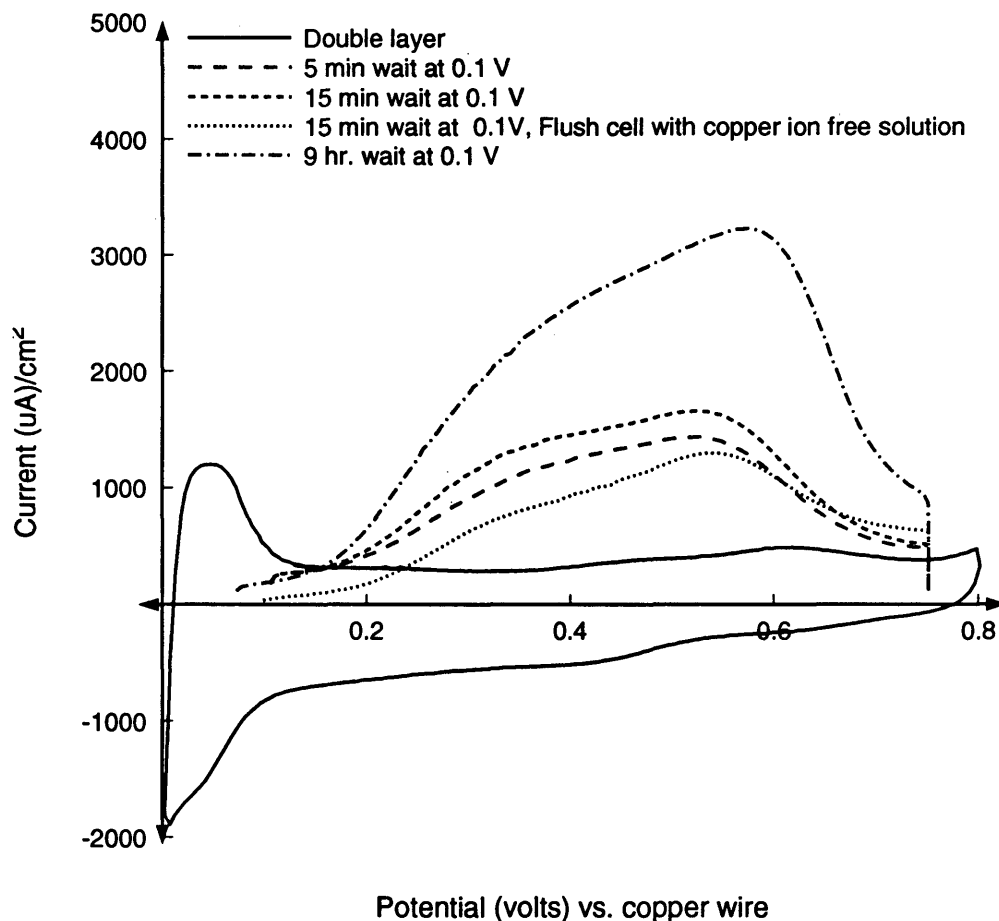


FIG. 6.1: Voltammetry of Cu adlayer on polycrystalline Pt electrode in hydrochloric acid solution. Solid curve is the voltammetry of the double layer in Cu^{2+} ion free solution. Dashed lines are stripping curves of Cu monolayer deposition with different waiting time at potential of 0.1 V vs. copper wire reference electrode. Scan rate: 20 mV/s.

REFERENCES

- [1] M. F. Toney, *Electrochemical Interfaces*. Ed. by H. D. Abruna, VCH publishers, Inc. 1991.
- [2] A. J. Bard and L. R. Faulkner, *Electrochemical Methods*. John Wiley and Sons. New York, 1990.
- [3] P. N. Ross, F. T. Wagner, *Advances in Electrochemistry and Electrochemical Engineering*. H. Gerisher and C. Tobias, Eds. Wiley, New York, **13**,70-109 (1984).
- [4] E. B. Yeager, *J. Electroanal. Chem.* **128** 1600 (1981).
- [5] A. T. Hubbard, *Acc. Chem. Res.* **13** 177 (1980).
- [6] P. N. Ross, *Surf. Sci.* **102** 463 (1981).
- [7] R. Hoffman, in: *Passivity in Metals and Semiconductors*. Ed. M. Froment (Elsevier, Amsterdam 1983) p.147.
- [8] C. H. Lee, R. K. Chang and N. Bloembergen, *Phys. Rev. Lett.* **18** 167 (1967).
- [9] C. K. Chen, T. F. Heinz, D. Ricard, Y. R. Shen, *Phys. Rev. Lett.* **46** 1010 (1981).
- [10] T. E. Furtak, J. Miragliotta and G. M. Korenowski, *Phys. Rev. B.* **35** 2569 (1987).
- [11] R. M. Corn, M. Romagnoli, M. D. Levenson, and M. R. Philipott, *J. Chem. Phys.* **81** 4127 (1984).

- [12] R. M. Corn, M. Romagnoli, M. D. Levenson, and M. R. Philipott, *et al. Chem. Phys. Lett.* **106** 30 (1984).
- [13] P. Gao and M. J. Weaver, *J. Phys. Chem.* **90** 296 (1986).
- [14] X. Gao, A. Hamelin and M. J. Weaver, *Phys. Rev. B.* **44** 10983 (1991).
- [15] M. F. Toney, and S. Brennan, *Phys. Rev. B.* **39** 7963 (1989).
- [16] M. G. Samant, M. F. Toney, G. L. Borges, L. Blum, and O. R. Melroy, *J. Phys. Chem.* **92** 220 (1988).
- [17] M. J. Bedzyk, G. M. Bommarito, M. Caffrey, and T. L. Penner, *Science.* **248** 52 (1990).
- [18] J. Zegenhagen, G. Materlik, *Synchrotron Radiation News.* **6** 19 (1993).
- [19] D. Kolb *Advances in Electrochemistry and Electrochemical Engineering.* Ed. by H. Gerisher and C. Tobias, Wiley, New York, **11** 125-271 (1984).
- [20] S. Wang, W. L. Mochań, and R. G. Barrera, *Phys. Rev. B.* **42** 9155 (1990).
- [21] O. Melroy, K. Kanazawa, J. G. Gordon II and D. Buttry, *Langmuir.* **2** 697 (1986).
- [22] D. A. Buttry and M. D. Ward, *Chemical Reviews.* **92** 1355 (1992).
- [23] G. Z. Sauerbrey, *Z. Phys.* **155** 206 (1959).
- [24] H. Winick, S. Doniach, Eds. *Synchrotron Radiation Research.* Plenum, New York, (1980).
- [25] B. J. Bowles, *Electrochimica Acta.* **15** 589 (1970).

- [26] D. M. Kolb, R. Kötz and K. Yamamoto, *Surface Sci.* **87** 20 (1979).
- [27] D. M. Kolb and R. Kötz, *Surface Sci.* **64** 698 (1977).
- [28] T. Kramar, R. Podloucky, A. Neckel, H. Erschbaumer and A. J. Freeman, *Surface Science.* **247** 58 (1991).
- [29] E. Schmidt and H. R. Gygax, *J. Electroanal. Chem.* **12** 300 (1966).
- [30] E. Schmidt, H. R. Gygax and P. Böhlen, *Helv. Chmi. Acta.* **49** 733 (1966).
- [31] J. O. Bockris and A. K. N. Reddy, *Modern Electrochemistry.* Plenum, New York, (1970).
- [32] J. H. White and H. D. Abruna, *J. Phys. Chem.* **94** 894 (1990).
- [33] K. Kunimatsu, M. G. Samant and H. Seki, *J. Electrochem. Soc.* **258** 163 (1989).
- [34] G. Horanyi and G. Vertes, *Electroanalytical Chemistry and Interfacial Electrochemistry.* **45** 295 (1973).
- [35] G. Horanyi, *Electroanalytical Chemistry and Interfacial Electrochemistry.* **55** 45 (1974).
- [36] K. Sashikata, N. Furuya and K. Itaya, *J. Electrochem. Soc.* **316** 361(1991).
- [37] O. M. Magnussen, J. Hotlos, R. J. Nichols, D. M. Kolb and R. J. Behm, *Phys. Rew. Lett.* **64** 2929 (1990).
- [38] O. M. Magnussen, J. Hotlos, G. Beitel, D. M. Kolb and R. J. Behm, *J. Vac. Sci. Technol. A* **B9** 969 (1991).
- [39] O. R. Melroy, M. G. Samant, G. L. Borges, J. G. Gorden, L. Blum, J. H. White, M. L. McMillan and H. D. Abruna, *Langmuir.* **4** 728 (1988).

- [40] T. Hachiya, H. Honbo, and K. Itaya, *J. Electrochem. Soc.* **315** 275 (1991).
- [41] J. H. White and H. D. Abruna, *J. Electroanal. Chem.* **274** 185 (1989).
- [42] J. McBreen, W. E. O'Grady, G. Tourillon, E. Dartyge and A. Fontaine, *J. Electroanal. Chem.* **307** 229 (1991).
- [43] R. Durand, R. Faure, D. Aberdam, C. Salem, G. Tourillon, D. Guay and M. Ladouceur, *Electrochimica Acta.* **37** 1977 (1992).
- [44] L. Blum, H. D. Abruna, J. H. White, J. G. Gordon, G. L. Borges, M. G. Samant and O. R. Melroy, *J. Chem. Phys.* **85** 6732 (1986).
- [45] G. Tourillon, D. Guay and A. Tadjeddine, *J. Electroanal. Chem.* **289** 263 (1990).
- [46] A. Tadjeddine, D. Guay, M. Ladouceur and G. Tourillon, *Phys. Rev. Lett.* **66** 2235 (1991).
- [47] M. G. Samant, G. L. Borges, J. G. Gordon and O. R. Melroy, *J. Electrochem. Soc.* **109** 5920 (1987).
- [48] S. Manne, P. K. Hansma, J. Massie, V. B. Elings, A. A. Gewirth, *Science.* **251** 183 (1991).
- [49] H. Bort, K. Jüttner, W. J. Lorenz, G. Stailov and E. Budevski, *Electrochimica Acta.* **28** 985 (1983).
- [50] A. Milchev, S. Stoyanov and R. Kaishev, *Thin Solid Films.* **22** 267 (1974).
- [51] B. Pettinger, M. R. Philpott and J. G. Gordon, *J. Chem. Phys.* **74** 934 (1981).
- [52] J. W. Gadzuk, *Surface Science.* **43** 44 (1974).

- [53] R. L. Kroning, *Z Phys.* **70** 317 (1931).
- [54] R. L. Kroning, *Z Phys.* **75** 191 (1932).
- [55] T. M. Hayes and J. B. Boyce, *Solid State Physics.* **37** 173 (1976).
- [56] M. F. Toney and S. Brennan, *Phys. Rev. B.* **39** 7963 (1989).
- [57] P. A. Lee and J. B. Pendry, *Phys. Rev.* **B11** 2795 (1975).
- [58] P. A. Lee, P. H. Citrin, P. Eisenberger and B. M. Kincaid, *Reviews of Modern Physics.* **53** 769 (1981).
- [59] Private communication with Prof. T. Hayes.
- [60] X-ray Data Booklet. Lawrence Berkeley Laboratory, 1986
- [61] Private communication with Dr. F. Lytle.
- [62] M. W. Breiter, *Electrochim. Acta.* **8** 925 (1963).
- [63] M. Nakamura and H. Kita, *J. Electroanal. Chem.,* **72** 165 (1976).
- [64] P. N. Ross, *Surface Science.* **102** 463 (1981).
- [65] J. Clavilier, *J. Electroanal. Chem.* **107** 211 (1980).
- [66] A. T. Kuhn, *Techniques in Electrochemistry.* John Wiley and Sons, (1987).
- [67] K. Itaya, S. Sugawara and K. Higakim, *J. Phys. Chem.* **92** 6714 (1988).
- [68] E. Yeager, W. E. O' Grady, M. Y. C. Woo and P. Hagans, *J. Electrochem. Soc.* **125** 356 (1978).

- [69] J. Clavilier, R. Faure, G. Guinet and R. Durand, *J. Electroanal. Chem.* **107** 205 (1980).
- [70] A. T. Hubbard, R. Ishikawa and J. Kutukara, *J. Electroanal. Chem.* **86** 271 (1978).
- [71] F. T. Wagner and P. N. Ross, *J. Electroanal. Chem.* **150** 141 (1983).
- [72] T. E. Furtak, and Li Wang (in preparation).
- [73] L. H. Leung, T. W. Gregg and D. W. Goodman, *Chemical Physics Letters.* **188** 467 (1992).
- [74] Private communication with Dr. L. Lurio at Rensselaer Polytechnic Institute.
- [75] J. S. Hammond and N. Winograd, *J. Electroanal. Chem.* **80** 123 (1977).
- [76] P. C. Hiemenz, *Principles of Colloid and Surface Chemistry*. 2nd ed. Eds. Marcel Dekker, inc. New York and Basel, (1986).
- [77] D. Stern, *Elektrochem.* **30** 508 (1927).
- [78] D. C. Grahame, *Chem. Rev.* **41** 44 (1947).
- [79] J. O. Brockris and A. G. Martin, *Spectroscopic and Diffraction Techniques* Kluwer & Dordrecht, (1990).
- [80] K. Kunimatsu, W. G. Golden, H. Seki and M. R. Philpott, *Langmuir* **1** 245 (1985).
- [81] J. N. Glosli and M. R. Philpott, *J. Chem. Phys.* **96** 6962 (1992).

Appendix A

CLEANING PROCEDURE FOR GLASS SUBSTRATES

1. Rinse the glass substrate with distilled water. Do not use anything to scratch it;
2. Use Ethyl alcohol to drag wipe (means drop alcohol on the substrate and used lens tissue pulled along the substrate) it 5-6 times;
3. Drag wipe with 18 M Ω distilled water 5-6 times;
4. Drag wipe with solution (one drop of Targital chemical and 500 monolayer water) 5-6 times;
5. Rinse with 18 M Ω distilled water very thoroughly;
6. Drag wipe with 18 M Ω distilled water 5-6 times;
7. Then blow substrate with pure nitrogen gas with filter to dry the substrate.

Appendix B

MODELS FOR THE SOLID-ELECTROLYTE INTERFACE(DOUBLE LAYER STRUCTURE)

B.1 The Parallel-Plate Condenser (Helmholtz Model)

This model of the solid-electrolyte interface was proposed first by Helmholtz more than a century ago. He oversimplified the interface as a parallel compressed capacitor. This is the situation that when the metal is charged with an excess charge density q_m , an equal and opposite excess charge density q_s on the solution side at the outer Helmholtz plane (OHP) (due to the solvated ions) is built. These two layers of excess charge give rise to the term of double layer. The simple model leads a linear variation of potential Ψ_H across the two layers:

$$\Psi_H = \frac{4\pi x dq_m}{\epsilon} \quad (\text{B.1})$$

and its differential,

$$dH = \frac{4\pi x dq_m}{\epsilon} \quad (\text{B.2})$$

and the capacity,

$$C_H = \frac{dq_m}{dH} = \frac{4\pi x}{\epsilon} \quad (\text{B.3})$$

is a constant. Where x is the distance between the two parallel charged plates (several angstroms, and ϵ , the product of $\epsilon_1 \epsilon_0$, is the dielectric constant of the material between the plates. The potential drop between the two charged plates is about 1 volt, and the electrical field is about 1×10^7 V/cm. The consequence of Helmholtz model is that the

high electrical field tends to orient molecular dipoles which is reasonable. However, the experimental observation of the potential is not a linear relation vs the distance. The minimal capacitance at the potential of zero charge (pzc), the concentration dependence, which observed in the experiment, can not be obtained from this model as well. The concentration dependence of the capacitance is missing too. Therefore, this simplified model does not show the real behavior of the solid-solution interface and needs to be modified.

B.2 The Diffuse Double Layer (Gouy-Chapman Model)

The diffuse double layer model was introduced by G. Gouy (in 1910) and D. L. Chapman (in 1913) independently. This model is the consideration of the thermal kinetic motion of charges in the solution. It postulates that charges in the solution are like point charges in an isotropic dielectric medium. The charge distribution in the vicinity of the electrode is determined by the combined effect of coulombic interaction (migration) and concentration gradient (diffusion) between the electrode and the ions. These two opposite motions destroy the compact charge layer and ions distribute in a certain region near the electrode. The variation of potential with distance from a charged surface of arbitrary shape within the double layer is described by the Poisson-Boltzmann equation [76]:

$$\frac{d^2\Psi_H}{dx^2} = \frac{-e}{\epsilon} \sum_i Z_i n_{i0} \exp\left[-\frac{Z_i e \Psi_H}{kT}\right] \quad (\text{B.4})$$

Where e is the electron charge, Z_i is valence number which could be either positive or negative integer, n_{i0} is the number of ions of type i far from the electrode surface, or the bulk concentration of the species i , k represents Boltzmann constant as usual. Since Eq. (B.4) include ϵ , it provides for the effect of the medium. The solution of

Eq. (B.4) is:

$$\Psi_G = \frac{4kTA_0}{Ze} \exp(-\gamma x) \quad (\text{B.5})$$

with

$$A_0 = \frac{\left[\exp \frac{Ze\Psi_0}{2kT} - 1 \right]}{\left[\exp \frac{Ze\Psi_0}{2kT} + 1 \right]} \quad (\text{B.6})$$

and

$$\gamma^2 = \frac{e^2 \sum_i Z_i^2 n_{i0}}{\epsilon kT} \quad (\text{B.7})$$

when Ψ_0 (potential at the electrode surface) is large, $A_0 \rightarrow 1$, Eq. (B.5) is independent of the potential at the electrode surface.

$$C_G = \left[\frac{\epsilon Z^2 e^2 n_0}{2\pi kT} \right]^{1/2} \cosh \frac{Ze\Psi_H}{kT} \quad (\text{B.8})$$

The G-C model predicts that the capacitance shows a minimum at the pzc and increases at higher ion concentration. It is important to note that the Gouy-Chapman relationship works well, but only for dilute solutions and low values of surface charge density (or near the pzc). Also, Ψ_G decreases more rapidly than predicted with higher ionic concentration and higher valence number γ .

B.3 The Inner Layer Double Layer (Stern-Grahame Model)

As we mentioned before, the Gouy-Chapman model has difficulty to explain the experimental results in concentrated solutions. It was Stern who modified the double layer model [77]. He postulated that ions could not approach the electrode beyond a certain distance because of their *finite sizes*. Thus the inner boundary of the diffuse layer is the plane containing the centers of closest approach of ions. In 1947, Grahame concluded [78] that there should be two planes of closest approach in the double layer

when he interpreted the experimental data. These two planes consist of the inner helmholtz plane (IHP) (the center of specific adsorbed ions) and the outer helmholtz plane (OHP) (the center of non-specific adsorbed ions). Therefore, the total capacity, C , in the double layer should be represented as a series combination of an inner layer capacity C_H (or the capacity from Helmholtz model) and a diffuse layer capacity C_G (or the capacity from Gouy-chapman model):

$$\frac{1}{C} = \frac{1}{C_H} + \frac{1}{C_G}. \quad (\text{B.9})$$

From Eq.(B.9), One can see that C_G becomes large while C_H does not change for a concentrated electrolyte. Thus, the total capacity C in the double layer region is equal to the capacity of the Helmholtz model(C_H). This suggests that most charges in the higher concentrated solution are confined in (or near) the Helmholtz plane and little charge is diffused into the diffuse double layer. However, this model is good only for a limited electrode (*e.g.* Hg/NaF interface).

B.4 Water Structure in the Double Layer BDM Model

In 1963, Bockris [31], Devanathan, and Müller (BDM) postulated that a metal electrode is largely (about 70%) covered with adsorbed water molecules. These water molecules will interact with the electrode surface. This short range interaction is not included in any previous model. At the beginning, one might only think the interaction is electrostatic. But, with this prediction, one could not explain why negative charges adsorb on a negatively charged electrode. In order to explain the problem, one should consider other effects like image forces (between water molecule or water dipoles in the solution side and their image dipoles in the electrode side) and dispersion forces (between an instantaneous dipole due to proton and electron

in solution side and metal side). It is this interaction which causes negative charge to be adsorbed on a negatively charged electrode. This kind of adsorption is called specific adsorption or contact adsorption. The region between the electrode surface and IHP (the center of the contact adsorbing ions) is called compact region, and the region between the IHP and OHP is called diffuse ion region.

B.5 Molecular Dynamics Simulation of Ion Adsorption

After the BDM model was proposed, contact adsorption was verified by various techniques. They include: differential capacitance [79], SEXAFS [44, 39], Fourier transform infrared [80]. But the first molecular dynamics simulation of ion adsorption on charged electrodes was reported by Glosli and at. al. [81]. The simulation system includes 214 water molecules, one lithium (Li^+) ion and one iodide (I^-) ion. All molecules were confined to two oppositely charged *flat* plates. The electric field between two charged plates is 2×10^7 V/cm. A small number of molecules were chosen to explore time scales up to a nanosecond. The reason for choosing LiI is that the system represent extreme cases for adsorption. The previous experiments showed that the Li^+ is strongly hydrated and it is not the contact absorption on the charged electrode. In contrast, the I^- is completely contact adsorbed on the charged electrode. The nice thing about the computer simulation is that the method provides the insight of how ions and water orient in the presence of an electric field at a charged surface. The simulation results showed that the molecular distribution is not symmetric. The solvated lithium ion does not lose any waters when it adsorbed on the electrode and the solvated ion defines the OHP, whereas the iodide ion is strongly contact adsorbed on the electrode and the unsolvated ion defines the IHP.

Appendix C

REFLECTANCE SPECTROSCOPY SET-UP

A schematic diagram of the experimental set-up is shown in figure C.1. An unpolarized white light from a projector lamp with a tungsten filament was used as a source. The incident angle of the beam was about 45° . A piece of glass was used to reflect the incident beam as a reference beam. The incident beam with the wavelength between 480 nm to 800 nm can be transmitted through the Kapton window. Both the reference beam and the reflected beam go through the same collection lens. Two identical Si photocells (S1087-01) were used to detect the reference beam and the reflected beam. The signal from those photocells was amplified by a pre-amplifier. A signal processor recorded the differential reflectance $(R_1 - R_o)/R_o$. The detailed information about the monolayer preparation can be found in section 4.1.5. An X-Y recorder records $(R_1 - R_o)/R_o$ vs the potential or time.

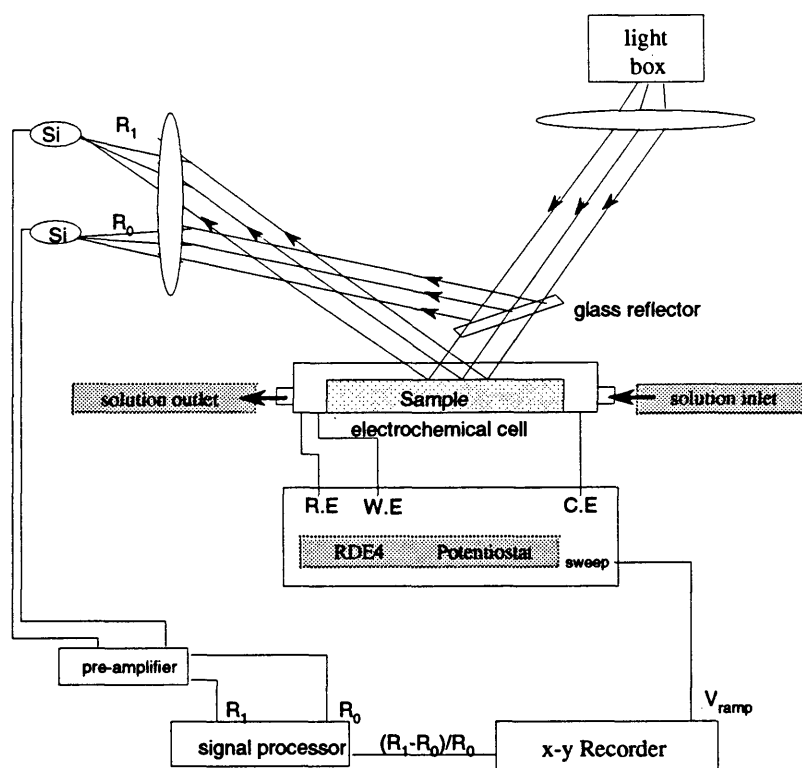


FIG. C.1: schematic diagram of the reflectance experimental set up.